MSc thesis in Offshore and Dredging Engineering

Rock behavior in and below an inclined fall pipe

Jasper Fontijn

2023

TU Delft

Boskalis

Rock behavior in and below an inclined fall-pipe

by

Jasper Fontijn

to obtain the degree of Master of Science
at the Delft University of Technology.

Student number:	4458907	
Project duration:	May 2, 2022 – June 13, 2023	
Thesis committee:	Prof. dr. ir. Cees van Rhee,	TU Delft
	Dr. ir. Arno Talmon,	TU Delft
Company supervisors:	Ir. Roeland Neelissen,	Boskalis
	Ir. Guido van der Salm,	Boskalis
	Ir. Remmelt van der Wal,	Boskalis

TU Delft Delft University of Technology

Boskalis

Abstract

Subsea rock installation is an offshore engineering process where rocks are placed on the seabed as protection of cables and pipelines and as scour protection. The inclined fall-pipe is a new piece of equipment specifically designed to install rocks close to submerged structures. This thesis investigates the processes of the rock flow in and below the inclined pipe. This is done with a research question in two parts: What is the rock behavior in the inclined fall-pipe, and what is the behavior below the inclined fall-pipe? The research is questions are supported by sub-questions on the influence of pipe angle, production and rock size.

To answer the research questions model tests have been carried out at a scale of 1:15 in the Dredging Lab at TU Delft. The tests were performed with varying pipe angles, production rates and rock sizes. The tests have been analyzed with special focus on velocity, flow behavior, touch down offset from the pipe, and the spread of the rocks. For analysis, video recordings of the tests have been used and the tests have been analyzed with Particle Image Velocimetry software PIVlab.

The results of the tests reveal that the velocity of the rock flow mostly depends on the pipe angle and production rate, and for a lesser part on the rock size. Steep pipe angles increase rock velocity, increasing production leads to a higher average velocity, and smaller rock sizes increase the velocity.

The spread of the rocks and the offset from the pipe are influenced the strongest by the stand-off (SOD) distance between the pipe and the bed. In the tests the SOD was determined by the pipe angle. To compare the tests, they were also analyzed at the same height below the pipe. The results show that the spread of the rocks is only influenced by the height above the floor. The offset is influenced both by the angle and the production. The influence of the production is only visible at lower angles. The increase in production means an increase in velocity and the rocks falling further away. More horizontal pipe angles give the rocks more horizontal velocity, making the rocks fall further away.

Contents

List of symbols

Symbol	*Description*	*Unit*
A	Cross-sectional area	m^2
C	Concentration	$-$
C_D	Drag coefficient	$-$
C_L	Lift coefficient	$-$
C_{vb}	Concentration of the bed	$-$
C_{vd}	Delivered volumetric solids concentration	$-$
C_{vi}	Spatial volumetric solids concentration in pipe	$-$
d	Particle diameter	m
D	Pipe diameter	m
D_h	Hydraulic diameter	m
f	Frequency of separation	s^{-1}
F_D	Drag force on a particle	N
F_G	Gravitational force on a particle	N
F_N	Normal force	N
F_V	Force on a rock due to horizontal flow	N
F_W	Submerged weight	N
Fr	Froude number	$-$
g	Gravitational acceleration	m/s^2
h	Height of the bed	m
L	Pipe length	m
n	Hindered settling coefficient	$-$
N	Number of horizontal fluctuations	$-$
O	Perimeter length	m
P	Sphere-fluid parameter	$-$
P	Pressure	Pa
Q	Volumetric low rate	m^3/s
Re_p	Particle Reynolds number	$-$
Re_t	Terminal Reynolds number	$-$
S_{hor}	Horizontal fluctuation	m
St	Strouhall number	$-$
S_{ver}	Vertical distance during a fluctuation	m
t	Time	s
T	Vortex separation period	s
v	Velocity	m/s
v_f	Fluid velocity	m/s
v_m	Mixture velocity	m/s
v_s	Solids velocity	m/s
V	Flow velocity	m/s
V	Volume	m^3
$\bar{V}$	Depth averaged flow velocity	m/s

$V_{rock,hor}$	Horizontal rock velocity	m/s
$V_{rock,ver}$	Vertical rock velocity	m/s
w_0	Particle settling velocity	m/s
$w_{0,p}$	Particle settling velocity in a pipe	m/s
w_s	Hindered settling velocity	m/s
$w_{s,p}$	Hindered settling velocity in a pipe	m/s
w_θ	Particle settling velocity on an incline	m/s
W_b	Weight of the bed	kg
$W_{b,s}$	Submerged weight of the bed	kg
x	Distance	m
Y	Dimensionless velocity	$-$
y'	Correction factor	$-$
α	Angle defining a position if the pipe cross-section	$^\circ$
β	Rock falling angle	$^\circ$
β	Angle defining interface position	$^\circ$
Δ	Specific density of the solids	$-$
θ	Inclination angle	$^\circ$
λ	Darcy-Weisbach friction coefficient	$-$
λ_w	Relative particle size	$-$
μ_{CD}	Mean drag coefficient	$-$
μ_f	Dynamic viscosity	$Pa \cdot s$
ν	Kinematic viscosity	m^2/s
ρ_f	Density of the liquid	kg/m^3
ρ_m	Density of the mixture	kg/m^3
ρ_s	Density of the solid particle	kg/m^3
σ_{CD}	Standard deviation of the drag coefficient	$-$
σ_G	Standard deviation random walk model	$-$
σ_i	Standard deviation individual fluctuation	m
σ_N	Standard deviation number of fluctuations	$-$
σ_s	Interganular normal stress	Pa
τ_s	Intergranular shear stress	Pa
τ_{12}	Interfacial shear stress	Pa
τ_2	Bed shear stress	Pa
ϕ	Grain angle of repose	$^\circ$

Chapter 1

Introduction

In this chapter, the subject of subsea rock installation through an inclined fall-pipe will be introduced. The goal of the thesis will be described with a problem definition, the objective and the research questions. Finally the approach and outline of the thesis will be given.

Rock installation has been an essential part of coastal protection works and offshore platform installation for decades and more recently also for wind turbine installation. It started with placing rocks by hand in ancient times, to dumping from barges, to the invention of the side-stone dumper, to the vertical fall-pipe and currently the inclined fall-pipe. The inclined fall-pipe is specifically designed to ease the placement of rocks close to submerged structures. Traditional fall-pipe vessels with the pipe lowered through a moon pool cannot maneuver close enough to the quay side, jacket or monopile foundation to install the rocks directly next to them. With the pipe over the side of the vessel, angled toward the structure, this is made a lot easier, also illustrated in figure 1.1.

Figure 1.1: Three different methods of fall-pipe use: a flexible bucket system, a vertical fall-pipe and an inclined fall-pipe.

1.1 Problem description

The inclined fall-pipe is a new piece of equipment in the world of subsea rock installation. No public research is yet available on the rock behavior in the inclined fall-pipe and the influence of the inclined fall-pipe on the behavior on the rocks when they exit the pipe. The aim of subsea rock installation works is to place the rocks as efficient as possible around the structure. To do that, knowledge of the mechanics and processes in and below the inclined fall pipe are necessary.

These processes and mechanics are known to a limited extent. Vertical subsea rock installation, transport through inclined pipe and the unrestricted falling of rocks are well researched topics. What is not yet known is how these topics come together in rock installation through an inclined fall pipe. Therefore the problem is defined as:

"There is a limited extent of knowledge on the behavior of rock flow in and below an inclined fall-pipe."

1.2 Thesis objective

The main objective of this thesis is to gather knowledge on the processes in and below the inclined fall-pipe. Only the behavior in the pipe and directly below the pipe will be investigated in this thesis. The interaction of the rocks with the current, the influence of ship hydrodynamics and interaction with the seabed are also very interesting topic necessary of research but are no subject of the scope of this project.

The influence of operational parameters will be used as a subject of this research, such as production levels, rock gradings and pipe angles, but with a broader range compared to what is used in practice to gain as much understanding of the processes as possible. An example of the expanded parameters is pipe angles outside of the designed operating range.

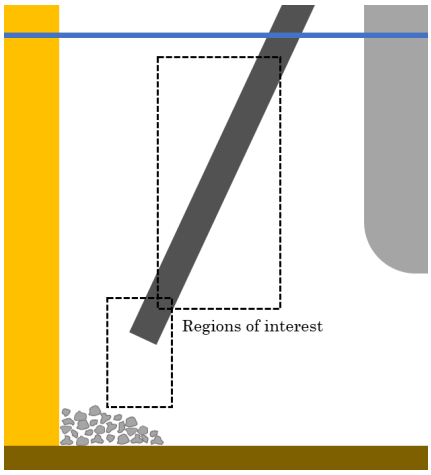

Figure 1.2: Regions of interest of this thesis.

The objective is supported by two main research questions with sub questions:

What is the behavior of rock flow in an inclined fall-pipe?

- *How is the behavior influenced by the production?*
- *How is the behavior influenced by the rock size?*
- *How is the behavior influenced by the pipe inclination angle?*
- *What kind of behavior is shown? I.e., sliding, rolling, jumping or falling?*

What is the behavior of rocks falling out of an inclined fall pipe?

- *How is the behavior influenced by the production?*
- *How is the behavior influenced by rock size?*
- *How is the behavior influenced by the pipe inclination angle?*
- *How is the spread and offset of the rock dump influenced?*

The 'behavior' in the questions refers to the way the rocks move in and below the pipe and the velocity the rock flow reaches. To give answer to these questions, model tests were carried out in the Dredging Lab at Delft University of Technology. The setup consists of a large tank filled with water, a clear plastic pipe and cameras to record the tests. The cameras record the regions of interest marked in figure 1.2. The setup is at a scale of 1:15. The tests were carried out with four different production levels, three different rock sizes and five different pipe angles. The tests were then analyzed for the velocity in and below the pipe, the flow behavior, the offset from the pipe and the spread of the

rocks. The tests were analyzed manually from the video recordings and with particle image velocimetry (PIV) software PIVlab.

1.3 Thesis structure

The thesis is a description of the research carried out to answer the research questions. The content of each chapter is briefly explained:

- *Chapter 2* gives a background on subsea rock installation, placing the thesis in context.
- *Chapter 3* first focuses on the forces a spherical particle experiences when free-falling and during pipeline transport, and secondly it focuses on the velocity particles of falling alone, in groups, in pipes and on inclinations.
- *Chapter 4* investigates processes connected to the falling behavior of rocks and its innate randomness due to the irregular shape of the particles. Two models describing the motion of the rocks are given: the random walk model is used to determine the spread of the rocks and the offset model describes the influence of the horizontal velocity on the horizontal distance (offset) of the rocks below the pipe.
- *Chapter 5* explores the mechanics of two-layer flow in the pipe, using the two-layer model for stratification in pipelines.
- *Chapter 6* is about scale effects that arise from changing from reality to model scale. It goes deeper into the concept of Froude and Reynolds similarity.
- *Chapter 7* explains the methodology and the setup of the tests, and why the parameters were chosen.
- In *chapter 8* the results of the processes in the pipe are analyzed.
- In *chapter 9* the results of the processes below the pipe are analyzed.
- *Chapter 10* presents the conclusions of the research and gives recommendations for future research.

Chapter 2

Subsea rock installation

This chapter is about the subsea rock installation, the different methods of rock installation and the applications of subsea rock installation are discussed.

Rock has been used as protection for thousands of years, at first mostly on land and on the coast, but in recent decades also at sea, at increasing depths, even up to 2000 m. At first, rocks were installed by hand or from barges as coastal protection, break waters and harbor heads. Modern methods have been developed more recently. Side-stone dumping vessels were used to mechanically shove rocks over the side of the vessel. The problem with these vessels is the decreasing accuracy at increasing depths, and because of this the fall-pipe was developed. The fall-pipe provides guidance from the vessel to the sea floor.

2.1 Installation methods

The rock manual (CIRIA et al., 2007) describes three methods for accurately placing rocks, also pictured in figure 2.1:

- Side stone-dumping vessels
- Vessels with excavators or cranes
- Fall-pipe vessels

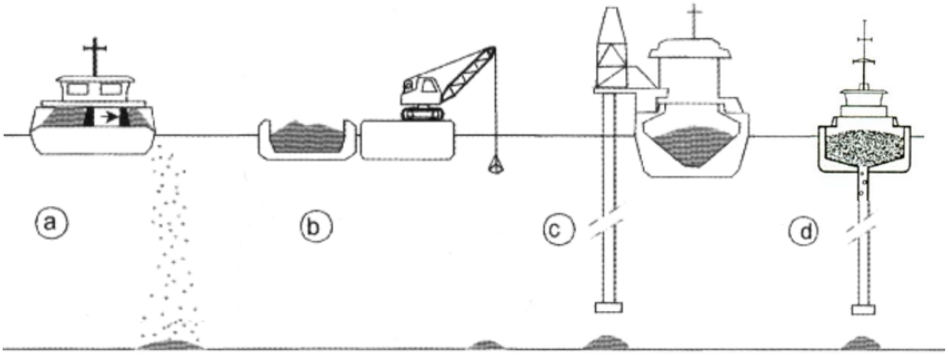

Figure 2.1: Rock installation methods. (Edited from de Reus, 2004)

2.1.1 Side stone-dumping vessels

Side stone-dumping vessels (SSDVs) can dump relatively large amounts of stone in a controlled manner. The stones are either transported off the deck by chains or a vibrating deck or by sliding shovels. The important factor in controlling the dumping process is the speed at which the stones are pushed overboard. SSDVs can place rocks in layers by moving laterally in a controlled speed, or in narrow ridges by moving forward. These vessels are often equipped with thrusters and a dynamic position system for this purpose.

The decks of these vessels are typically divided in sections that can be unloaded separately. This may be used when, for example, a layer of smaller stones has to be protected from strong currents by larger stones. These vessels have a large range of loading capacity ranging from 500 tons to 2000 tons. They are capable of dumping very large stones, even very close to existing structures.

Figure 2.2: Side stone-dumping vessel NDeavor.

2.1.2 Vessels with excavators or cranes

With this equipment, small quantities of stones can be placed each time, or large stones individually. Compared to SSDVs less specialized equipment is necessary, like dynamic positioning, making this option more easily available.

Excavators can be used to place armor stones of different gradings in the same dumping operation, and are typically used to place relatively small stones for breakwaters or slope protection.

Cranes are more often used when the area for maneuvering is small or the total quantity of rock to be placed is small, making other options not economically viable. Cranes are very accurate and can be used to place rocks individually or place large bags. Cranes are also used for depths excavators cannot reach.

Figure 2.3: Backhoe dredger Magnor

2.1.3 Fall-pipe vessels

Fall-pipe vessels are used to achieve great accuracy even in deep waters, and can work accurately up to depths of 2000 meters. The pipe guides the stones to several meters above the seabed where they are released. Fall-pipe vessels are most commonly used for pipeline and cable protection, preparation for foundations, slope protection and scour protection.

Two categories of fall-pipe systems can be distinguished. Semi-closed flexible fall-pipe systems and closed fall-pipe systems. A semi-closed flexible fall-pipe consists of a column of conical, bottomless buckets connected to each other that is lowered to the sea bed. The semi-closed systems sucks in sea water over the whole length of the pipe. This make this type of pipe viable for installing rocks at extreme depths.

Closed systems consist of a continuous closed pipe. Closed systems vary from simple pipes lowered from a spudded pontoon where the pontoon is moved after a set amount of rock is dropped through the pipe, to advanced systems with hydraulic hoist wires, rails and dynamic tracking systems to control the pipe, either through a moon pool or over the side of the vessel.

A relatively new development is the inclined fall-pipe, where the pipe has an inclination to the vertical, in order to keep distance from the structure where rock is installed. This eases the installation around monopile foundations or near walls.

Figure 2.4: Three types of fall-pipe design: a flexible fall-pipe system, a closed fall-pipe and an inclined fall-pipe.

2.2 Applications

There are two main applications of rock installation, protection and foundations. Protection for example against scour, waves and foreign objects like anchors or nets, and foundations for wind turbines, offshore platforms and pipelines.

2.2.1 Scour protection

Scour is the removal of sediment or soil around the base of objects in flow. Velocity changes around the object in the flow cause the suspension of particles and the removal of particles can cause instability in the structures. To protect against the removal of the soil, rocks are placed around the structure that are too heavy to be picked up by currents Additional protection against erosion and waves can be gained by placing larger rocks, a so called armor layer.

2.2.2 Pipeline and cable protection

The sea floor is covered with pipelines cables for the transport or oil and gas and electricity. These cables and pipes cover great distances and are vulnerable to terrain changes, temperature changes, falling objects, dragnets and anchors. To protect the cables and pipes, rock layers can be installed, either below (pre-lay) or on top of the pipes (post lay). The pre-lay can act as supports to cover spans or be used to fill pits. The post lay prevents again temperature induced buckling, falling objects, anchors and nets.

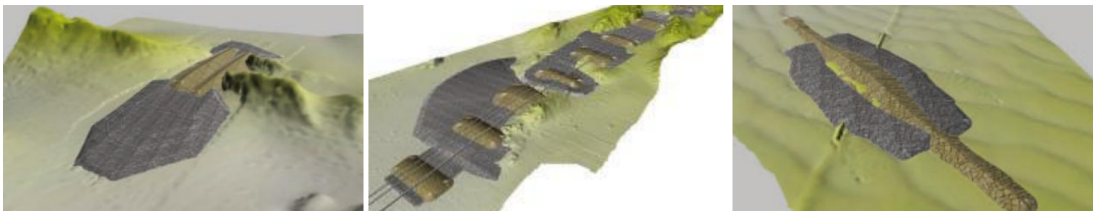

Figure 2.5: Three example of subsea rock installation. On the left the basic design of supports and counter fills, in the middle free span mitigation and on the right a pipeline crossing design (Visser & van der Meer, 2008).

2.2.3 Foundations

Subsea rock installation is also used to create suitable foundations for offshore platforms and wind turbines. Soils can be to soft, or the sea floor is uneven. A rock layer is placed to spread out the loads of the construction to be installed or to create an even layer on the seabed to install the structures on.

2.3 Inclined fall-pipe

Figure 2.6: The inclined fall-pipe installed on the Rockpiper.

Chapter 3

Falling of spherical particles

3.1 Introduction

This chapter first describes the forces acting on single particles, then it defines the velocity a single particle or rock attains during settling. This chapter is based on the lecture notes by Van Rhee (van Rhee, 2018) and by Talmon (Matoušek & Talmon, 2021).

3.2 Transport of single, spherical particles

For many dredging applications, particle mixtures are carried through pipes. The forces acting on the particles come from the interaction between the particles or the interaction between the carrier liquid and the particles. The forces acting on the particles are gravity, drag, buoyancy and lift force. Since most particle transport is characterized by turbulent flow, the particles undergo turbulent diffusive forces.

3.2.1 Gravitational and buoyancy forces

The force acting on the body due to gravitational acceleration is determined from the particle volume and density. For a spherical particles this is described by:

$$F_G = \rho_s g \frac{\pi d^3}{6}. \tag{3.1}$$

With	F_G	gravitational force on a particle	N
	ρ_s	density of the solid particle	kg/m^3
	g	gravitational acceleration	m/s^2
	d	diameter of the particle	m

Archimedes law states that particles submerges in liquid obey a buoyancy effect which decreases its weight in the carrying fluid. For the same spherical particle this is

$$F_w = (\rho_s - \rho_f)\, g \frac{\pi d^3}{6}. \tag{3.2}$$

With	F_W	submerged weight of a spherical particle	N
	ρ_s	density of the solid particle	kg/m^3
	ρ_f	density of the liquid	kg/m^3
	g	gravitational acceleration	m/s^2
	d	diameter of the particle	m

3.2.2 Drag force

Particles moving through liquid experience a resisting force from the liquid on the particle. Either the particle can be moving through a fluid of the fluid moves around the particle, or both at the same time. The resisting force is called the drag force F_D and the magnitude of this force depends on the drag coefficient C_D. The rocks in subsea rock installation fall in the turbulent transition region of Reynolds numbers larger than 1000. The drag force can be calculated with

$$F_D = \frac{1}{2} C_D \rho_f A_s v^2 \tag{3.3}$$

With	F_D	drag force on a particle	N
	C_D	drag coefficient	$-$
	ρ_f	density of the liquid	kg/m^3
	A	cross-sectional area	m^2
	v	velocity	m/s

The drag coefficient depends on the shape of the particle and the particle Reynolds number

$$Re_p = \frac{\rho_f v d}{\mu_f} = \frac{v d}{\nu} \tag{3.4}$$

With	d	particle diameter	m
	μ_f	dynamic viscosity	$Pa \cdot s$
	ν	kinematic viscosity	m^2/s

The drag coefficient of a sphere as a function of the Reynolds number is shown in figure 3.1. The drag coefficient for low Reynolds numbers (0.1 - 10) is linear proportional to the sphere velocity and becomes roughly constant for $Re > 1000$ until $Re > 2 \times 10^5$ where the drag coefficient steeply drops of. The drag coefficient has to be determined experimentally, and for random irregular shaped particles can differ drastically between particles.

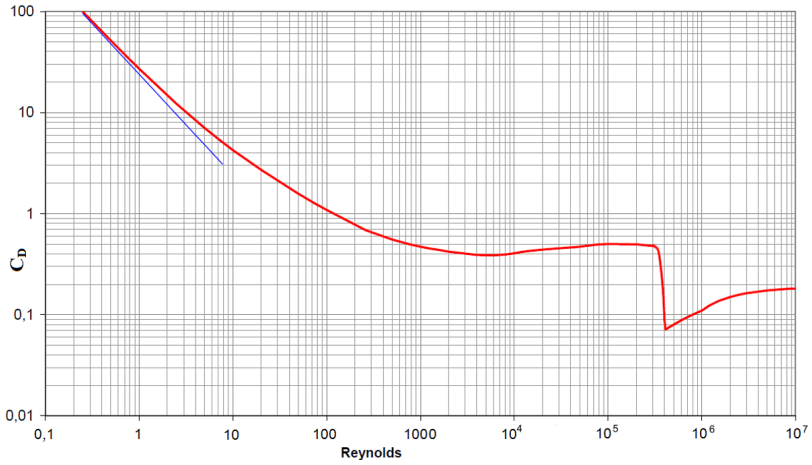

Figure 3.1: Drag coefficient of a sphere as a function of Reynolds number, from Wikimedia (Go Mars, B. de, 2014).

3.2.3 Lift force

If flow is asymmetrical around a particle, the drag force is split in two components, where one (the drag force) is parallel to the flow and the other is perpendicular to the flow. This perpendicular force is the lift force. This asymmetry in the flow around a particle can arise from irregularities in the shape of the particle, unequal flow separation around the particle, the angle of the flow with respect to the particle orientation or rotation. The asymmetry causes a lower pressure on one side of the particle, and this pressure gradient generates the lift force. The Magnus effect is also related to this force (see section 4.3.2).

The lift force in pipelines is most active near the pipe walls where the velocities are highest, but are small in comparison to particle-particle contact forces.

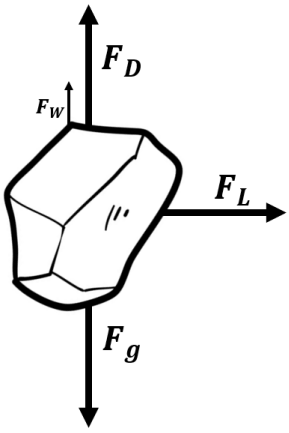

Figure 3.2: Schematics of the forces on a falling rock.

3.2.4 Turbulent diffusive force

Particles are transported through a pipe driven by gravity or a pressure gradient, but locally the particles are picked up by eddies and turbulence in the flow. The effectiveness of this mechanism depends on the size the eddies can attain and this is limited by the pipe diameter. The force from the eddies on the particles can be calculated, but it depends on the value of the solids dispersion coefficient. Determining the value of this coefficient however is a major challenge for determining this force. For the force in a short, inclined, gravity driven pipe with large particles, this force is less of an influence due to the particles size compared to the eddy size.

3.2.5 Coulombic contact force

Particles in inclined pipes slide over the bottom of the pipe in a bed. The contact between the bed and the particles causes a transmission of forces between the particles and the pipe wall. The intergranular shear and normal stress following from this force transfer are related to each other by a friction coefficient. Du Buys applied Coulombs findings on

stress transfer to riverbeds with the relation from equation 3.5. The ratio between shear and normal stress gives the angle of repose ϕ.

$$\tan\phi = \frac{\tau_s}{\sigma_s} = \frac{\tau_s}{\rho_f g \Delta C_{vb} h} \tag{3.5}$$

With	ϕ	angle of repose of the grains	$^\circ$
	τ_s	intergranular shear stress	Pa
	σ_s	intergranular normal stress	Pa
	Δ	Specific density of the solids $\left(\frac{\rho_s - \rho_f}{\rho_f}\right)$	$-$
	C_{vb}	Concentration of the bed	$-$
	h	height of the bed	m

The angle of repose ϕ is the angle at which a granular material starts to move and is dependent mostly on particle size and shape because most of the particles are resting on other particles and only a thin layer rests on the pipe wall. If the angle of the pipe is not steep enough, the particles will not move but rest on the pipe wall. The angle ϕ for wet sand is 45° and for rocks between 30° and 45°.

3.3 Settling velocity of solid particles

3.3.1 Settling velocity of a single particle

The settling velocity of a single submerged sphere is determined by a balance of the gravitational, buoyancy and drag forces. The settling velocity is calculated with

$$w_0 = \sqrt{\frac{4\Delta g d}{3C_D}} \tag{3.6}$$

With	w_0	particle settling velocity	m/s
	Δ	specific density of the solids $\left(\frac{\rho_s - \rho_f}{\rho_f}\right)$	$-$
	g	gravitational acceleration	m/s^2
	d	particle diameter	m
	C_D	drag coefficient	$-$

The drag coefficient C_D depends on the particle Reynolds number, and three regimes can be distinguished: the laminar, transition and turbulent regime. For laminar flows, with low Reynolds numbers, the Stokes equation for settling velocity can be used:

$$w_0 = \frac{\Delta g d^2}{18\nu}. \tag{3.7}$$

Here, ν, is the dynamic viscosity of the liquid. In the turbulent regime, the value for C_D is constant and the velocity is calculated with

$$w_0 = 1.8\sqrt{\Delta g d}. \tag{3.8}$$

In the transition regime, the following relation found by (Ferguson & Church, 2004) can be used, which is valid over a wide range of Reynolds numbers. This equation is also valid for non-spherical particles.

$$w_0 = \frac{\Delta g d^2}{C_1 \nu + \sqrt{0.75 C_2 \Delta g d^3}} \tag{3.9}$$

The coefficient $C_1 = 18$ and $C_2 = 1$ for natural particles and $C_2 = 0.44$ for spheres.

3.3.2 Hindered settling

The equations in section 3.3.1 determine the terminal settling for a single particle falling unrestricted in liquid. However, in rock installation, large masses of stones are used and these rocks influence each other in their fall trajectory in a restricted area. Figure 3.3 illustrates this effect. The settling equation with the influence of the concentration by (Richardson & Zaki, 1954) is

$$w_s = w_0 (1 - c)^n \tag{3.10}$$

with

$$n = \frac{4.7 + 0.41 Re_p^{0.75}}{1 + 0.175 Re_p^{0.75}} \tag{3.11}$$

and	w_s	hindered settling velocity	m/s
	w_0	particle settling velocity	m/s
	c	concentration	$-$
	Re_p	particle Reynolds number	

The coefficient n has values between $n = 4.65$ for very fine particles and $n = 2.4$ for very coarse particles.

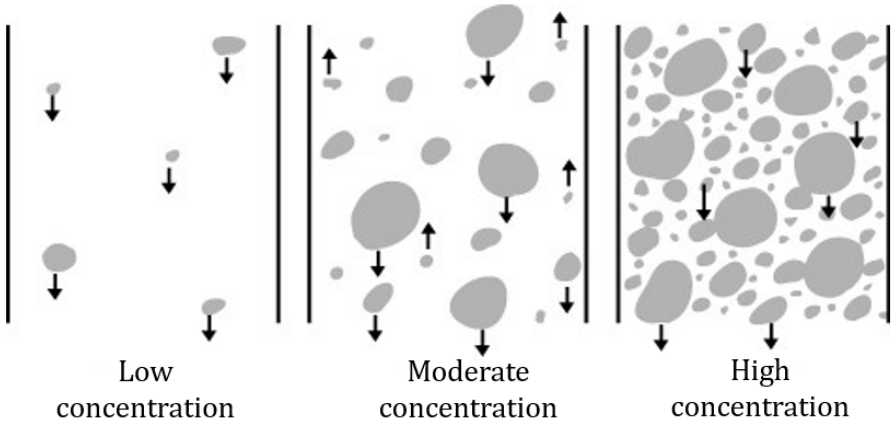

Figure 3.3: Hindered settling, from the Encyclopedia of Sediments and Sedimentary Rocks (Major, 2003).

3.3.3 The wall effect

In vertical pipes, the pipe wall also has an effect on the settling velocity of particles. This effect happens because upward flow of the fluid slows down the downward flow of the particles. The effect depends on the ratio between the particle size and the pipe diameter, and becomes more prominent if the particles are large compared to the pipe diameter, as equation 3.12 shows. In subsea rock installation, the maximum rock diameter is

often limited to one third of the pipe diameter, giving a reduction in settling velocity of approximately 14% (van Rhee, 2018).

$$w_{0,p} = w_0 \left(\left(1 - \lambda_w^2\right) \sqrt{1 - 0.5\lambda_w^2} \right) \quad \text{with} \quad \lambda_w = \frac{d}{D} \tag{3.12}$$

With			
	$w_{0,p}$	particle settling velocity in a pipe	m/s
	w_0	particle settling velocity	m/s
	λ_w	relative particle size	$-$
	d	particle diameter	m
	D	pipe diameter	m

Combining equations 3.10 and 3.12 gives the settling velocity in the pipe:

$$w_{s,p} = w_0 \left(\left(1 - \lambda_w^2\right) \sqrt{1 - 0.5\lambda_w^2} \right) (1 - c)^n \tag{3.13}$$

3.3.4 Settling down an inclined plane

The previous equations in section 3.3 all relate to the vertical settling of particles, but the situation changes when the particles are in contact with a solid boundary. Particles in an inclined pipe show rolling and sliding motions, which increases the drag, as shown by the research of Chhabra, Kumar and Prasad (Chhabra et al., 2000):

$$C_D = 0.861 + \frac{321.906}{Re_p} \tag{3.14}$$

With this correlation for the drag coefficient, the vertical settling velocity for a sphere rolling down an incline is

$$w_\theta = \sqrt{\frac{4gd\Delta}{3C_D} \sin\theta}. \tag{3.15}$$

With			
	C_D	drag coefficient	$-$
	Re_p	Particle Reynolds number	$-$
	w_θ	inclined particle settling velocity	m/s
	Δ	specific density	$-$
	g	gravitational acceleration	m/s^2
	d	particle diameter	m
	θ	incline angle	deg

Chhabra also investigated the dynamics of spheres rolling down smooth planes for the relation between the angle, time and distance to reach their terminal velocity (Chhabra & Ferreira, 1999). First the terminal Reynolds number Re_t is calculated

$$Re_t = \frac{321.906}{2 \cdot 0.861} \left(-1 + \sqrt{1 + \frac{32}{\pi} \frac{1.23}{177.5^2} P \sin\theta} \right) \tag{3.16}$$

With sphere-fluid parameter P

$$P = \left(\frac{\pi d^3}{6} \rho_s g \Delta \right) / \left(\frac{\mu_f^2}{\rho_f} \right) \tag{3.17}$$

The time (t) and distance (x) traveled by the sphere on the inclined plane are obtained by

$$t = 0.774 \cdot \frac{1}{Re_t} \frac{d^2 \rho_s}{\mu_f} \left(1.4 + 2.0 \frac{\rho_f}{\rho_s} \right) \ln \left(\frac{1 + Y}{1 - Y} \right) \tag{3.18}$$

$$x = 0.774 \cdot \frac{d\rho_s}{\rho_f}\left(1.4 + 2.0\frac{\rho_f}{\rho_s}\right)\ln\left(\frac{1}{(1+Y)(1-Y)}\right) \tag{3.19}$$

According to Chhabra, equations 3.16, 3.17, 3.18 and 3.19 together predict that when $Re_t >> 400$, the terminal time and distance are independent of the fluid viscosity and the sphere's motion is predominantly in the constant drag coefficient region. Substituting $Y = 0.99$ for the dimensionless velocity at terminal distance, the upper limit for terminal distance can be calculated with

$$x = 3.03d\left(2.0 + 1.4\frac{\rho_s}{\rho_f}\right) \tag{3.20}$$

For equations 3.16 - 3.20			
	Re_t	terminal Reynolds number	$-$
	θ	incline angle	$^\circ$
	P	sphere-fluid parameter	$-$
	Δ	specific density	$-$
	μ_f	fluid viscosity	$Pa \cdot s$
	ρ_f	liquid density	kg/m^3
	ρ_s	solids density	kg/m^3
	Y	dimensionless velocity	$-$

Research by Wardhaugh and Williams shows that for an angle of 74° from the horizontal, spheres rolling down an incline start to lose contact with the wall, because the hydrodynamic forces act outward from the wall, and at high enough velocity, lift-off occurs. This happened for a wide range of Reynolds numbers and systems (Wardhaugh & Williams, 2014).

Chapter 4

Falling behavior of rocks

4.1 Introduction

In this chapter, first the method of determining the settling velocity of irregular particles is given, then the trajectory particles follow during free fall is detailed and finally the different phases the falling process shows are explained.

4.2 Settling velocity of rocks

In chapter 3 the settling velocities are determined for spherical particles. For non-spherical particles like quarried stone, the drag coefficient is not so easily determined as for a sphere, because of the large variation in the shape and roughness. The drag coefficient is largely dependent on the shape and the length/width (L/d) of the rock. L is the largest distance between two ends of the stone and d the smallest distance perpendicular to L. For his research, Van der Wal determined the drag coefficient of of specific rock grade (van der Wal, 2002). First the individual rock characteristics were determined like mass, volume, density and the L/d ratio. Then the settling velocities of individual rocks and rock groups was determined. With the equation for settling particles $w_0 = \sqrt{\frac{4\Delta g d}{3C_D}}$ the drag coefficient for each individual rock can be determined. The distribution of the drag coefficient as a function of L/d is then calculated with this equation:

$$f_{CD,n}\left(C_{D,n}\right) = \frac{1}{\sqrt{2\pi}\sigma_{CD,n}} e^{\frac{\left(C_{D,n}-\mu_{CD,n}\right)^2}{2\sigma^2_{CD,n}}} \tag{4.1}$$

where

$$\mu_{CD,n} = 0.54\frac{L}{d} + 0.42 \tag{4.2}$$

Van der Wal calculated the drag coefficient as a function of L/d because the rocks tended to fall with their largest face downward and this increased the accuracy of his predictions. Van der Wal determined that the drag coefficient is normally distributed around $\mu_{C_D} = 1.42$ and $\sigma_{C_D} = 0.33$. A side note for his relation is that it is determined on a small selection of rocks and is not universal. Research in settling velocity of rocks has also been carried out by, among others, by (van Oord, 1996). Van Oord came to a drag coefficient of 2.3 for quarried rock and 1.4 for gravel. These measurements where also carried out with relatively small rocks and might not hold for larger scales. They concluded that when the shape deviates farther from spheres, the drag coefficient increases.

4.3 Falling path and motion

The motion and the path of irregular shaped rocks are influenced by various occurring phenomena. These phenomena are described in the next sections.

4.3.1 Vortex shedding

Flow will start to separate from an object at Reynolds numbers from 4000 and above. The vortexes created by the flow separation are shed in a regular manner, alternating from side to side. Theodore von Kármán discovered there is only one stable configuration and therefore this phenomenon is called a Kármán vortex street.

Figure 4.1: A Kármán vortex street behind a cylinder in water (Joseph Straccia, 2016).

The Strouhal number describes the frequency of the vortex separation:

$$St = \frac{fd}{V} \tag{4.3}$$

In the range of $250 < Re_p < 200000$ the following equation written with the Reynolds number is roughly true.

$$St = 0.198\left(1 - \frac{19.7}{Re_p}\right) \tag{4.4}$$

With	St	Strouhal number	$-$
	f	frequency of separation	s^{-1}
	d	sphere diameter	m
	V	flow velocity	m/s
	Re_p	Particle Reynolds number	$-$

The equation for the Strouhal number assumes a sphere and can be written as

$$St = \frac{fd}{V} = 2\frac{\pi d}{TV} \tag{4.5}$$

When the Strouhal number and the velocity are constant, this results in the following for the period of vortex separation:

$$T = \frac{2\pi\sqrt{d}}{St\sqrt{\frac{2\Delta g}{C_D}}} \tag{4.6}$$

Particles falling downwards through a fluid experience horizontal fluctuations actuated by vortex separations. The period of vortex separation (T) can be used to calculate the horizontal distance traveled by a falling sphere:

$$S_{hor} = \frac{1}{2} g T^2 = \frac{\rho_f}{\rho_s} \frac{\pi^2}{St^2} C_L d \tag{4.7}$$

If the vertical distance between the release point and the bed and the vortex separation period are known, the amount of horizontal fluctuations can also be calculated:

$$N = \frac{h}{S_{ver}} = \frac{h}{2\pi d} St \tag{4.8}$$

With	Δ	specific density	$-$
	T	vortex separation period	s
	g	gravitational acceleration	m/s^2
	C_D	drag coefficient	$-$
	S_{hor}	horizontal distance traveled due to vortex separation	m
	ρ_f	liquid density	kg/m^3
	ρ_s	solid density	kg/m^3
	C_L	lift coefficient	$-$
	N	amount of horizontal fluctuations in the fall trajectory	$-$
	h	fall height	m
	S_{ver}	vertical distance traveled during a single vortex period	m

Equation 4.6 shows that the time between two direction changes is proportionate with the square root of the diameter of the particle or rock. The fluctuation larger rocks experience are larger in distance, but they experience fewer fluctuations than smaller rocks. The random walk model developed by Vrijling, Manni and De Wilde (Vrijling et al., 1995) is based on this principle. Section 4.3.3 elaborates on this model.

4.3.2 Magnus effect and asymmetrical separation

If an object moves through a fluid while rotating, a lift force is formed perpendicular to the direction of motion. This is called the Magnus effect. Friction between the (spherical) object and the fluid causes the fluid to rotate with the object. This creates a velocity difference between two opposing sides of the sphere. The consequence of this is a pressure difference between the top and the bottom, where the higher pressure is at the bottom of the sphere. The resulting force of this pressure difference is a lift force perpendicular to the direction of motion.

A similar effect can occur when an object has a smooth and a rough side. The boundary layer flow on the smooth side will be in the laminar regime and will separate faster than the flow on the rough side. This asymmetrical separation lead to an asymmetrical pressure distribution. This leads to rotation, which can lead to the Magnus effect.

4.3.3 Random walk model

Vortex shedding on a rock happens randomly over the surface of the rock because rocks are irregular shaped and their orientation changes continuously with respect to the flow. The rock will move in a random direction in a plane perpendicular to the falling direction. The sum of all horizontal displacements is the total horizontal displacement at a certain depth.

When the total horizontal displacement of a large amount of falling rocks with similar characteristics is considered, statistics can be used to predict the displacement of a falling rock.

The Random Walk model gives a statistical description of the falling motion of a single piece of rock. Vrijling, Manni and De Wilde described it extensively in their paper 'Prediction of the deposition-mound of dumped rubble' (Vrijling et al., 1995). The single stone model is a model to predict the position of a rock when it hits the bed (Cregten, 1995). The most important steps of the model are detailed here.

The separation of vortexes is periodical and is described with the Strouhal number. Each vortex period has a random horizontal displacement. This displacement is a consequence of a lift force generated by the asymmetrical separation.

The horizontal distance a rock travels per vortex period is given by the same formula as for a sphere (equation 4.7), but with a correction factor (y') for the rock shape:

$$S_{hor} = \frac{1}{2} g T^2 = \frac{\rho_f}{\rho_s} \frac{y'}{St^2} C_L d \tag{4.9}$$

The sum of all horizontal fluctuations over the falling trajectory gives the total horizontal displacement at the bottom. The total standard deviation for this process is calculated by summing the individual standard deviations for each horizontal fluctuation. Here σ_N denotes the standard deviation of the total process and σ_i is the standard deviation for an individual fluctuation.

$$\sigma_N^2 = n \sigma_i^2 \tag{4.10}$$

The individual standard deviation σ_i must be determined by measuring the fluctuations during a rock dumping tests.

Equation 4.8, 4.9, and 4.10 can be combined to give an equation for the standard deviation of a falling rock in water:

$$\sigma_G = \frac{y'}{\sqrt{St^3}} \frac{\rho_f}{\rho_s} C_L \sqrt{hd} \tag{4.11}$$

Here, σ_G is the standard deviation of the sum of N independent horizontal displacements.

This can be simplified to

$$\sigma_G = c \sqrt{d_{n50} h} \tag{4.12}$$

Meermans (Meermans, 1997) simplified the three-dimensional behavior of falling rocks by supposing the rocks fall between two parallel plates. The rocks then spread with a Gaussian probability distribution. The two-dimensional probability density for a Gaussian profile is given by:

$$f_x(x) = \frac{1}{\sqrt{2\pi}\sigma_G} e^{-\frac{1}{2}\left(\frac{x-\mu_x}{\sigma_G}\right)^2} \tag{4.13}$$

By multiplying the probability density function in the x- and y-direction the three-dimensional probability density distribution is acquired:

$$f_{xy}(x,y) = \frac{1}{2\pi\sigma_D^2} e^{-\frac{1}{2}\left(\frac{(x-\mu_x)^2+(x-\mu_y)^2}{\sigma_D}\right)} \tag{4.14}$$

4.3.4 Offset model

The offset model was originally developed to evaluate the behavior of rock falling in flow from rivers or tides. In an equilibrium the horizontal component of the rock's velocity will become equal to the flow's velocity. A rock falling out of an inclined fall pipe also has a horizontal component due to its direction, and mathematically, flow around an object and a moving object in stationary liquid are the same. The horizontal component will diminish quickly as the stones exit the pipe because there is no horizontal driving force.

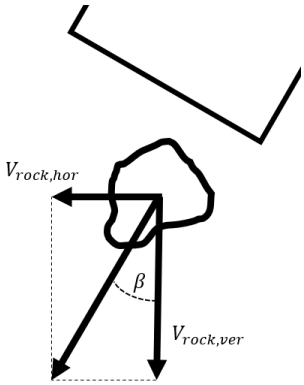

Figure 4.2: Schematics of particle velocity in the offset model.

The offset model starts with the horizontal force working on a rock:

$$F_V = \frac{1}{2}\rho_f C_L \left(V_{rock,hor} - V_{rock,ver}\right)^2 \tag{4.15}$$

Using Newton's second law gives the horizontal acceleration of a falling stone

$$\frac{dV_{rock}}{dt} = \frac{A_s}{2V_s}\frac{\rho_f}{\rho_s - \rho_f} C_L \left(V_{rock,ver} - V_{rock,hor}\right)^2 \tag{4.16}$$

Solving this differential equation gives the rock's direction of falling (w is the vertical settling velocity)

$$\tan\beta = \frac{V_{rock,hor}}{w} \tag{4.17}$$

Using these equations a model for the offset of the rock to the center of falling was developed by WL — Delft Hydraulics (Waterloopkundig-laboratorium, 1983). This model gives the offset due to horizontal velocity:

$$\text{Offset} = h\frac{V}{w} = h\frac{\sqrt{0.5C_D}\bar{V}}{\sqrt{gd_n\Delta}} \tag{4.18}$$

Here,	F_V	horizontal force	N
	ρ_f	liquid density	kg/m^3
	C_L	lift coefficient	$-$
	V_{flow}	horizontal flow velocity	m/s
	V_{rock}	horizontal stone velocity	m/s
	A_s	projected stone area	m^2
	V_s	stone volume	m^3
	ρ_s	solid density	kg/m^3
	β	stone falling direction	deg
	w	stone settling velocity	m/s
	h	falling height	m
	C_D	drag coefficient	$-$
	$\bar{V}$	depth averaged flow velocity	m/s
	g	gravitational acceleration	m/s^2
	d_n	stone diameter	m
	Δ	specific density	$-$

The offset model and the single stone model can be combined to give the probability density distribution the position of the rock due to falling and a horizontal velocity

component.

$$f_X(x) = \frac{1}{\sigma_D\sqrt{2\pi}} e^{-\frac{1}{2}\left(\frac{x-h\frac{\sqrt{0.5C_D}\bar{V}}{\sqrt{gd\Delta}}}{\sigma_D}\right)^2} \tag{4.19}$$

Equation 4.14 and equation 4.19 can be combined for

$$f_X(x) = \frac{1}{\sqrt{2\pi h d_n}} e^{-\frac{1}{2}\left(\frac{x}{\sqrt{hd_n}} - \frac{\sqrt{0.5C_D}\bar{V}}{d_n\sqrt{g\Delta}}\right)^2} \tag{4.20}$$

4.4 Fall behavior of a group of stones

4.4.1 Two-phase principle

G. W. Slack (Slack, 1963) conducted experiments where a large number of small glass spheres was released simultaneously. He observed first that the spheres first fell in a spherical group where the group velocity was higher than the equilibrium velocity of the individual particles. In these particle clusters, the particles started to rotate from the center to the outside and when the group velocity was high enough, the cluster transformed to a bowl shape. This behavior shows similarities to masses of moist air forming clouds, hence the name ”thermal phase”.

Bühler and Papantoniou (Papantoniou & Buhler, 1999) described a second phase following this where the group velocity is nearly equal to the equilibrium velocity of the individual particles. This is called the swarming phase. The width of the swarm increases with the square root of the depth (Papantoniou & Buhler, 1999). These observation show similarities with the Single Stone model developed by Vrijling (Vrijling et al., 1995). The falling velocity of the group in this phase is limited by the maximum velocity of the single rocks.

4.4.2 Five-phase principle

Van der Wal distinguishes five phases for rock groups with a long enough fall trajectory (van der Wal, 2002):

1. Acceleration phase
2. Deceleration phase
3. Disintegration phase
4. No influence phase
5. Radial runoff phase (only if phase one or two is active)

The first phase is can be characterized as a group of stones that forms a whole with the entrained water. The maximum velocity of this group is larger than the velocity of a single rock, with a longer acceleration trajectory. The length and width of the group increases over time and the relative density decreases. The acceleration reduces until the equilibrium velocity is reached. This marks the end of phase one.

The second phases starts directly when the velocity has reaches is peak, and the group starts to decelerate. More water is entrained in the group and the group effect becomes smaller until the larger rocks in the group start to leave the group. This is the end of phase two.

The third phase happens when rocks start to leave the group. The larger rocks take smaller rocks with them in their wake.

In the fourth phase, the rocks do not influence each other and follow the processes of singular settling particles.

The fifth phase starts when rocks start to hit the floor. If the rocks are still in the first or second phase with group effects, a radial outflow effect will occur. The entrained water contains kinetic energy and will deflect and flow away along the floor. The rocks will flow with the water and will deposited farther away. Phase five can only occur if the height of the release point is too low.

The first four phases are a further distinction of the two phases recognized by Slack. The first two phases are part of the thermal phase and the third and fourth phase are part of the swarming phase. In that sense, phase five is not really a phase but an effect that occurs when the falling distance is too short.

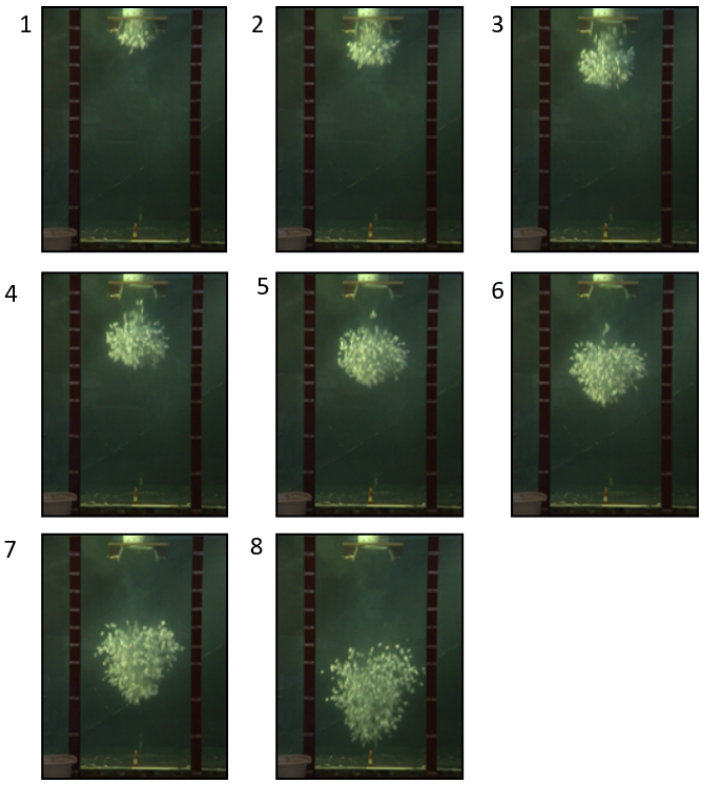

Figure 4.3: A series of images of the falling process during a test by Van der Wal, clearly showing the first four phases (van der Wal, 2002).

Chapter 5

Flow in inclined pipes

5.1 Introduction

In this chapter flow in inclined pipes is explained. Flow in inclined pipes can be described with a two-layer model. The content in this chapter is based on the lecture notes ”Dredging Pumps and Slurry Transport” by (Matoušek & Talmon, 2021) and ”Flow Mechanism of Sand-Water Mixtures in Pipelines” by (Matoušek, 1997). This slurry transport theory is applicable to rock installation in the sense that it explains two-layer flow in a pipe, but the particle size difference between rock dumping and sand transport is very large and might not scale.

5.2 The two-layer model

Sand, gravel and rocks transported through horizontal, positively or negatively inclined pipes undergo stratification because the particles will settle in the flow and the larger the particle, the faster it settles. The upper part of the pipe lacks particles, and the lower part contains most of the transported particles. The thickness of the layer depends on the amount of material transported and the velocity of the flow.

5.2.1 Principles of the two-layer model

The two-layer model separates the concentration profile in the pipe in two separate parts: the upper part purely consists of the carrier fluid and the lower part is a mixture of particles and the carrier fluid. The particles are also considered to be in contact with each other and not in suspension. Figure 5.1 shows a sketch of the two-layer model, where angle β characterizes the height of the interface between bed and liquid.

The two-layer model assumes two physical mechanisms are responsible for solid particle support: interparticle contact and particle suspension in the carrier fluid. In the two-layer model this translates to the assumption that the submerged weight of the particles in suspension is loaded fully in the carrying fluid and the submerged weight of the particles on the bed is fully loaded on the pipe wall.

The behavior of the flow is governed by a force balance between the driving and the resisting forces in the two layers. The driving force for slurry transport is caused by a pressure gradient over the pipe length, but rock installation with an inclined pipe is driven by gravity. The resisting force comes from the interface between the rock bed and the water, between the rocks and pipe, and the water and the pipe.

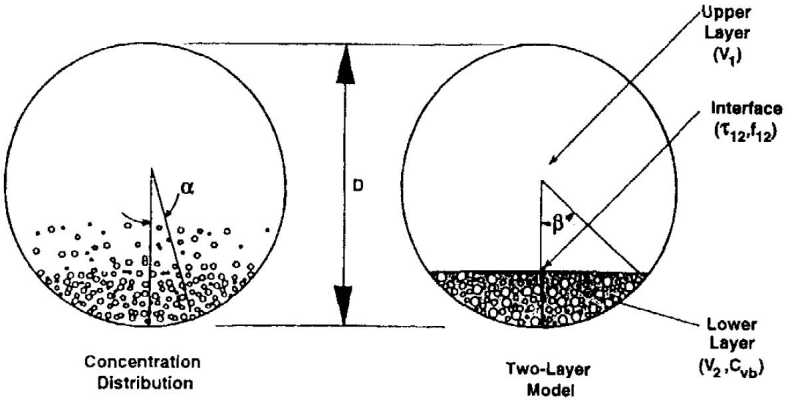

Figure 5.1: Definition sketch for two-layer model of stratified flow, after (Wilson et al., 1992)

The two-layer model consists of sets of equations of conservation of mass and conservation of momentum in both layers of the flow in a pipe section. The equations assume a control volume of length dx and steady and uniform flow. As seen in figure 5.2, the subscript 1 refers to the top layer and subscript 2 refers to the bottom layer. The mass balance and the momentum balance are given in the next two sections.

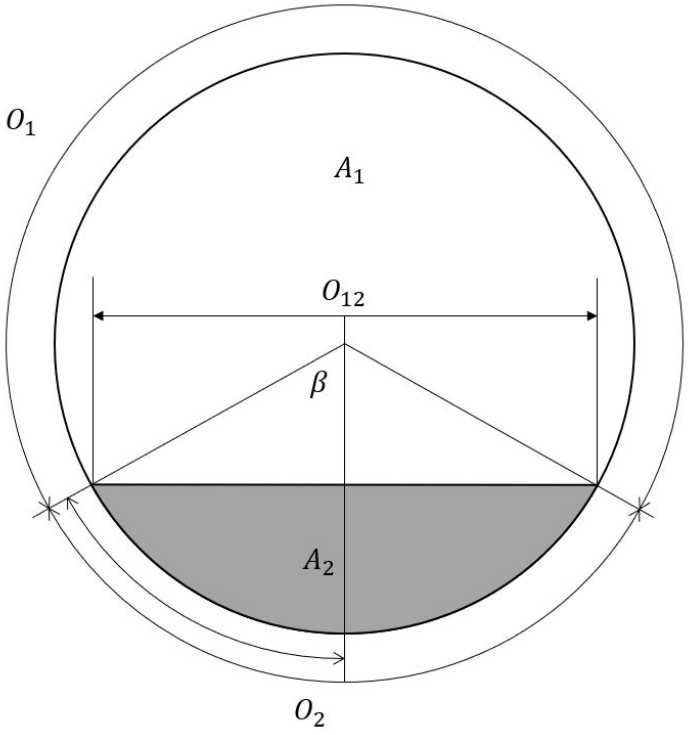

Figure 5.2: Schematic cross-section for the two-layer model

5.2.2 Mass balance for two-layer flow

Applying the law of conservation of mass to a two-layer flow yields the following balances, where the subscript 1 refers to the top area of the pipe and the subscript 2 to the bottom part of the pipe.

Mixture flow rate

$$\begin{aligned} Q_m &= Q_{m1} + Q_{m2} = \text{constant} \\ v_m A &= v_1 A_1 + v_2 A_2 \end{aligned} \tag{5.1}$$

Solids flow rate

$$\begin{aligned} Q_s &= Q_{s1} + Q_{s2} = \text{constant} \\ v_s A_s &= C_{vi} v_s A = C_1 A_1 v_1 + C_2 A_2 v_2 \end{aligned} \tag{5.2}$$

and for liquid flow rate:

$$\begin{aligned} Q_f &= Q_{f1} + Q_{f2} = \text{const.} \\ v_f A_f &= (1 - C_{vi})\, v_f A = (1 - C_1)\, A_1 v_1 + (1 - C_2)\, A_2 v_2 \end{aligned} \tag{5.3}$$

The solids volume balance

$$C_{vi} = C_1 A_1 + C_2 A_2 \tag{5.4}$$

because $C_{vd} = Q_s / Q_m$, equation 5.2 can be rewritten as

$$C_{vd} A v_m = C_1 A_1 v_1 + C_2 A_2 v_2 \tag{5.5}$$

With	Q_m	mixture volumetric flow rate	m^3/s
	Q_s	solids volumetric flow rate	m^3/s
	Q_f	fluid volumetric flow rate	m^3/s
	v_m	mixture velocity	m/s
	v_s	solids velocity	m/s
	v_f	fluid velocity	m/s
	A	pipe cross-section area	m^2
	C	volumetric solids concentration	$-$
	C_{vi}	spatial volumetric solids concentration in pipe cross section	$-$
	C_{vb}	volumetric solids concentration in the bed	$-$
	C_{vd}	delivered volumetric solids concentration	$-$

5.2.3 Momentum balance for two-layer flow

In a pipeline section L, the conservation of momentum is a force balance between the driving forces (gravity for rock installation) and the resisting forces on boundary layers of the flows, i.e. the water on the pipe wall in the upper layer, the water-rock interface and rock bed on the pipe bottom. There is viscous friction between the liquid layer and the pipe wall and bed and mechanical friction between the pipe and the solid particles. Because the pipe is submerged in water, and the driving forces only work on the lower layer, only the lower layer needs to be considered for the momentum balance in the inclined pipe. This part of the momentum balance from (Miedema, 2019) is:

$$\frac{\rho_m V_2 g}{\Delta L} - \frac{dP}{dx} A_2 = \tau_2 O_2 - \tau_{12} O_{12} + W_b \sin\theta + \mu_{sf} W_{b,s} \cos\theta \tag{5.6}$$

Part of thee term on the left can be simplified to $\frac{\rho_m V_2 g}{\Delta L} = \rho_m g A_2$.

With	V_2	volume of the lower layer	m^3
	ρ_m	density of the mixture in the lower layer	kg/m^3
	g	gravitational acceleration	m/s^2
	P	pressure	Pa
	θ	pipe angle	$^\circ$
	O_{12}	perimeter layer interface	m
	O_2	perimeter of the lower layer	m
	τ_{12}	shear stress at boundary O_{12}	Pa
	τ_2	shear stress at boundary O_2	Pa
	W_b	weight of the bed	kg
	$W_{b,s}$	submerged weight of the bed	kg
	ΔL	pipe section length	m

5.2.4 Mechanical friction

The solid particles are in direct contact with each other and with the pipe wall, and transmit their submerged weight to the pipe wall. This mechanical friction acts as a resisting force opposite the driving forces. This boundary frictional resistance depends on the interparticle stress σ_s. The stress acts normal to the pipe wall. Wilson gives the stress for a granular layer as follows:

$$\sigma_s = g\left(\rho_s - \rho_f\right) C_{vb} \frac{D}{2} \left(\cos\alpha - \cos\beta\right) \tag{5.7}$$

With	σ_s	normal stress of solids	$kg/m/s^2$
	g	gravitational acceleration	m/s^2
	ρ_s	solids density	kg/m^3
	ρ_f	fluid density	kg/m^3
	C_{vb}	volumetric solids concentration in the bed	$-$
	D	pipe diameter	m
	β	angle defining the interface position (see fig. 5.2)	$^\circ$
	α	angle defining a position in the pipe cross-section and half of β	$^\circ$

The normal stress σ_s produces the intergranular stress $\tau_s = \mu_s \sigma_s$. μ_s is the mechanical friction coefficient between the solids and the pipe wall. The total resisting force of the bed is

$$\mu_s F_N = \tau_{2s} O_2 = \mu_s \sigma_{s,mean} O_2 \quad \text{for} \quad O_2 = D\beta \quad \text{and} \quad \sigma_{s,mean} = \frac{1}{\beta}\int_0^\beta \sigma_s \, d\alpha \tag{5.8}$$

The total normal force F_N against the pipeline wall can be obtained by integrating the normal stress over pipeline perimeter O_2. F_N is then

$$F_N = g\left(\rho_s - \rho_f\right) C_{vb} \frac{D^2}{2} \left(\sin\beta - \beta\cos\beta\right) \tag{5.9}$$

The normal force F_N is different from the submerged weight of the bed, referred to as F_w, which represents the gravitational effect on the bed and is integrated from the stress component σ_w. The difference between F_N and F_w comes from their directions. F_N acts orthogonal to the pipe wall at all points on O_2 and F_w always acts in the direction of gravity. In an inclined pipe this is:

$$F_w = g\left(\rho_s - \rho_f\right) C_{vb} A_2 \sin\theta \tag{5.10}$$

where θ is the angle of the pipe with respect to the horizontal.

5.2.5 Viscous friction

The viscous friction between the water and the pipe wall, and the water and the particle layer depends on the velocity of the layers.

Shear stress and the velocity difference between the liquid and the flow boundary are related by a friction coefficient expressing flow conditions at the boundary called the Darcy-Weisbach friction coefficient. The flow conditions follow from the flow regime (i.e. laminar, turbulent) and the roughness of the pipe wall and the particle layer. The Darcy-Weisbach friction coefficient is defined as

$$\lambda = \frac{8\tau_0}{\rho V^2} \tag{5.11}$$

With	λ	Darcy-Weisbach friction coefficient	$-$
	τ_o	bed shear stress	$kg/m/s^2$
	ρ	density of the layer	kg/m^3
	V	velocity of the layer	m/s

The determination of the viscous shear stress depends on the friction coefficient, the velocity difference at the boundary and the density of the fluid. The friction coefficient is also related to the Reynolds number of the flow and the boundary roughness.

The friction coefficient for water flow can be obtained from the Moody diagram. The flow's Reynolds number is calculated with the hydraulic diameter D_h of the respective layer.

$$Re = \frac{VD_h\rho_f}{\mu_f} \quad \text{with} \quad D_{h1} = \frac{4A_1}{O_1} \text{ or } D_{h2} = \frac{4A_2}{O_2} \tag{5.12}$$

The friction coefficient λ_1 is the friction coefficient in the top layer over the pipe wall indicated by O_1, λ_2 for the bottom layer over the pipe wall O_2 and λ_{12} is for the interface between the layer O_{12}.

Wilson and Brown (Wilson & Brown, 1982) proposed a method for determining λ_2 based on experiments with granular plug flow in a 26 mm pipe. Their analysis of the liquid velocity distribution transformed the theoretical velocity profile in a relation between the liquid friction coefficient λ_2 and the Reynolds number Re_d of the plug. These results gave the friction coefficient in two regimes. For the laminar regime ($Re_d < 335$):

$$\lambda_2 = \frac{22}{Re_d} \tag{5.13}$$

and for the turbulent regime ($Re_d > 335$):

$$\lambda_2 = 0.033\left(1 + \frac{138}{Re_d}\right)^2 \tag{5.14}$$

As an alternative method, the friction coefficient λ_2 can also be determined with the Moody diagram for the Reynolds number Re of the particle layer and the pipe roughness k.

The coefficient λ_{12} is the friction coefficient for the interface between the two layers in the flow. If the interface can be assumed to be as a flat surface of the bed, the roughness can be considered to be proportional to the diameter of the particles of the bed. Wilson

(Wilson, 1976) proposed using Nikuradse's friction equation with the effective roughness k replaced with the d_{50} and multiplying the λ with an empirical coefficient of 2.

$$\lambda_2 = \frac{1}{\left(2\log\frac{D}{k} + 1.138\right)^2} \tag{5.15}$$

Gillies (Gillies et al., 1991) proposed the following equation

$$\sqrt{\frac{8}{\lambda_{12}}} = \frac{4\log\frac{D}{d_{12}} + 3.36}{\sqrt{0.5 + X}} \tag{5.16}$$

in which $X = 5 + 1.86\log\frac{d_{12}}{D}$ for $d_{12}/D > 0.002$ and $X = 0$ otherwise. d_{12} is the diameter of the particles at the interface. Gillies assumption is that the smallest particles in the flow are at the surface and that all particles larger than the particles at the surface layer have settled lower than d_{12}.

With the forces calculated in 5.2.4 and the friction coefficients calculated in this section, the balances from 5.2.2 and 5.2.3 can be calculated.

Chapter 6

Scaling effects for tests with falling stones

6.1 Introduction

A physical model is a small scale representation of a real world prototype and is used as a tool to provide a clear view of all processes, while only taking up limited space and limiting the costs. So called scale effects originate from the fact that not all processes can be scaled down satisfactory. Recognizing which scale effects can occur increases the accuracy of the analysis of the test results.

The scale for the ratio between model and prototype defined as

$$\alpha_X = \frac{X_m}{X_p} = \frac{\text{Value of X in model}}{\text{Value of X in prototype}}. \tag{6.1}$$

6.2 Scaling rules

According to Van der Schriek and Van Rhee, three rules are applicable when scaling processes between prototype and model scale (van der Schrieck & van Rhee, 2010):

1. The scale of the product of two parameters is equal to the product of the scales of two parameters.
2. The scale of the sum of two parameters is equal to the scale of either of the parameters, provided the scale of the two parameters is equal.
3. A non-dimensional constant has the same value in at model and at prototype scale.

6.3 Similarity

A model is completely similar to the prototype and shows no scale effects if it adheres to three requirements (Heller, 2011; Hughes, 1993):

- geometric similarity,
- kinematic similarity,
- dynamic similarity.

For geometric similarity, all dimensions are scaled with the same factor, preserving shape. Kinematic similarity follows from geometric similarity and indicates that the motions of model and prototype are the same. The ratios between time, velocity, acceleration and discharge must stay constant. Finally, dynamic similarity requires that the ratios between all forces in model and prototype scale are the same.

6.3.1 Froude similarity

Froude similarity is the scaling rule most often used in hydraulic modeling. The Froude number gives the ratio between the force of inertia and the force of gravity on an object. the force of inertia is the product of the mass and acceleration of an object, while the gravitational force is the product of the mass and gravitational acceleration on the object:

$$Fr^2 = \text{inertial force/gravitational force} = \frac{(\rho L^3)(v^2/L)}{(\rho L^3)g} = \frac{v^2}{gL} \tag{6.2}$$

$$Fr = \frac{v}{\sqrt{gL}} \tag{6.3}$$

Froude similarity is achieved if $Fr_m = Fr_p$ or $\alpha_F r = 1$. The Froude scaling rule is the

$$\alpha_v = \sqrt{\alpha_g \cdot \alpha_L} \tag{6.4}$$

As long as the model tests are not taking place in a centrifuge, $g_m = g_p$ and the scaling rule simplifies to $\alpha_v = \sqrt{\alpha_L}$. Applying this to other parameters like mass and time gives

Length scale	$\alpha_L = \alpha$
Velocity scale	$\alpha_V = \alpha^{1/2}$
Mass scale	$\alpha_m = \alpha^3$
Time scale	$\alpha_t = \alpha^{1/2}$

These scaling rules indicate how the parameters of the test change in comparison to the model scale. For example, if the dimensions are scaled with a factor of $\alpha = 15$, then the velocity is scaled with a factor of $\alpha_V = \sqrt{15}$.

6.3.2 Reynolds similarity

Reynolds similarity is important if viscous forces dominate, for example in laminar boundary layer problems. The Reynolds number gives the ratio between the inertial force and the viscous force (de Vries, 1977):

$$Re = \text{inertial force/viscous force} = \frac{(\rho L^3)(v^2/L)}{(\eta v L^{-1})L^2}\frac{\rho u L}{\eta} = \frac{vL}{\nu} \tag{6.5}$$

The Reynolds scaling rule is $\alpha_v = \alpha_L^{-1}$, which is unwieldy in the case of subsea rock installation model tests because the ratio for velocity is α_V^{-1} which means that a rock with a velocity of 1 m/s in real life has to have a velocity of 15 m/s at a scale of 15:1.

Nevertheless, the Reynolds number can be used to give a lower bound to particle size. The flow in a fall-pipe is strictly in the turbulent regime, where the drag coefficient is mostly constant. Using that, the Reynolds number can be rewritten to

$$d^{3/2} = \frac{Re \cdot \nu}{\left(\frac{4\Delta g}{3C_D}\right)^{1/2}}. \tag{6.6}$$

Then, using a Reynolds number of $Re > 1000$ and a drag coefficient of 1.42 as determined by (van der Wal, 2002) and substituting this in equation 6.6, a minimum particle diameter of 6.4 mm is determined.

6.4 Other dimensionless numbers

In addition to the Froude and Reynolds numbers, there are a more dimensionless numbers considered in hydraulic experimentation, but these numbers are often only considered in very specific situations, or are difficult to keep the same between scales. These numbers are:

- The Weber number

$$We = \text{inertial force/surface tension force} = \frac{\rho V^2 L}{\sigma} \tag{6.7}$$

- The Cauchy number

$$Ca = \text{inertial force/elastic force} = \frac{\rho V^2}{E} \tag{6.8}$$

- The Euler number

$$Eu = \text{pressure force/inertial force} = \frac{p}{\rho V^2} \tag{6.9}$$

- The Strouhal number

$$\begin{aligned} St &= \text{temporal inertial force/convective inertial force} = \frac{\left(pL^3\right)(V/t)}{\left(\rho L^3\right)\left(V^2/L\right)} \\ &= \frac{L}{Vt} \end{aligned} \tag{6.10}$$

The Weber number deals with surface tension and is important for air entrainment and capillary waves, but model based on the Weber number haven't been built yet (Heller, 2011). The Cauchy number considers compression of the fluid and is especially important for wave impacts. The Euler number is used for high pressure in pipes or for cavitation in turbines. The Strouhal number is important for unsteady, oscillating flows. All these situations do not occur in or below fall pipes.

6.5 From reality to model

[redacted]The model is scaled down linearly from the prototype to fit in the laboratory tank (see chapter 7) because the Froude criterion is leading. The gravitational and inertial forces are the dominating factors in the processes in the pipe.

The limiting factors in determining the scale are the depth of the tank (2m) and the minimum rock diameter required for turbulent flow. The other factor in determining scale is the closeness to reality: the larger the model is, the closer it is to the prototype and the smaller the scale effects. Taking these factors into consideration, the chosen scale factor is 15.

The scaled down parameters for the tests are :

[redacted]

Chapter 7

Carrying out model tests

7.1 Introduction

In this chapter, the execution of the tests in the Dredging Lab of the faculty of Mechanical, Maritime and Materials Engineering is described. The test setup and the method of testing is explained, and a step-by-step plan of the tests is described.

7.2 Model test setup

The tests were carried out in the Dredging Lab of the faculty of Mechanical, Maritime and Materials Engineering. The lab's large tank was used with dimensions (lxbxh) of 5 m x 2.5 m x 2.15 m. The setup consists of the tank filled with water, a scaffold with a conveyor belt, a hopper, a pipe and a cement tub with metal grating.

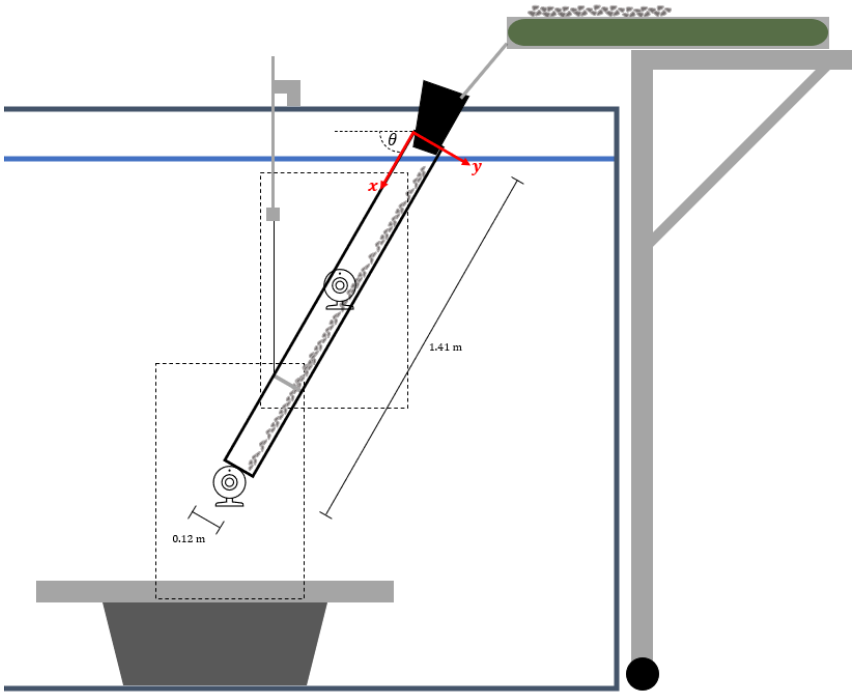

Figure 7.1: A sketch of the test setup

The pipe is located roughly in the middle of the right half of the tank due to the construction of the tank and framing of the video cameras. The two cameras are placed

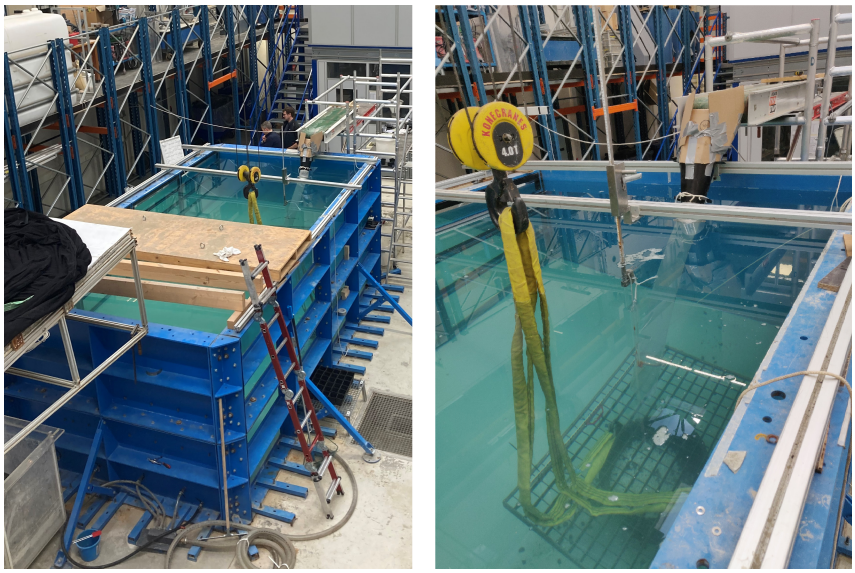

Figure 7.2: Overview of the test setup

in a way where one frames the pipe and the other frames the area between the pipe and the cement tub. The tests are recorded with these video cameras (GoPro) and analyzed with the open source MATLAB application PIVlab (Thielicke & Sonntag, 2021). PIVlab is an Particle Image Velocimetry application used to measure the velocity and displacement of suspended particles.

7.2.1 Pipe

The pipe used for all tests is a clear Polymethyl methacrylate (PMMA) pipe with a diameter of 120 mm and a length of 1410 mm. The lower end of the pipe is suspended with a rope from the beam across the tank, and the pipe is attached at the upper end to the hopper with ropes. Cardboard is taped to the hopper to reduce spillage from the open chute from the conveyor belt. The angle of the pipe can be changed by lowering and raising the hook it is attached to and by changing the position of the beam. The pipe is marked with stripes every ten centimeters.

Figure 7.3: Pipe close-up

7.2.2 Water tank

The tests are carried out in a large, modular metal and glass tank. The dimensions of the tank are 5 m x 2.5 m x 2.15 m. The tank is built with steel wall elements and glass panel elements and can be reconfigured to different setups. During the tests, the water level is at 1.85 m, so the pipe is as much submerged as possible and the water used is tap water. Beams are fitted on the edges of the tank to support the beam across for the pipe.

7.2.3 Conveyor belt

The conveyor belt is placed on a scaffold on the short side of the tank to give a good clear view of the pipe through the side of the tank. The belt has a width of 40 cm and a length of 150 cm. The conveyor belt has an adjustable speed, but the velocity was kept constant at 0.085 m/s to ensure similarity between tests.

7.2.4 Cement tub

The rocks were collected in a cement tub on the floor of the tank. The cement tub was covered in a large metal grate. The grate is connected to the cement tub with bolts and eyes for the crane slings. The grate also ensures that the cement tub does not buckle during lifting. The height of the cement tub with the grate is 39 cm and the holes are 6.5 cm.

For four tests the cement tub has been replaced with a grid with small containers on it to accurately measure the spread of the rocks.

7.2.5 Cameras

Two cameras have been used to record all tests, where one recorded the pipe and the other recorded the area between pipe and tub. The camera recording the pipe was a GoPro Hero 9 Black and the other camera a GoPro Hero 4 Silver. Both cameras recorded with a resolution of 1080p and 60 frames per second. No extra lighting was used to illuminate the tank except for the lighting in the laboratory.

7.2.6 Software

Three applications were used on the recorded footage: Handbrake to rotate the images and convert the codec to one readable by MATLAB, PIVlab, a MATLAB toolbox for PIV-analysis and PotPlayer for frame by frame video analysis.

Particle image velocimetry

Particle image velocimetry (PIV) is a non-intrusive method to measure particle velocity in fluids. A camera records the particle motion and the displacement between video frames is quantified by image cross-correlation. The displacement over time (between frames) yield the velocity of the particles (Thielicke & Sonntag, 2021). PIVlab is a free, and the most popular toolbox in MATLAB with an easy to use GUI. The goal of PIVlab is to make PIV-analysis more accessible to researchers.

7.2.7 Rocks and grading

For the experiments, three types of rock were used. The rock specifications are:

Rock type	*Size*	*Density*
Carrera Marble	8-12 mm	2711 kg/m^3
Petit Granit	12-16 mm	2670 kg/m^3
Basalt	16-32 mm	2900 kg/m^3

[redacted]The smaller two rock types represent the upper

Figure 7.4: A sample of the rocks used in the experiments

and the lower half of the 5 - 40 kg grading and the basalt is scaled for the 60 - 300 kg grading. Figure 7.4 shows a small sample of the rocks used.

7.3 Methodology of the tests

7.3.1 Intent of the tests

The idea of the tests is to observe the behavior of the rock flow in and below the inclined fall-pipe. The tests are carried out in a wide range of parameter configurations, where the pipe angle, the rock size and mixture, and the production are varied. The parameters are given in table 7.1.

Parameter					
Angle	90°	75°	60°	45°	30°
Production	0.64 kg/s	0.48 kg/s	0.32 kg/s	0.16 kg/s	
Rock size	16-32 mm	12-16 mm	8-12 mm	8-16 mm	

Table 7.1: Test parameters

[redacted]

The choice has been made for a wider range of angles with large intervals because it is expected the difference between small differences in angles are not very large, and a larger range of angles gives a better picture when numerical models are going to be made of the rock flow.

[redacted]

The typical rock grading expected to be used with the inclined fall-pipe is 5-40 kg, which at scale is 8-16 mm. The grading has been split in two fractions for most tests, 8-12 mm and 12-16 mm, to investigate the behavior of the smaller and larger rocks. Tests were also performed with a mixture of the rocks for an accurate representation of real operations. After suggestions during testing it was also decided to perform tests with larger rocks of 16-32 mm which correspond to a rock grade of 40-300 kg, in case works have to be completed with larger armor stones. The range is a bit wider than the range of rocks used in realit (60-300 kg) due to the rocks available at scale.

See also appendix A for a list of all tests carried out.

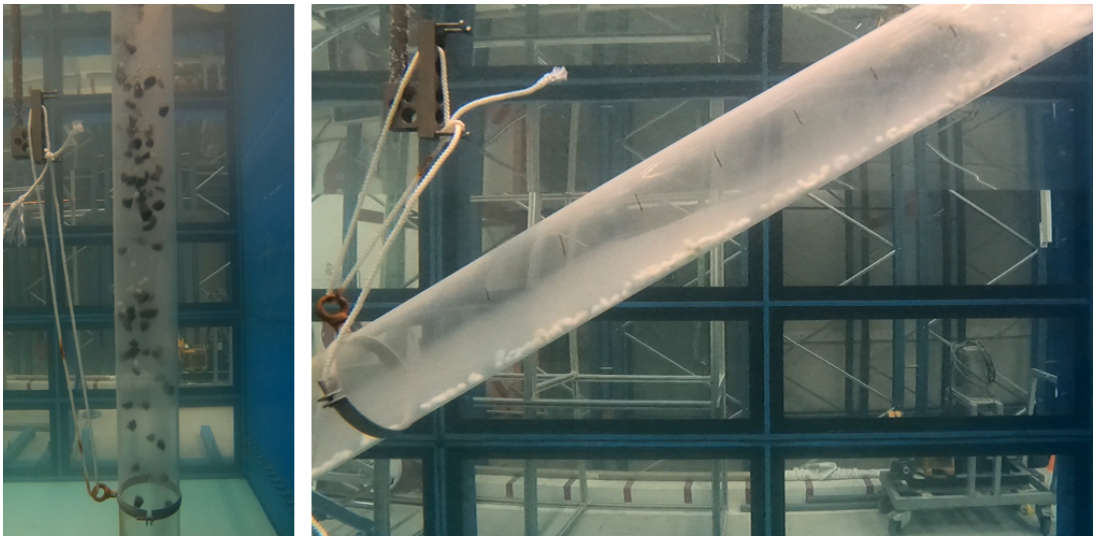

Figure 7.5: The pipe at 90^o and at 30^o

7.3.2 Step-by-step plan for the tests

This is a step-by-step plan covering all steps necessary to successfully carry out the model tests. Before starting any tests, determine the velocity of the conveyor belt and wash all rocks to reduce dust in the water.

Preparation

1. Set the angle of the pipe.
2. Place the bucket below the pipe.
3. Weigh the amount of rocks needed for the test.
4. Write down test number and parameters on a flash card (angle, production, rock size).
5. Lay the rocks over a predefined distance on the conveyor belt.

Tests

1. Start the cameras.
2. Film the flash card.
3. Start the conveyor belt.
4. Stop the conveyor belt.
5. Stop the cameras.
6. Save the results.
7. Wait for the dust from the rocks to settle down.

Velocity calculation in PIVlab

1. Rotate the videos with a video editor to set the pipes vertical or horizontal.
2. Set up a batch for analysis in PIVlab with appropriate settings.
3. Run PIV analysis.
4. Export velocities from points at the start, the middle and the end of the region of interest of the pipe, and over the length of the pipe to MATLAB.
5. Plot velocity profiles of the flow through pipe cross-sections.

Velocity calculation with a video player

1. Open a video in a video player of choice (VLC or PotPlayer for example because they have a frame-by-frame function).
2. Count the frames it takes for a cluster of stones to go between two points in the pipe.
3. Calculate the velocity.
4. Repeat multiple times per test.
5. Take the average of the velocities.

Measuring offset and spread with a video player

1. Take a screenshot of during playback of a video of the area below the pipe.
2. Open the still in the MATLAB Image Viewer.
3. Use the 'measure distance' tool to measure the offset and spread of the rock flow below the pipe.
4. Convert the measured pixel distances to SI units.

Measuring offset and spread at 25 cm below the pipe

1. Take a screenshot of during playback of a video of the area below the pipe.
2. Open the still in the MATLAB Image Viewer.
3. Use the 'measure distance' tool to measure 25 cm below the pipe.
4. Use the 'measure distance' tool to measure the offset and spread of the rock flow below the pipe.
5. Convert the measured pixel distances to SI units.

On the next page, figure 7.6 shows the where the velocities are measured, and figure 7.7 shows where the offsets, spreads and velocities are measured below the pipe.

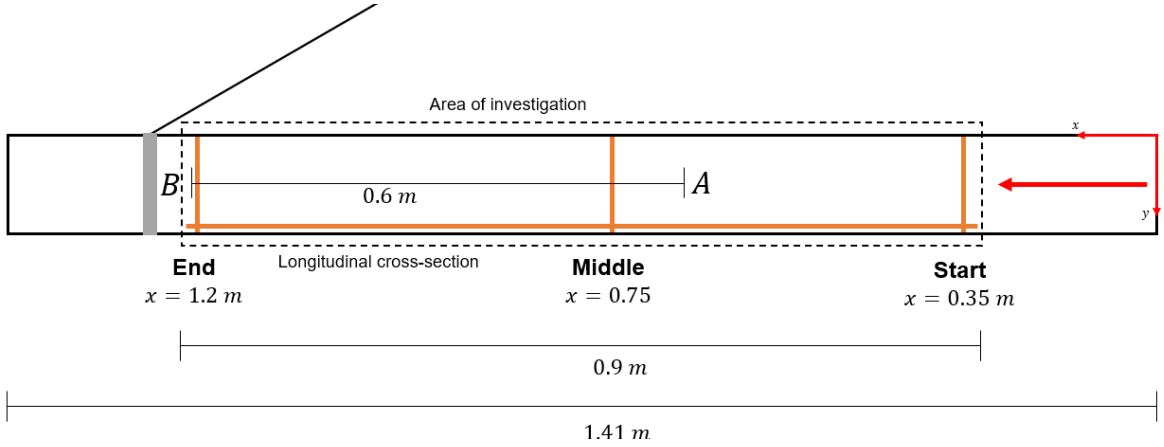

Figure 7.6: The locations where velocities are measured. The orange lines indicate the profiles made with PIVlab, A & B are the points between which the velocity is manually calculated.

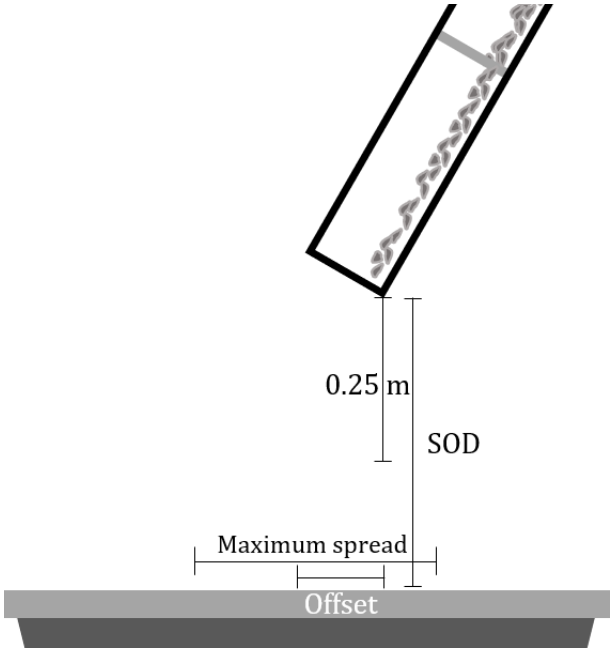

Figure 7.7: The locations where the spread and offset are measured. The stand-off distance (SOD) to the floor varies with the angle of the pipe. The offset and spread are also measured at 25 cm below the pipe. The velocity is measured over the SOD.

Chapter 8

Results of the mixture process in the pipe section

8.1 Introduction

This chapter details the results recorded in the pipe of the experiments in the dredging lab. Section 8.2 qualitatively outlines processes observed in the pipe. Section 8.3 describes the results from the manual calculations of the pipe velocity and the influence changing the angle, rock size and production has on flow in the pipe, and the results gathered with PIVlab. It also shows a comparison of the two methods. Section 8.4 talks about the scale effects in the tests, and finally section 8.5 concludes and summarizes.

8.2 Observed processes

In the laboratory, 91 tests have been carried out with a broad composition of parameters (see also section 7.3.1 and appendix A). The changes in parameters between the tests are meant to show the different ways flow can develop in an inclined pipe. Figure 8.1 for example, shows that the rock flow at steep angles does not form a smooth sliding bed but that the bed starts to break up. The rocks cannot form a smooth bed due to return

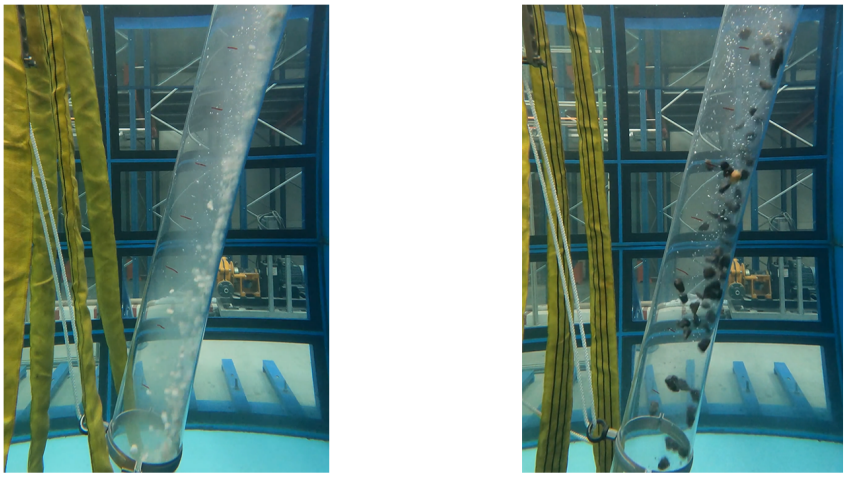

Figure 8.1: Two tests (4 & 10) at the same angle and production but with different rock sizes that show the bed breaking up halfway in the pipe.

flow and vortexes created by the flow. Some rocks move upwards and tumble around in

the pipe before either settling down in the left side of the pipe or joining the flow again at the right side. This is an effect that mostly happens at 75° and 60° because it is closer to free fall. At lower angles the bed experiences more shear with the upper layer that 'catches' rocks and deposits them back in the flow. These effects and vortexes seem to be caused by a return flow and the subsequent velocity difference. The bed moves quickly down through the pipe, and the upper layer moves up through the pipe or is stationary. The return flow is caused by the rock flow entraining water from the upper layer of the pipe and pushing water away in the lower layer of the pipe. The water removed from the upper layer needs to be compensated, and this happens with the return flow. Depending on the angle of the pipe, the flow in the pipe can be true two-layer flow, partial two-layer flow with some particles in suspension, or suspended particle transport.

Another example of an effect that happens in an inclined pipe is the formation of groups and slipstreams. Figure 8.2 shows a clear example of this. The rocks clump together because of the water resistance against the front of the group and the increased group mass causes the group to accelerate. At some point, some rocks at the back of the group start to lag behind and lose the slipstream effect of the group. These rocks start to decelerate until enough rocks have clumped together to form a new group that starts to accelerate. This slipstream effect happens at all angles but is more pronounced at 45° and 30°, and for the 12-16 mm and 16-32 mm rocks. The rocks are placed in an even bed on the conveyor belt and the conveyor belt runs with the same speed for all tests, making this effect a consequence of the flow in the pipe and not the feed conditions.

Table 8.1 gives an overview of the effects observed in the pipe for each parameter composition, indicating if the flow resembles two-layer flow, suspended flow, if clusters form, etc.

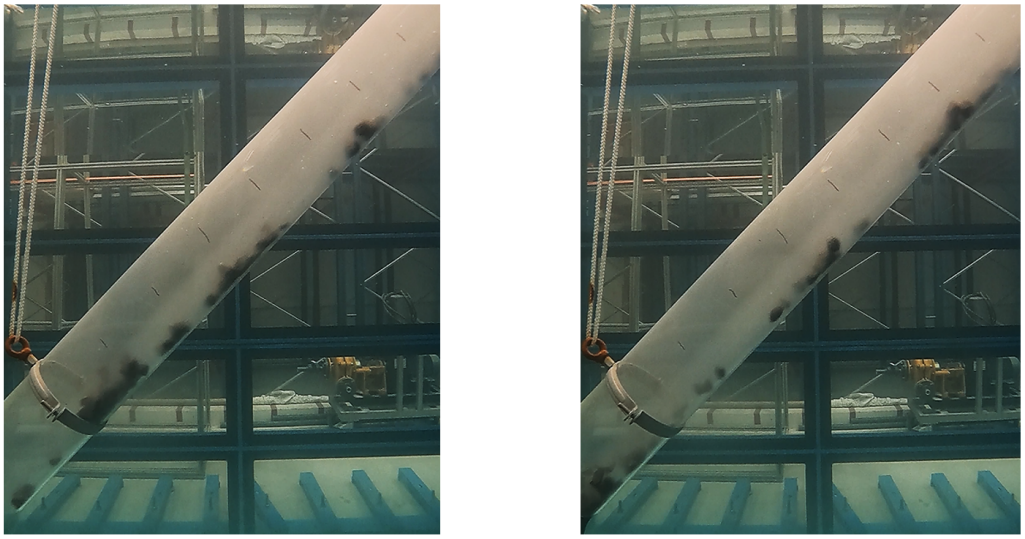

Figure 8.2: Two frames from test 38 with 20 frames between them that show the effect of slipstreams in the pipe.

Table 8.1: A summary of the observed effects in the pipe.

Observation levels	
A	Two-layer flow
B	Two-layer flow - particles in suspension
C	Rock clusters
D	Some chaos observed; partial bottom transport, partial suspended transport
E	Total chaos, like a vertical pipe

Production:	0.16	kg/s			
Angle	*90°*	*75°*	*60°*	*45°*	*30°*
8-12 mm	E	B, C	A, C	A, C	A, C
12-16 mm	E	C, D	A,C	A, C	A, C
16-32 mm	E	D/E	B	A, C	A, C

Production:	0.32	kg/s			
Angle	*90°*	*75°*	*60°*	*45°*	*30°*
8-12 mm	E	B, C	B, C	A, C	A, C
12-16 mm	E	C, D	A, C	A, C	A, C
16-32 mm	E	D/E	B	B, C	A, C

Production:	0.48	kg/s			
Angle	*90°*	*75°*	*60°*	*45°*	*30°*
8-12 mm	E	C, D	B, C	A, C	A
12-16 mm	E	C, D	A, C	A, C	A, C
8-16 mm	E	C, D	A, C	A, C	A, C

Production:	0.64	kg/s			
Angle	*90°*	*75°*	*60°*	*45°*	*30°*
8-12 mm	E	D	B, C	A, C	A
12-16 mm	E	C, D	A, C	A, C	A, C

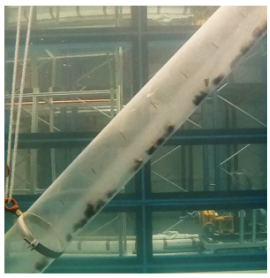

A - Two-layer flow.
C – Rock clusters.

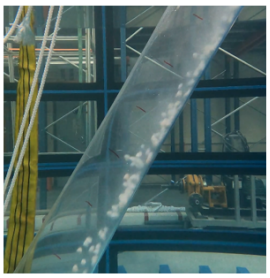

B - Two-layer flow, particles in suspension.

D – Some chaos observed.

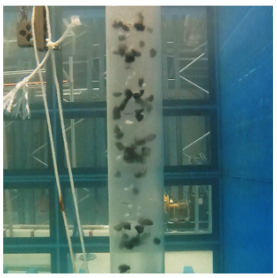

E – Total chaos, vertical pipe.

Figure 8.3: The observed effects of table 8.1

8.3 Velocity of the rocks

8.3.1 Manual analysis

After observing the processes in the pipe and the qualitative analysis, the behavior in the pipe can be analyzed more quantitatively. The rock flow in the pipe is analyzed for their average velocity. The simplest method for doing that is measuring the time it takes for a stone or a cluster of stones to cover a certain distance. The pipe is covered with tick marks with a distance of 10 cm between them and the footage of the experiments is shot in sixty frames per second. Thus simply counting the frames it takes to cover the distance between mark A and mark B is enough to calculate the average velocity. Figure 8.4 shows test 36 with the pipe at 45°, 12-16 mm rocks and 0.48 kg/s production. The distance between mark A and B is 0.5 m and the difference between the snapshots is 50 frames. This was the time it took for the cluster at A in the left image to travel to B in the right image. Point B is always taken as the last mark before the brace holding the pipe, and point A is either 0.6 or 0.5 m before that, depending on the pipe angle and camera position relative to the pipe.

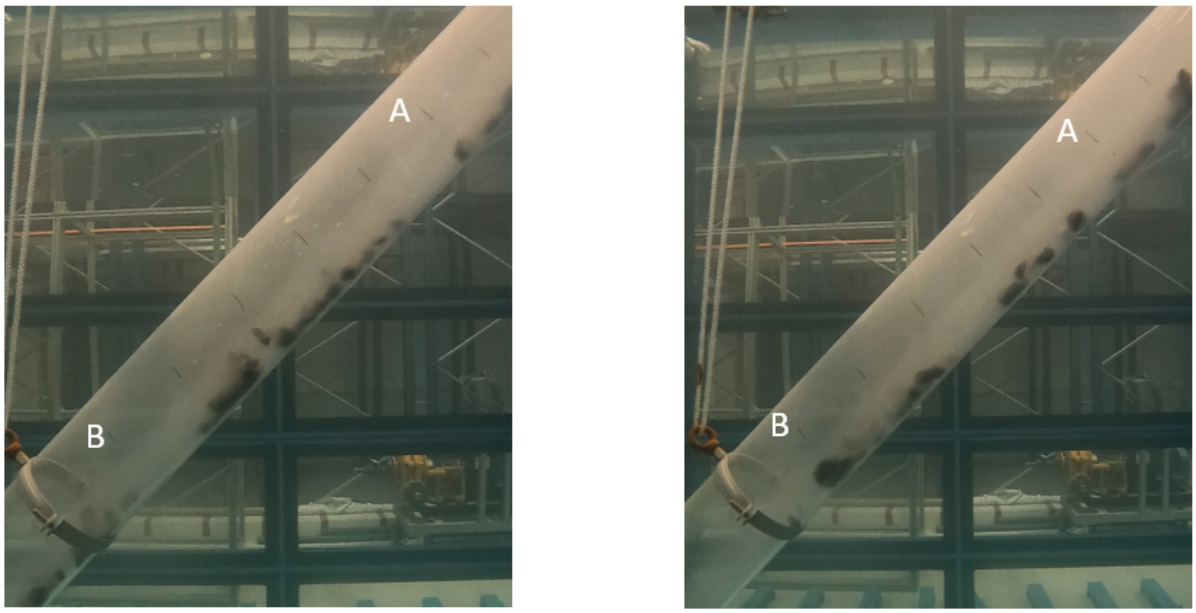

Figure 8.4: Two frames, with a difference of 50 frames.

Calculating the velocity from this is done with

$$w = \frac{s}{\left(\frac{\text{frames}}{\text{frames per second}}\right)} = \frac{0.5}{\left(\frac{50}{60}\right)} = 0.6\, m/s \tag{8.1}$$

To average out turbulence in the pipe that can change the flow velocity, changes in visibility that impact the calculation, or mistakes, the velocity is calculated at least six times per test. The average per test is shown in figure 8.5 (next page). On the left the results are colored per rock size and on the right per production.

It is immediately clear that the angle has a large influence on the average velocity of the rock flow. At 75° the average velocity ranges from 0.67 m/s to 0.88 m/s, and at 30° the average rock velocity is between 0.45 m/s and 0.65 m/s. The closer the angle of the pipe is to vertical, the faster the rocks go. The exception however is the flow in the vertical pipe (90°). At that angle, the velocity is in the same range as at 30°, between 0.46 and 0.65 m/s. The rocks in the vertical pipe experience the effects of hindered settling and

the wall effect (see chapter 3), slowing down the rocks. In reality, sometimes water is added at the top in a vertical pipe to counter drop of the water level.

Because figure 8.5 is plotted with velocity against the angle and a lot of results are covering each other, it is difficult to discern the effects of the rock grading and production on the velocity. In figure 8.6, the velocities are plotted against the rock size and the production, with linear trend lines through the data. The trend seems to be that for increasing rock size, the velocity decreases, but a caveat for this figure is that the largest rocks have not been tested with the highest productions. Figure 8.7 shows on the left the rock velocity for all productions at 8-12 mm, 8-16 mm and 12-16 mm, and on the right all the rock sizes at 0.16 kg/s and 0.32 kg/s. This shows that for the 8-12 mm and the 12-16 mm rock and the 8-16 mm mixture the rock size has minimal influence on the rock velocity, but on average gives a slight decrease. The plot on the right, at 0.16 kg/s and 0.32 kg/s, shows a downward trend for the velocity when the largest rock grading is taken into account, except for the vertical pipe, where velocity increases with particle size. The smaller rocks have a higher particle count per unit of time, and the rocks together form a more compact bed that has a smaller projected surface area, and thus less resistance. Figure 8.8 illustrates this effect with a comparison between three tests, all at 75° and 0.32 kg/s.

The plot on the right in figure 8.6 shows the influence of production on the velocity of the rock flow. For all angles, except for 90°, there is an increase in velocity with increased production. Figure 8.9 has separated the data from figure 8.6 in three plots to make it more clear. At 90°, the velocity does not increase with the production, but decreases with larger productions, with an optimum between 0.32 and 0.48 kg/s. The velocity increases for increasing productions because the mass of the bed is higher. Gravity is the driving force in the inclined fall pipe, so it follows that a higher mass of the bed gives a higher velocity.

It was tried to perform statistical analysis on the results but because there were either no or one repeat per test configuration, there is not enough data to determine the mean and standard deviation per parameter set.

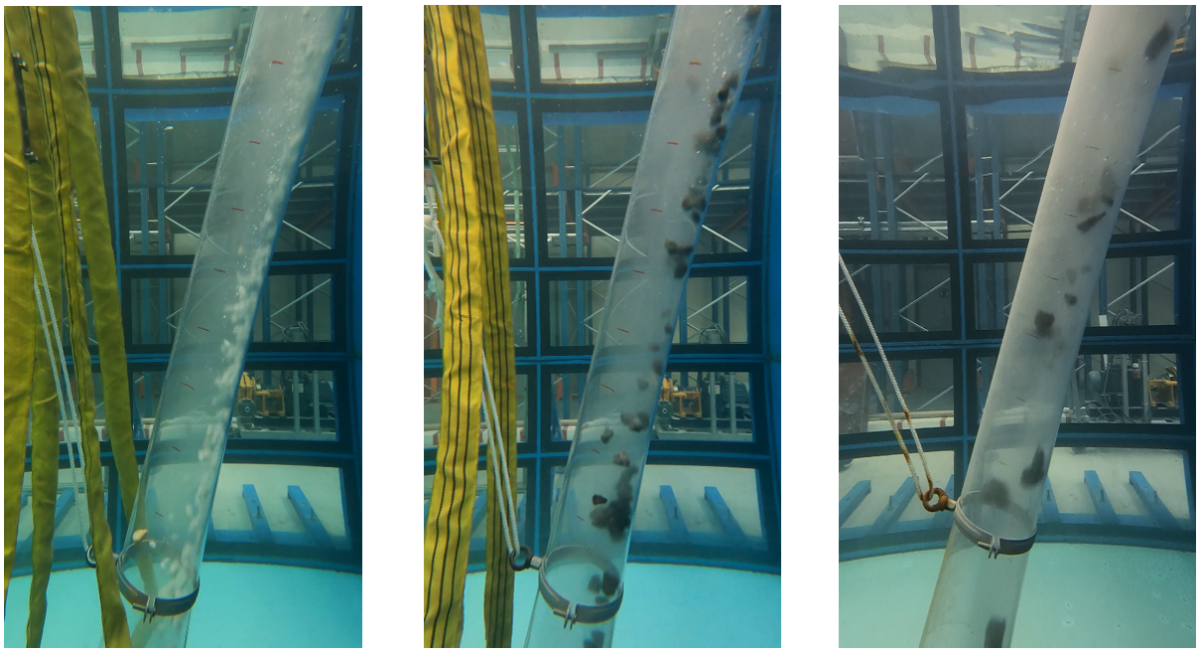

Figure 8.8: Stills from three tests (7, 13 and 76) at 75° and 0.32 kg/s production, but with different rock sizes.

Single particle velocity

Some tests were carried out with individual particles, namely with spherical marbles and rocks, as a way to compare the theory from chapter 3 to the test situation. Figure 8.10 shows the measured velocities and the calculated velocities in the pipe at 75°, with the rock particulars in table 8.2 below. An interesting situation occurs here as the larger rocks are faster alone than in a group, but the smaller stones are a lot faster in groups than individually. The interaction of the large rocks hinder the flow in the pipe, slowing

down the other rocks. The small rocks benefit from the group effect identified in section 8.2. The figure also shows velocities marked with $w\theta$ and $vt\theta$. These are velocities calculated with equations 3.15, 3.18 and 3.19 from section 3.3.4. The calculated velocities are much higher than than the measured velocities, even for a sphere. Comparing the test results to the research done into small spheres and thin tubes shows that the results at smaller scale and particle/pipe ratio's are not applicable to irregular particles in large pipes.

Table 8.2: Rock particulars from figure 8.10.

Rock weight	*Nominal diameter*	*Density*
62.3 g	28 mm	2900 kg/m^3
44.3 g	25 mm	2900 kg/m^3
16.4 g	18 mm	2900 kg/m^3
14 g	17 mm	2670 kg/m^3
9.6 g	15 mm	2670 kg/m^3
5.8 g	13 mm	2670 kg/m^3
2.5 g	10 mm	2711 kg/m^3
1.7 g	9 mm	2711 kg/m^3
0.8	7 mm	2711 kg/m^3
3.5 g (marble)	14 mm	2500 kg/m^3

8.3.2 Analysis with PIVlab

PIVlab is used to determine the velocity of the flow at any point in a region in the pipe. With this, not just the velocity can be determined, but also the way the velocity and the flow develops over the length of the pipe. PIVlab can be a powerful tool for analysis but there are some caveats for using it. First, the amount of particles must be large enough, and the particle sizes preferably small enough, so the flow is accurately defined by the particles. Second, the direction of the flow must be vertical or horizontal to align with the grid PIVlab utilizes. Third, there needs to be contrast between the particles, otherwise the difference between two frames cannot be detected by the software. These points mean that not all experiments carried out were usable for analysis in PIVlab. The experiments with the 16-32 mm rocks have too few particles to analyze this way for example and in some tests with the white 8-12 mm rocks the lighting makes the contrast minimal. The problem with the direction of the flow is remedied by rotating the images to align with the horizontal and vertical axis.

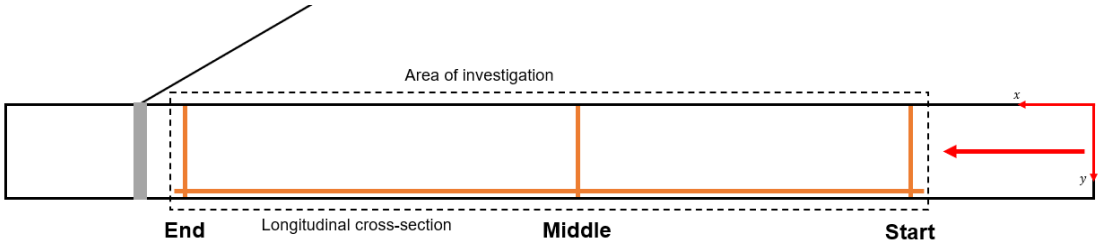

Figure 8.11: Sketch of the pipe region analyzed with PIV.

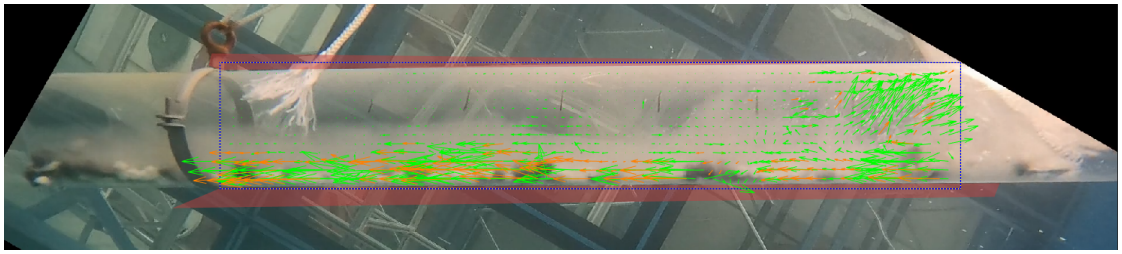

Figure 8.12: Frame from test 54 at 30°, 8-16 mm and 0.48 kg/s.

Figure 8.11 shows the region of the pipe analyzed with PIVlab, and the locations where velocity profiles are plotted. Figures 8.12 and 8.13 show a PIV example from test 54. Figure 8.12 shows one frame of 180 used for analysis. The green vectors are velocity vectors determined by PIVlab and the orange vectors are outliers that have been replaced by interpolated vectors based on neighboring grid points. Vectors are removed if they either exceed the mean velocity plus eight times the standard deviation or if they deviate three times from the local median. These filtering methods are simple to implement and based on experience from the developer of PIVlab (Thielicke, 2014). The vectors are distanced 15 pixels because the interrogation area used by the multipass algorithm changes from 120 to 60 to 30 pixels with 50% overlap.

Figure 8.13 shows three compounded velocity profiles over the width of the pipe. Each gray line is the velocity profile of one frame from the video and the red line is the average of all frames. The velocity profile for test 54 shows a top speed of 0.8 m/s near the bottom of the pipe, but shows also that the velocity can be zero at that location. This is a consequence of the cluster formation in the pipe and the way PIVlab calculates the velocity at all points for every frame, even if there are no particles visible at that point. This figure can therefore be used to see the general top speed at a point in the pipe and

the layer thickness, because for the points where there are no particles, no velocity is calculated. This explains why the lines cover so much space between 0 and the max, and why the average is so low.

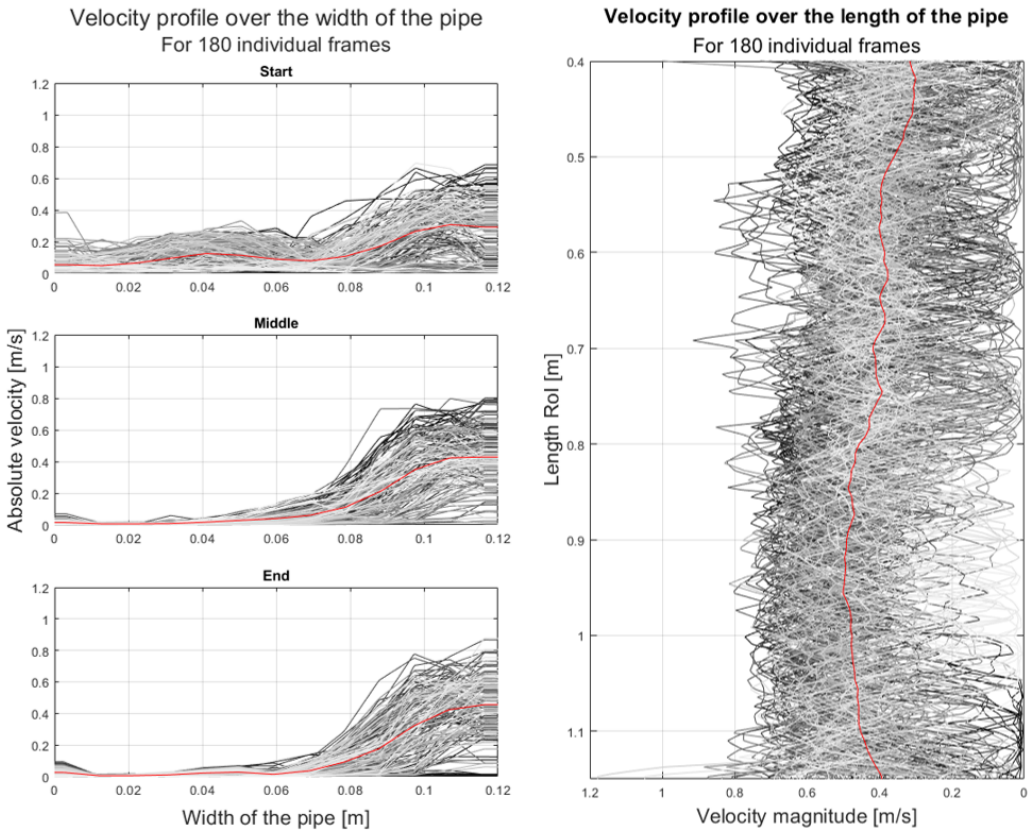

Figure 8.13: Left: absolute velocity profiles over the width of the pipe at the start, middle and end. Note: the 0 on the x-axis is the top of the pipe, and the end, 0.12 is the bottom of the pipe where the rocks are. Right: absolute velocity profile over the length of the pipe. The red line is the average absolute velocity.

The 'start' plot of figure 8.13 shows velocities at the line marked 'start' in figure 8.11. It even shows velocity in the top half of the pipe, even if no rocks flow there, because PIVlab sees the entrained air bubbles that move in the opposite direction of rocks, but because the velocity is calculated as absolute velocity, it shows up in the figure as positive velocity. Because the most important part of the PIV is the velocity at the bottom, it is deemed acceptable that these aberrations show up in some plots. Some rocks move backwards due to vortexes, but the velocity in negative x-direction is small in these cases, and does not exceed the top speed marked in the figures. The velocities in y-direction are also very small, because the rocks mostly go with the flow direction through the pipe. Therefore the top speed from the absolute velocity is virtually the same as the top speed in x-direction.

The right plot in figure 8.13 shows the same kind of plot as the plots on the left, but over the length of the pipe, 2 cm from the bottom. Two centimeters from the bottom is approximately where the peak velocity is in the horizontal velocity plots. The top of the figure corresponds to the start of the area of investigation. This plot is useful for determining the top speed at a location in the pipe, and seeing how the velocity develops over the length of the pipe. In the case of run 54, the absolute velocity increases from roughly 0.6 m/s to 0.75 m/s, where it plateaus and starts to decline again near the end of the region investigated with PIV.

Because of the limits imposed by equipment size and scale factors, the pipe used for the tests has the shortest length possible for pipe on the Rockpiper, and the usable region for PIV is shorter than the length of the pipe. Therefore it is difficult to determine how the flow develops over longer distances. The flow might slow down and then stay constant, or the flow velocity might increase again in some sort of cyclic behavior. In most of the tests analyzed with PIVlab, the velocity develops in the same way, where the velocity increases in the first part of the pipe, and plateaus halfway through the area of investigation. This seems to suggest that the length of the pipe is long enough for a stationary situation. For a comprehensive overview of these tests, see appendix C.

Some interesting examples that show the value of PIV software to visualize the velocity at all points in the pipe, are the tests in the vertical fall-pipe. The velocity profiles over the width of the pipe start skewed to the left side due to the inclined hopper feeding the pipe. Towards the end of the pipe, the velocity profiles become (more) symmetrical and the velocity decreases. Figure 8.14 shows this for two tests with 0.48 kg/s production and 8-16 mm and 8-12 mm rocks respectively. The top velocity in the profiles marked with End is lower for both tests than the velocity at Start and Middle. The longitudinal velocity profiles from figure 8.15 show this as well. The rocks accelerate until halfway through the pipe and then they start to decelerate again. The rock flow in the vertical pipe experiences similar effects as inclined pipes due to vortexes and return flow.

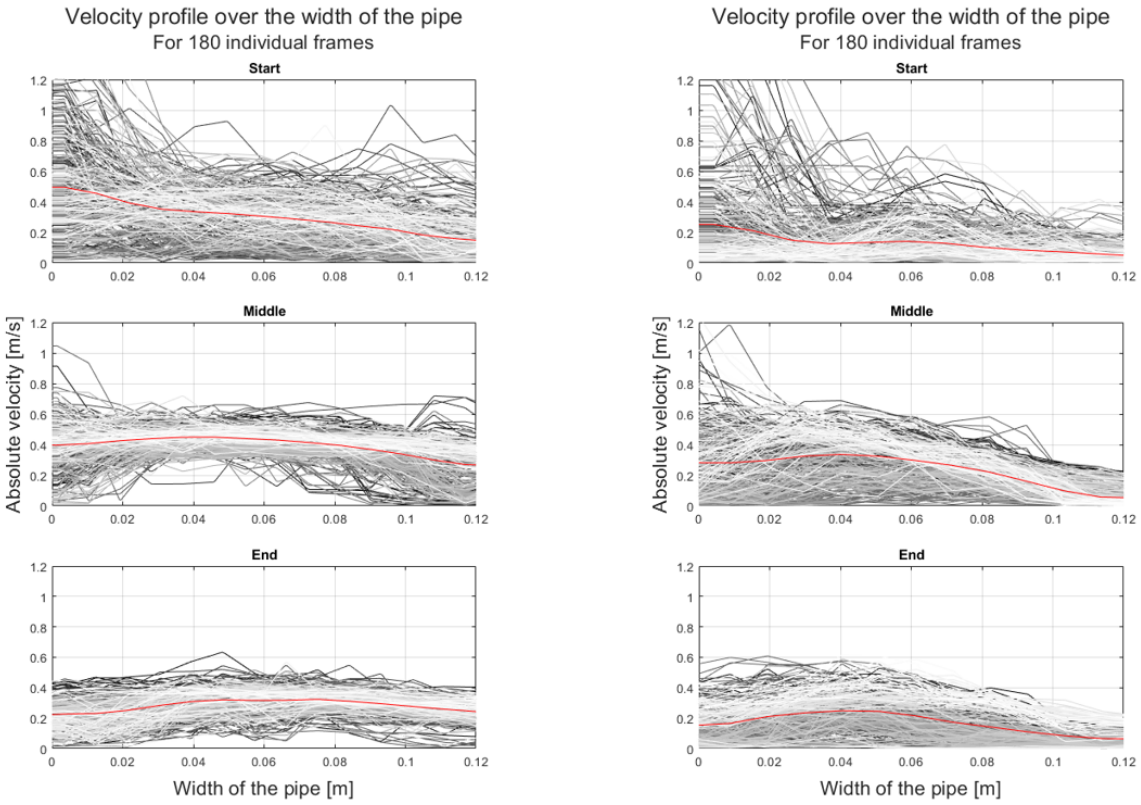

Figure 8.14: Horizontal absolute velocity profiles of tests 61 and 56 showing the velocity symmetry in the pipe. Both tests at 90°, 0.48 kg/s, and 8-16 mm and 8-12 mm rocks.

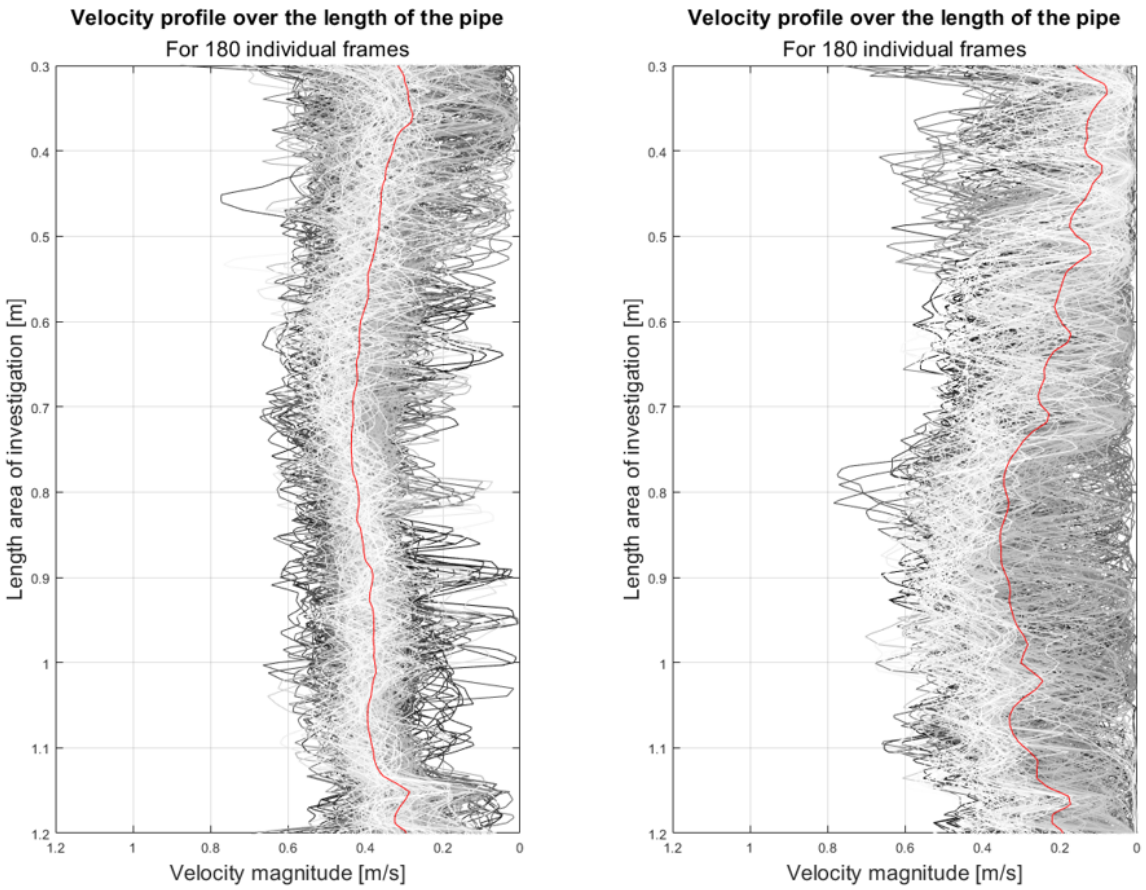

Figure 8.15: Longitudinal absolute velocity profiles of tests 61 and 56 showing the velocity development in the pipe. Both tests at 90°, 0.48 kg/s, and 8-16 mm and 8-12 mm rocks.

Downsides of PIV

During analysis of the tests it became clear that the raw videos were not suitable for PIV without some alterations, i.e. rotation of the image. The process also turned out to be very labor intensive in comparison to the manual calculations, both in preparation and in run time of the software. Finally, not all tests were able to produce valid or useful results. Due to background interference, lack of contrast in the rocks and low particle count, PIVlab did not produce results that described accurately what happened in the pipe. An example of this is test 8, as illustrated in figure 8.16. Parts of the longitudinal velocity profile show the expected flow development, but the flow velocity is very small at two points. When reviewing the test video, the rocks did not decelerate and accelerate drastically, so there had to be another cause. At the red arrow, PIVlab could not distinguish the rocks from the background and interpolated the velocity based on the surrounding values.

Because of examples like this, PIVlab is not the most reliable tool for fall-pipe analysis as it depends greatly on the quality of the data. To make PIV better suitable and more reliable for fall-pipe analysis, a few steps can be taken. First, make the videos better suitable. Use a plain background, use a rock mixture of contrasting colors or paint part of the rocks, and illuminate the pipe. Second, make or animate a test case with known motions and velocities with similar parameters as the tests to calibrate the PIV software. Finally, productions must be large enough to ensure enough particles are in the pipe for the PIV software to correlate the motions between grid points.

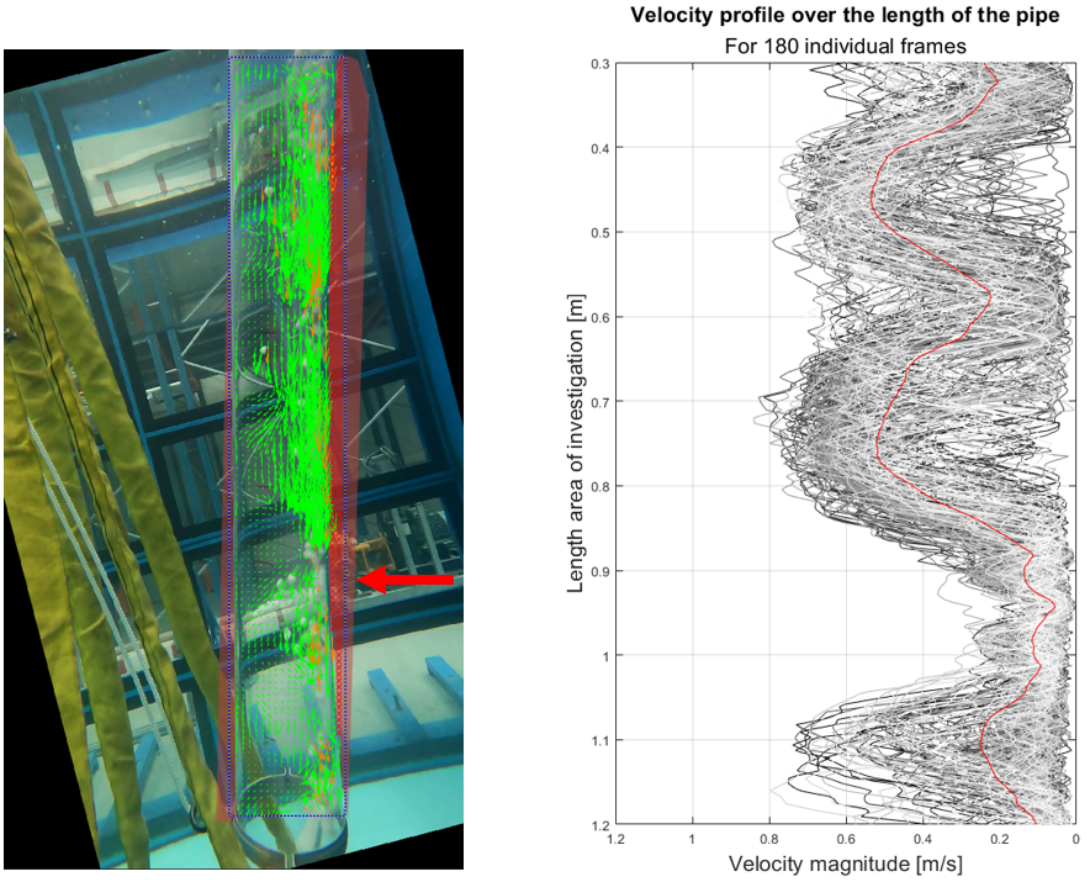

Figure 8.16: PIVlab analysis of test 8 (75°, 0.16 kg/s, 8-12 mm) with the corresponding longitudinal velocity profile.

8.3.3 Comparison of manual calculations and PIVlab

PIV and the manual calculations are two ways of looking at the flow in the pipe, and both offer advantages and disadvantages. PIVlab gives a great detailed view of the rock velocity at any point in the pipe, but is very labor intensive to set up and, if set up wrong gives no or very inaccurate results. The manual calculations are very easy to carry out and can be easily used to show trends in the variation of parameters, but it ignores effects in the pipe that locally accelerate or decelerate the rocks. The values from the two methods also differ somewhat. Figure 8.17 shows the velocities calculated at the three points in the pipe compared to the average velocities calculated manually. The blue and gray dots compare the average peak velocities calculated at the start and end of the area of investigation to the manually calculated average velocities. The peak velocity calculated with PIV is higher for the high velocities, and lower for the low velocities, but the average is approximately equal to the manual velocities, because the slope of the trend line is nearly 1. The velocity calculated in the middle of the pipe with PIV is on average slightly higher than the average of the manually calculated velocities. This corresponds to the trend shown in figures 8.14 and 8.15, where the velocity increases towards the middle of the pipe, and then decreases towards the end.

The fact that manual calculations and PIV on average give similar results proves that both methods used together are a great tool of analysis that can give deeper insights in the flow behavior in a pipe, if set up correctly.

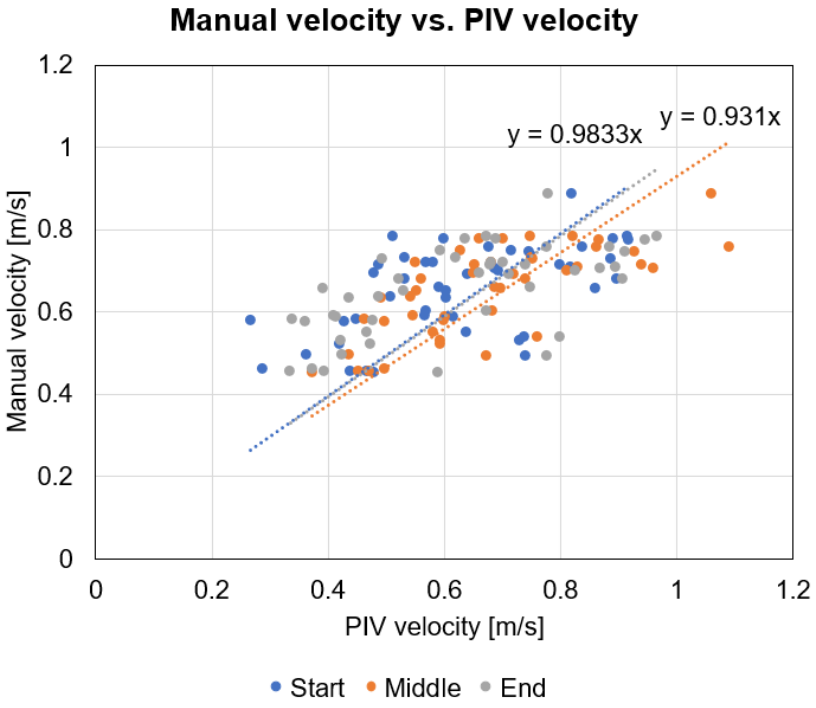

Figure 8.17: Comparison of the peak average of the PIV analysis at three points in the pipe and the manual velocity calculations.

8.4 Scale effects

Scale effects arise from the impossibility of keeping the ratio between model and prototype Froude and Reynolds numbers both at 1. The viscosity of the medium in which the tests are carried out is impossible to change with the amount needed from the scaling factor ($\alpha = 15, \alpha_\nu = 15^{1.5}$). Effectively this means that the tests were carried out in a liquid relatively more viscous compared to reality because the liquid is the same at model scale and in reality. The Reynolds number is $\sim$60 times higher in reality than for the model scale. If the drag coefficient of the rocks behaves the same as for a sphere, like in the left plot in figure 8.18, than the drag coefficient is lower in reality than at model scale and the rocks will go faster than the scaling predicts (velocity scales with a factor of $\sqrt{15}$). The drag coefficient of a sphere is approximately 0.5 at the Reynolds numbers of the tests, and for the rocks at approximately 1.2. The Reynolds numbers at prototype scale for the spheres are greater than $3{\cdot}10^5$, where the drag coefficient is approximately 0.1. The question is if that happens for rocks as well.

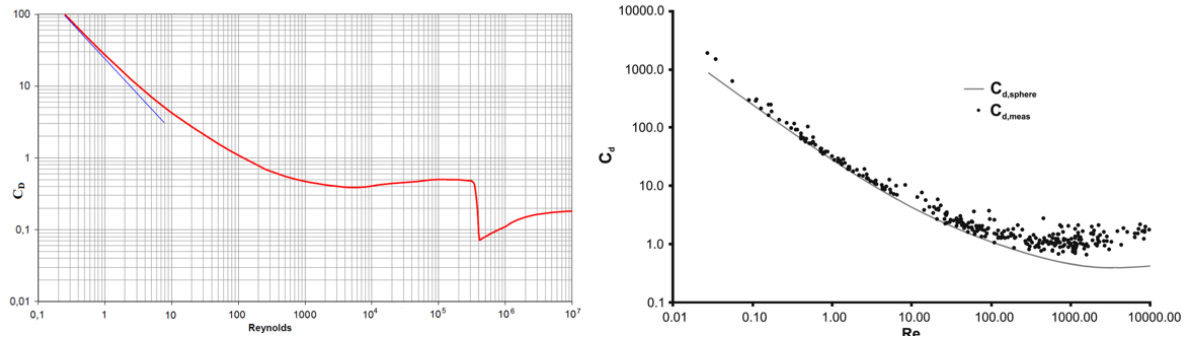

Figure 8.18: Drag coefficient of a sphere (Go Mars, B. de, 2014) and the measured drag coefficient of rock particles and of a sphere (Dioguardi et al., 2018).

A second factor to consider in scaling between the tests and reality stems from the pipe material and roughness and the resulting friction factor. The pipe in the tests setup is PMMA and very smooth ($\mu_{sf} =$), and was barely scratched from tests. The pipe on the Rockpiper is steel ($\mu_{sf} = 0.5$), which is inherently rougher than plastic, and the size and velocity of the rocks damages the pipe. This both leads to more friction between the pipe and the rock flow, potentially slowing down the rock flow.

8.5 Conclusions

Chapter 9

Results of the processes in the area below the pipe

9.1 Introduction

This chapter explains the results from the laboratory tests from the area below the pipe. Section 9.2 explores the processes observed, section 9.3 starts on the method used for analysis and a select few tests used to calibrate the analysis of the bulk of the tests. These tests are treated in section 9.4. Section 9.5 summarizes and concludes the results.

9.2 Observed processes

For the 91 tests, not only the processes in the pipe were observed, but also the area between the pipe and the bed. The first thing that immediately stands out is the cone shape created by the falling rocks. This shape is expected from the single stone model described in section 4.3.3. The cone is not located immediately below the pipe, but a small distance away. The rocks fall some distance away from the pipe due to the horizontal velocity the rocks get from the pipe inclination. This is described by the offset model from section 4.3.4, with the major difference that the horizontal velocity is not constant over the fall height, but decreases the moment the rocks leave the pipe. The rocks therefore stop falling forwards after some distance and continue falling only downwards.

Figure 9.1: The cone shape of the rock mass (test 18).

Section 8.2 describes the group formation in the rock flow and these groups persist also after the pipe, making the falling process intermittent instead of continuous. Figure 9.2 shows the progress of one group falling out of the pipe. This group then follows the phases described in 4.4.2, where the group first accelerates, then the acceleration stops and the group breaks up, and then the rocks fall barely influencing each other. The fifth phase, radial runoff, cannot exist in this setup because the rocks fall through the grate in the bucket. Because the height of the floor is fixed, smaller angles of the pipe increase the distance between the pipe and the grate. The larger distance makes the group effect and the distinction between the falling phases more pronounced.

Figure 9.2: A series of images from test 30 (45°, 0.48 kg/s and 8-12 mm, SOD = 0.67 m) showing the falling phases in the rocks below the pipe.

9.3 Tests with small containers

The general method of analyzing the spread of the tests consists of simply measuring the spread of the rocks and the offset from the pipe. Figure 9.3 (next page) shows a sketch of the method with an example next to it. The blue lines indicate the offset. The offset is the distance between the lowest corner of the pipe and where the center of mass of the rocks reaches the floor. The green lines indicate the maximum spread of the rocks, measured from the offset. The red lines indicate where the bulk of the rocks come down, approximately 80%. These distances are not just measured from one still frame, but are measured in the video of the full tests. The image viewer from MATLAB allows you to measure the pixel distance between two points and this can be converted to SI units.

Just measuring an image of a rock cone is error prone and depends on the observer and their definition of 'the bulk of the rocks' for the measurements, and from the images is it only possible to determine the spread in one direction. To make the method more defined, a setup was devised with small containers to measure the spread of the rocks in two directions and determine accurately where the rocks come down. Four tests have been carried out with the setup shown in figure 9.4 (next page), at two different angles: 60° and 45° and two rock sizes: 8-12 mm and 12-16 mm. These tests were carried out with a production of 0.32 kg/s.

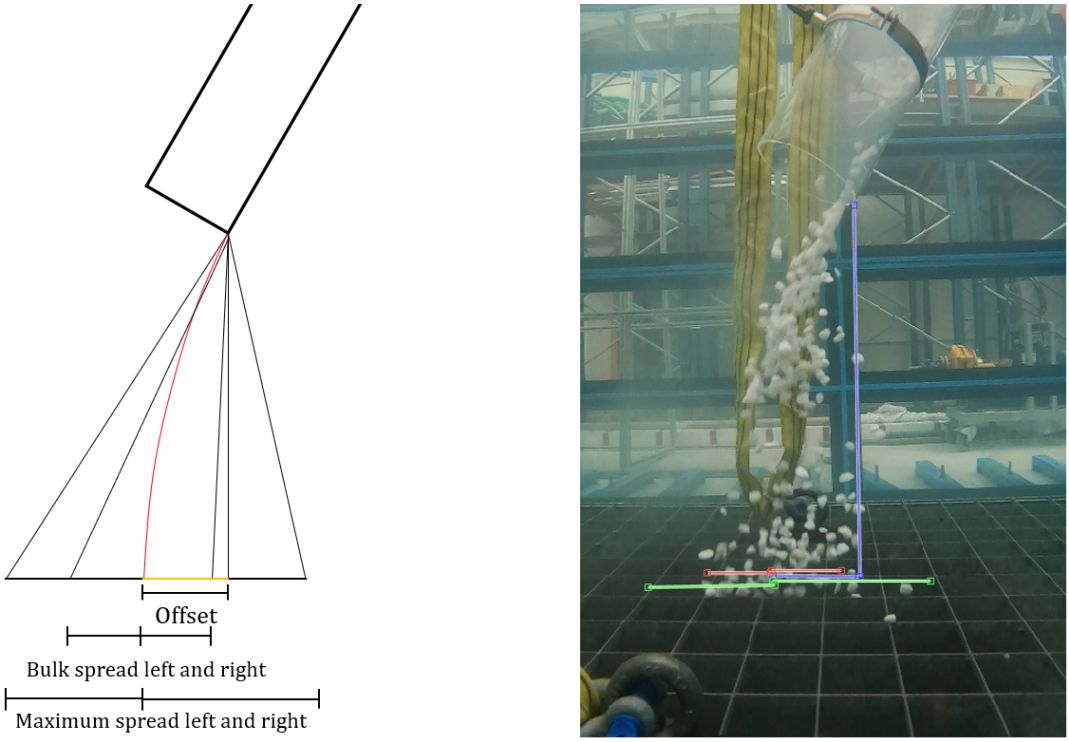

Figure 9.3: A sketch and an example of the method of rock spread analysis.

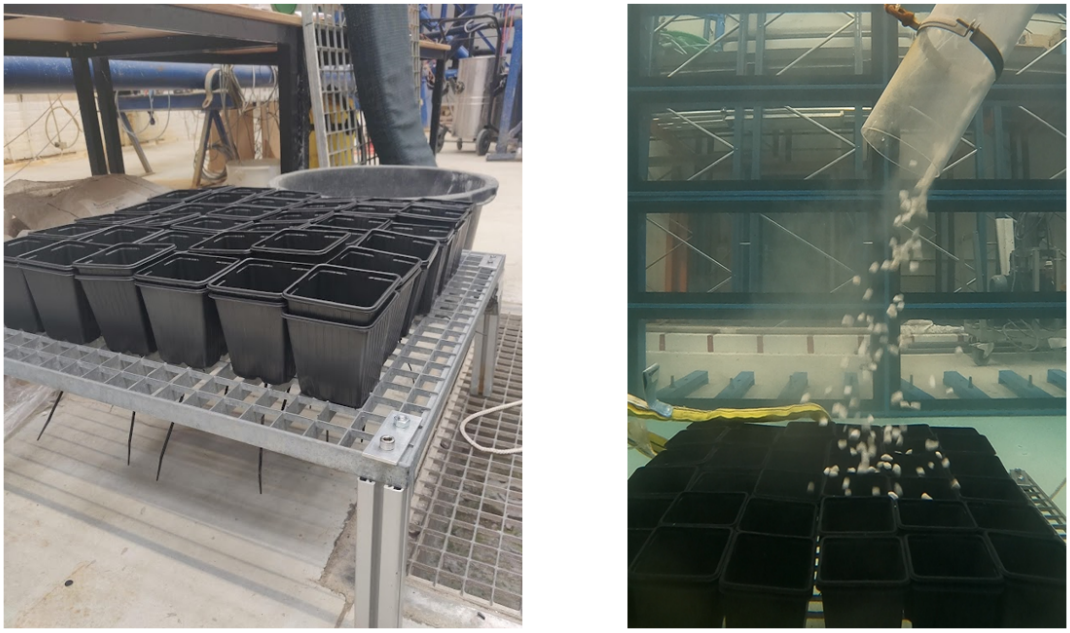

Figure 9.4: The container setup out of the tank and the container setup during a test.

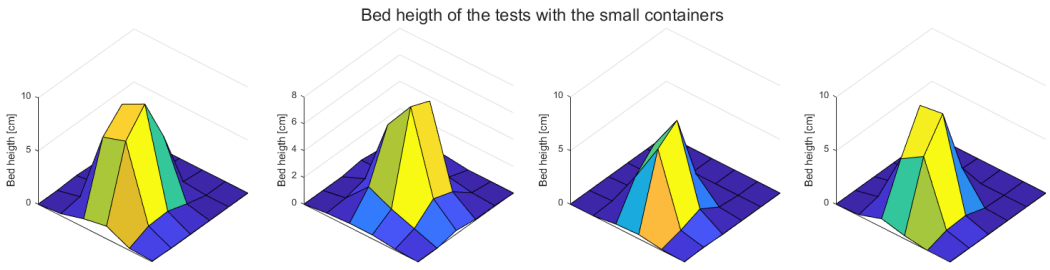

Figure 9.6: A 3D visualization of the bed height of the small containers.

9.4 Test results

Using the knowledge gained from the container tests, the other tests can be analyzed for their variation in offset, the maximum spread and the bulk spread. The velocities of the rocks after the pipe can be compared to the velocities in the pipe. These results were gathered with the method outlined in section 9.3, and the velocity is calculated the same way as in section 8.3.1.

Figure 9.7 shows the maximum spread and the bulk spread for the tests for each angle. It becomes immediately clear that the spread increases when the pipe angle decreases. The floor of the tank is fixed and the stand-off distance (SOD) between the pipe and the grate increases when the pipe angle decreases (see table 9.1). It should be noted that no results have been recorded for the tests with the pipe at 30° because the FOV of the camera was too tight and the region of interest could not be captured in full.

Angle	Stand-off distance	Angle	Stand-off distance
90°	0.21 m	45°	0.67 m
75°	0.25 m	30°	0.96 m
60°	0.44 m		

Table 9.1: Stand-off distance per angle.

Figure 9.7 clearly shows the influence of the angle and SOD on the spread of the rocks, but is not clear on the influence of the production and the rock size on the spread of the rocks. In figure 9.8 the maximum rock spread has been plotted against the production and rock size with linear trend lines through the data points for each angle. Both figures suggest that the production and rock size barely influence the spread of the rocks, and that the spread is only influenced by the angle of the pipe. For these tests that directly translates to the stand-off distance because the floor of the tank is fixed when the angle and the SOD changes. The trends are the same for the bulk spread, as the bulk spread is just a large fraction of the maximum rock spread.

Figure 9.9 shows the offset measured in the tests. The offset is plotted against the angle in the left plot and against the production on the right. The figure on the left shows the same trend as the spread, where the offset increases as the angle decreases and the SOD increases. The figure on the right is plotted with linear trend lines through the data points for each measured angle, showing an increase in the offset when the production increases. Section 8.3 shows that an increase in production increases the velocity in the rock flow, and with a higher velocity it is logical that the rocks carry more horizontal velocity and travel further away from the pipe before slowing down and settling on the floor.

The same problem regarding statistical analysis exists for the analysis of the area below the pipe as for the analysis of the processes in the pipe, there is only one repeat or no repeats of the tests, which is not enough to calculate means and standard deviations. Therefore it cannot be checked if the single stone model is valid for rock installation through inclined pipes.

9.4.1 Results at the same height after the pipe

The results discussed in section 9.4 are all measured at the grate, thus for each angle a different stand-off distance. To investigate the influence of the angle on the offset, maximum spread and bulk spread, these parameters were estimated at the same point 25 cm below the pipe exit, the SOD at 75°. Figure 9.11 shows where the offset is estimated at 25 cm below the pipe. The height at which to estimate is determined the same way as the offset and the spread, by converting pixel distances to SI units. There is no clear yardstick indicating the distance below the pipe, only the size of the holes of the grate indicate scale. And in combination with the estimation of the location of the center of mass of the falling rock clusters, the results at 25 cm below the pipe are closer to estimations than indisputable measurements.

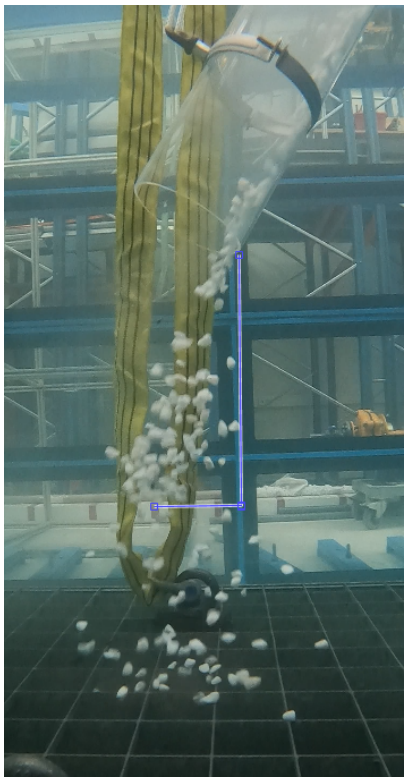

Figure 9.10: Measuring the offset at 25 cm below the pipe.

Figure 9.11 shows the maximum spread of the rocks at 25 cm below the pipe, on the left plotted against the angle and colored for the production, and on the right the reverse. The maximum spread at 25 cm below the pipe has approximately the same average, independent of the angle, production or rock size, at 0.25 m. The influence the production has on the spread of the rocks is that it introduces more variation in the results. This stems from the fact that more particles flow through the pipe at higher productions, so there is a higher chance for the rocks to fall further away from the center of mass. The bulk spread shows the same trend because it is a large fraction of the maximum spread.

Figure 9.12 shows the offset at 25 cm below the pipe plotted against the pipe angle, the production and the rock size. The left plot immediately shows the influence of the angle on the offset: the offset at the same height increases as the angle decreases. The rocks carry more horizontal velocity at the lower angles, thus the pipe ejects the rocks further away from the pipe. The plots next to it show the offset against the production and against the rock size. An increase in production increases the offset at 60° and 45°, but not at 75°. The influence of the rock size in comparison to the angle and production is mostly non-existent.

Figure 9.13 shows the offset at the floor against the offset at 25 cm below the pipe. The first points are the same because the SOD at 75° is 25 cm. The other points are from the tests at 60° and 45°. The offset at the floor is higher than the offset at 25 cm below the pipe, but the increase is slight. Most of the lateral movement due to the horizontal velocity the inclined pipe gives to the rocks happens in the first 25 cm below the pipe. The right plot shows that the difference between the offset at 25 cm and at the full SOD increases with increasing SOD.

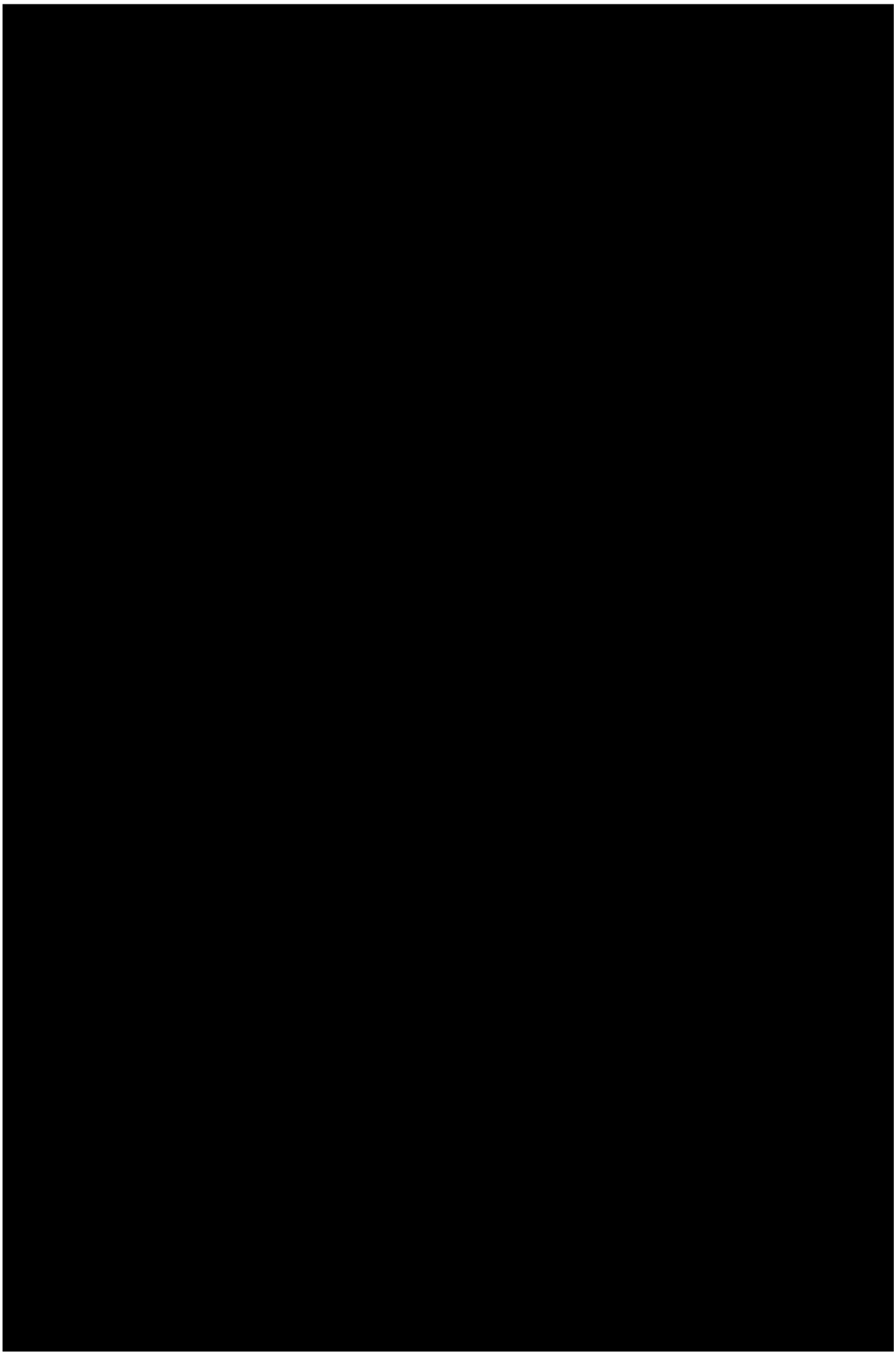

9.4.2 Comparison of the velocity in the pipe and below the pipe

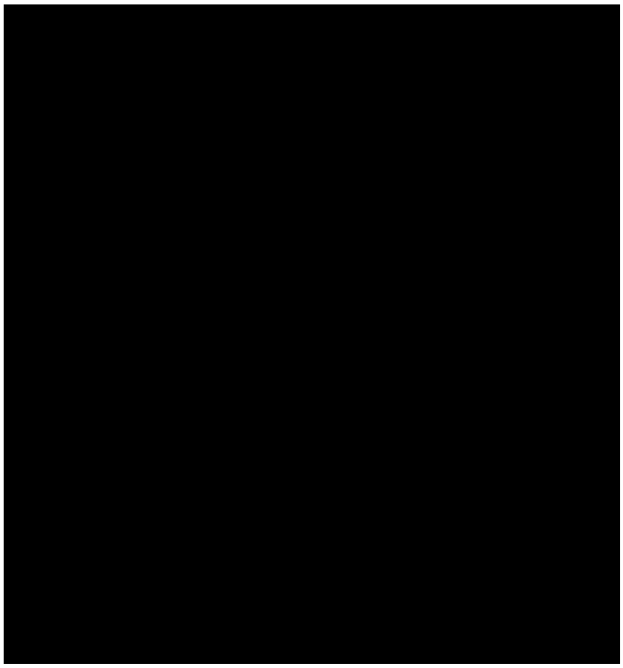

When the rocks flow through the pipe, the rocks have resistance from the pipe and from the return flow. When the rocks exit the pipe, these influences are gone. The rocks then fall unrestricted through the water, only influenced by the water and each other when they go through the four phases of falling groups. Figure 9.14 compares the velocity below the pipe with the velocity in the pipe. The velocity below the pipe is determined manually from the videos, between the lowest point of the pipe and the grate on the cement tub. It shows that the rocks are faster in the pipe at the steep angles (90° and 75°) and that the rocks are faster below the pipe for the lower angles (45° and 30°). The rocks have a low velocity at the lower angles, and then have a large distance to accelerate, creating a large discrepancy between the values in and below the pipe. At the steep angles the reverse happens. The rocks accelerate to a higher velocity in the pipe, but are slowed down by the water when exiting the pipe, and then do not have enough time to accelerate before reaching the bucket. If the stand-off distance was larger, the rocks would reach the same velocities below the pipe as the rocks at the lower angles.

As in all cases shown in this chapter, the pipe angle has the largest influence on the results. Figure 9.15 illustrates this when compared to figure 9.14. No trends are visible regarding the influence of the production or the rock size on the difference between the velocity in the pipe and below the pipe. One exception is the velocity of the largest rocks (16-32 mm). These rock are in nearly all experiments performed faster falling below the pipe than flowing through the pipe.

9.5 Conclusions

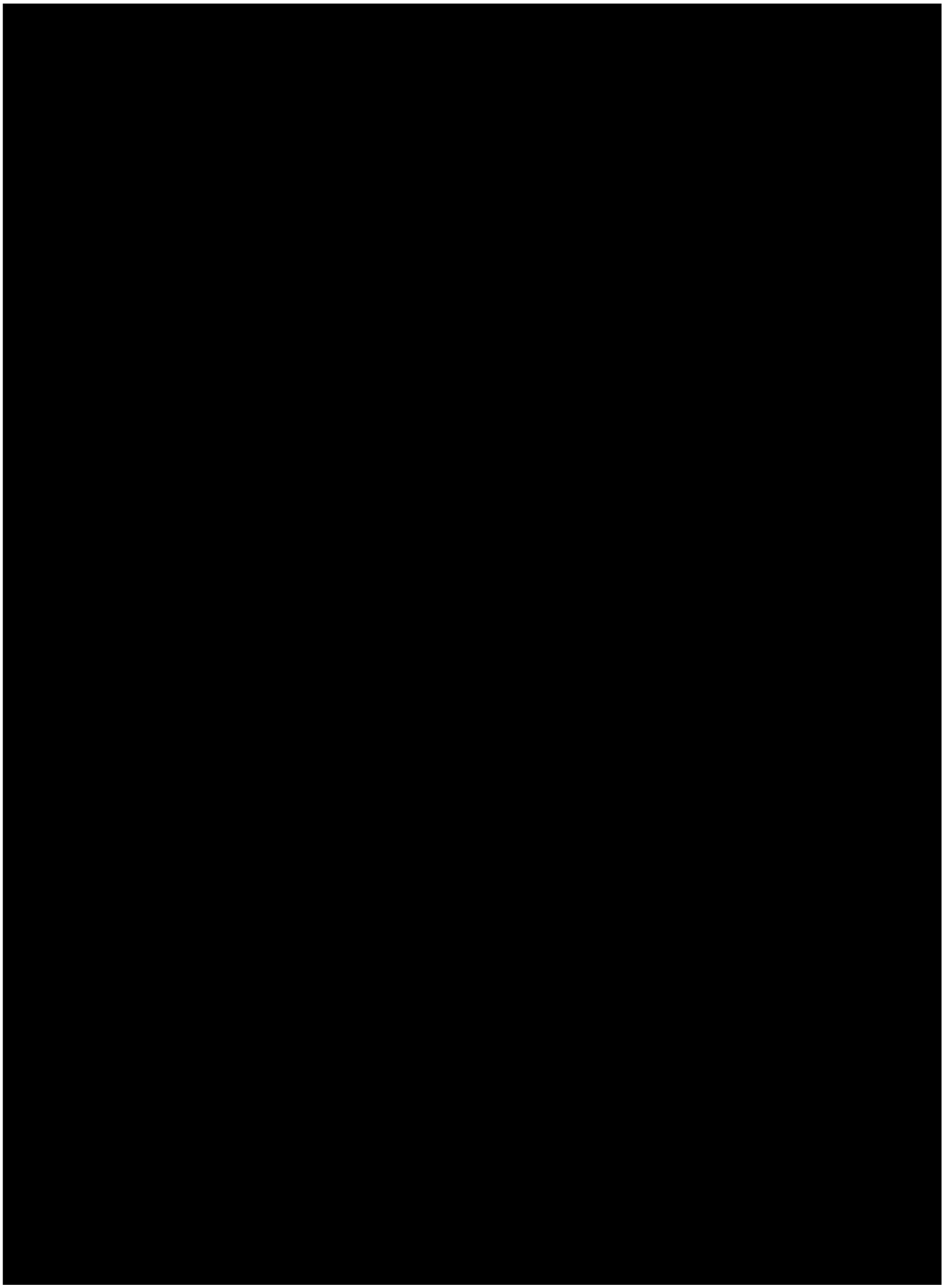

Chapter 10

Conclusions and recommendations

This chapter provides the conclusions to the analysis of the experiments to answer the research questions. Also, recommendations for future research are made.

The aim of this thesis is to gather knowledge on the processes in and below the inclined fall-pipe. The assessment of this behavior was twofold, the tests were analyzed for the behavior of the rock flow in the pipe, and for the behavior of the rocks below the inclined pipe.

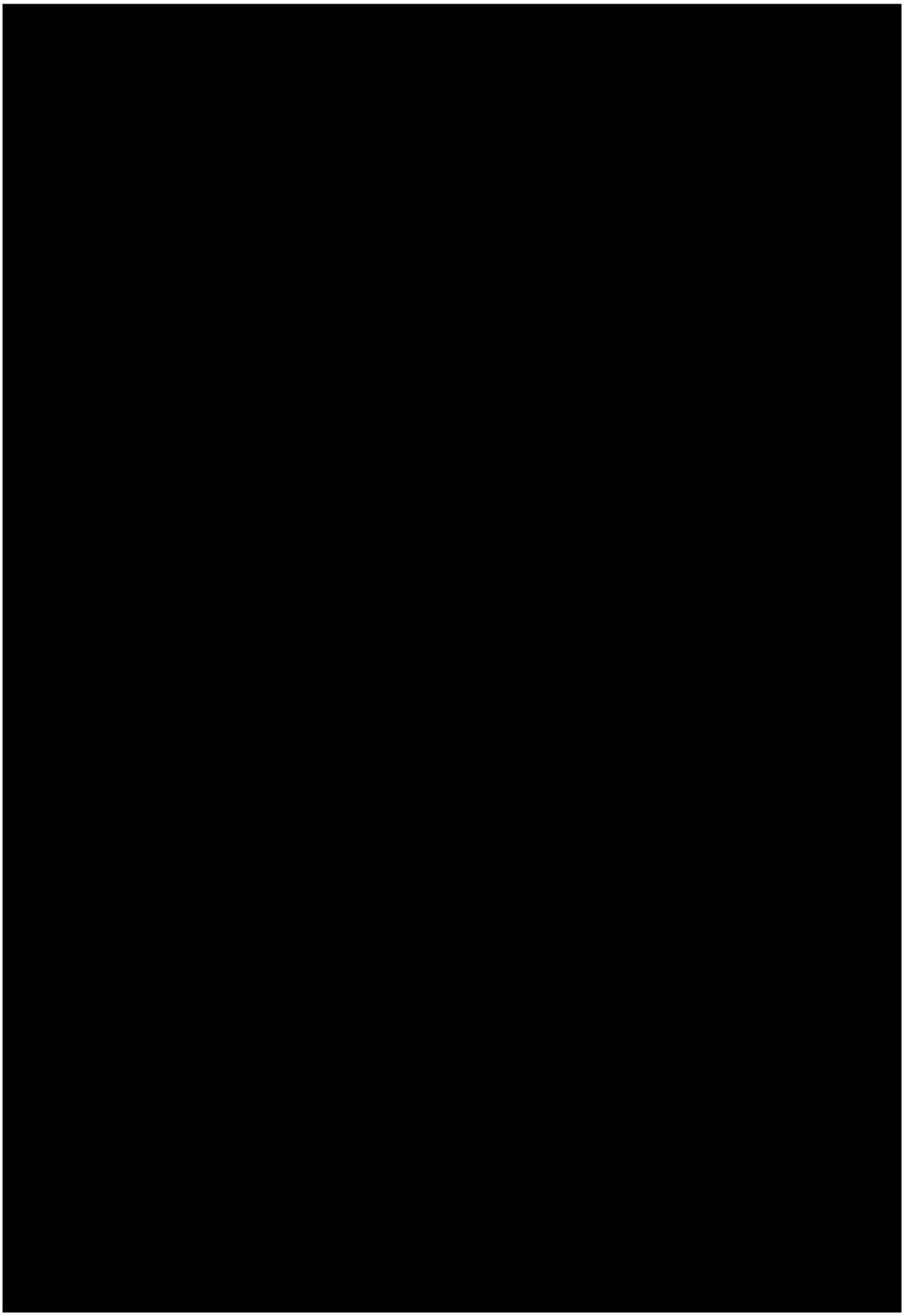

10.2 Recommendations

While the tests covered a broad expanse of parameters, there are still many situations that can be studied. For example, the SOD varied with angle for the tests, and the SOD can be kept the same to better research the effects of the angle on the spread and offset. The results only consider a static situation of the pipe in still waters. For real life operations at sea, the rocks are influenced by the currents and the vessel is influenced by the weather and waves. To investigate the influence of these factors, more experiments are needed under dynamic circumstances.

The spread of the rocks has only been measured in one direction for this thesis, and for further research, the spread of the rocks and their precise location can be measured, especially in combination with the effect of currents. The effect on bed impact from installing through an inclined pipe can also be measured in this case.

Finally, the gaps between the angles from the pipe were quite large, and more experiments can be done in the region between 90° and 75° for the transition between vertical and inclined pipe transport.

In addition to these recommendations, there are a few practical tips to improve the use of PIV, as it is a valuable tool for the analysis of the behavior in the pipe. First, to improve visibility, a plain white background behind the pipe, a mixture of black and white rocks for contrast, the camera closer to the pipe. Second, a better calibration for the camera below the pipe.

Bibliography

Chhabra, R. P., & Ferreira, J. M. (1999). An analytical study of the motion of a sphere rolling down a smooth inclined plane in an incompressible newtonian fluid. *Powder Technology*, *104*, 130–138. www.elsevier.com/locate/powtec

Chhabra, R. P., Kumar, M., & Prasad, R. (2000). Drag on spheres in rolling motion in inclined smooth tubes filled with incompressible liquids. *Powder Technology*, *113*, 114–118.

CIRIA, CUR, & CETMEF. (2007). *The rock manual. the use of rock in hydraulic engineering (2nd edition)* (2nd ed.). C683, CIRIA.

Cregten, H. (1995). *Het gebruik van probabilistische methoden bij het beoordelen van het stort- resultaat van een zijstorter* [Thesis]. TU Delft. http://resolver.tudelft.nl/uuid:a78ee7da-fae7-424b-99c5-f55f83068ad8

de Reus, J. (2004). *Het valgedrag van stortsteen onder invloed van stroming* [Thesis]. Delft University of Technology.

de Vries, M. (1977). *Hydrodynamic research* (lecture guide b80). TU Delft.

Dioguardi, F., Mele, D., & Dellino, P. (2018). A new one-equation model of fluid drag for irregularly shaped particles valid over a wide range of reynolds number. *Journal of Geophysical Research: Solid Earth*, *123*, 144–156. https://doi.org/10.1002/2017JB014926

Ferguson, R. I., & Church, M. (2004). A simple universal equation for grain settling velocity. *Journal of Sedimantary Research*, *74*, 933–937.

Gillies, R. G., Shook, C. A., & Wilson, K. C. (1991). An improved two layer model for horizontal slurry pipeline flow. *Canadian Journal of Chemical Engineering*, *69*, 173–178.

Go Mars, B. de. (2014). Drag coefficient of a sphere as a function of reynolds number [[Online; accessed May 12, 2022]]. https://commons.wikimedia.org/wiki/File:Drag_coefficient_of_a_sphere_as_a_function_of_Reynolds_number.png

Heller, V. (2011). Scale effects in physical hydraulic engineering models. *Journal of Hydraulic Research*, *49*, 293–306. https://doi.org/10.1080/00221686.2011.578914

Hughes, S. A. (1993). *Sediment transport models* (Vol. 7). WORLD SCIENTIFIC. https://doi.org/10.1142/2154

Joseph Straccia. (2016). Visualisation of the vortex street behind a circular cylinder in water [[Online; accessed February 10, 2023]]. https://www.flowvis.org/2016/11/20/a-3d-karman-vortex-street-in-water/

Major, J. J. (2003). *Hindered settling* (M. J., C. Mario, H. L. A., L. F. J. M. G. V., & Church, Eds.). Springer Netherlands. https://doi.org/10.1007/978-1-4020-3609-5_110

Matoušek, V., & Talmon, A. M. (2021). *Dredging pumps and slurry transport* (2nd ed.).

Matoušek, V. (1997). *Flow mechanism of sand-water mixtures in pipelines*. Delft University of Tech- nology.

Meermans, W. (1997). *Steenstorten - voorspelling van storten als gestort wordt vanuit een vast punt* [Thesis]. Delft University of Technology.

Miedema, S. (2019). *Slurry transport: Fundamentals, historical overview & dhlldv.* (R. C. Ramsdell, Ed.; 3rd ed.). https://doi.org/https://doi.org/10.5074/t.2019.002

Papantoniou, D., & Buhler, J. (1999). Barge dumping of rubble in deep water. *Environmental Hydraulics*, 193.

Richardson, J. F., & Zaki, W. N. (1954). The sedimentation of a suspension of uniform spheres under conditions of viscous flow. *Chemical Engineering Science*, *3*, 65–73.

Slack, G. W. (1963). Sedimentation of compact clusters of spheres. *Nature*, *200*, 466–467.

Thielicke, W. (2014). *The flapping flight of birds: Analysis and application* (Doctoral dissertation). University of Groningen. [S.n.]

Thielicke, W., & Sonntag, R. (2021). Particle image velocimetry for matlab: Accuracy and enhanced algorithms in pivlab. *Journal of Open Research Software*, *9*, 12. https://doi.org/10.5334/jors.334

van der Schrieck, G., & van Rhee, C. (2010). Physical scale modeling of dredging processes in sand and gravel [19th World Dredging Congress, Beijing, China ; Conference date: 08-09-2010 Through 12-09-2010]. In s.n. (Ed.), *19th world dredging congress* (pp. 859–874). WODA / CHIDA.

van der Wal, J. (2002). *Het valgedrag van steengroepen* [Thesis]. Delft University of Technology.

van Oord, G. (1996). *Spreiding van steen in het stortproces van schuifstorters: Modelproeven ter verificatie van het enkele steenmodel* [Thesis]. TUD. https://repository.tudelft.nl/islandora/object/uuid%5C%3A87326f1e-6524-43b7-81eb-95832e29fd2a

van Rhee, C. (2018). *Dredging processes ii* (2.1) [Lecture notes].

Visser, R., & van der Meer, J. (2008). Immediate displacement of the seabed during subsea rock installation. *Terra et Aqua*, 3–8.

Vrijling, J., Manni, R. J., & de Wilde, D. Prediction of the deposition-mound of dumped rubble. In: Rio de Janeiro: Copedec IV, 1995.

Wardhaugh, L. T., & Williams, M. C. (2014). Drag coefficients and rotational behavior of spheres descending through liquids along an inclined wall at high reynolds numbers. *Physics of Fluids*, *26*. https://doi.org/10.1063/1.4868489

Waterloopkundig-laboratorium. (1983). *Storten van grind in stromend water, m598*.

Wilson, K. C. (1976). A unified physically-based analysis of solid-liquid pipeline flow. *Proc. Hydro- transport 4*, 1–16.

Wilson, K. C., & Brown, N. P. (1982). Analysis of fluid friction in dense-phase pipeline flow. *The Canadian Journal of Chemical Engineering*, *60*, 83–86. https://doi.org/10.1002/cjce.5450600114

Appendix A

List of tests

Run	Angle (°)	Grade	Prod. (kg/s)
1	75	14 mm	Marbles
2	75	8-12 mm	0.48
3	75	8-12 mm	0.48
4	75	8-12 mm	0.48
5	75	8-12 mm	0.32
6	75	8-12 mm	0.32
7	75	8-12 mm	0.32
8	75	8-12 mm	0.16
9	75	8-12 mm	0.16
10	75	12-16 mm	0.48
11	75	12-16 mm	0.48
12	75	12-16 mm	0.32
13	75	12-16 mm	0.32
14	75	12-16 mm	0.16
15	75	12-16 mm	0.16
16	75	12-16 mm	0.16
17	60	8-12 mm	0.48
18	60	8-12 mm	0.48
19	60	8-12 mm	0.32
20	60		Marbles
21	60	8-12 mm	0.32
22	60	8-12 mm	0.16
23	60	8-12 mm	0.16
24	60	12-16 mm	0.48
25	60	12-16 mm	0.48
26	60	12-16 mm	0.48
27	60	12-16 mm	0.32
28	60	12-16 mm	0.16
29	45	8-12 mm	0.48
30	45	8-12 mm	0.48
31	45		Marbles
32	45	8-12 mm	0.32
33	45	8-12 mm	0.32
34	45	8-12 mm	0.16
35	45	8-12 mm	0.16
36	45	12-16 mm	0.48
37	accidentally skipped		
38	45	12-16 mm	0.48
39	45	12-16 mm	0.32
40	45	12-16 mm	0.32
41	45	12-16 mm	0.16
42	45	12-16 mm	0.16
43	45	12-16 mm	0.48
44	30	8-12 mm	0.48
45	30	8-12 mm	0.48
46	30	8-12 mm	0.32
47	30	8-12 mm	0.32
48	30	8-12 mm	0.16
49	30	8-12 mm	0.16
50	30	12-16 mm	0.48
51	30	12-16 mm	0.32
52	30		
53	30	12-16 mm	0.72
54	30	8-16 mm	0.48
55	30	8-12 mm	0.72
56	90	8-12 mm	0.48
57	90		Marbles
58	90	8-12 mm	0.32
59	90	8-12 mm	0.16
60	90	8-12 mm	0.64
61	90	8-16 mm	0.48
62	90	12-16 mm	0.64
63	90	12-16 mm	0.48
64	90	12-16 mm	0.32
65	90	12-16 mm	0.16
66	75	8-12 mm	0.64
67	75	12-16 mm	0.64
68	75	8-16 mm	0.48
69	60	8-12 mm	0.64
70	60	12-16 mm	0.64
71	60	8-16 mm	0.48
72	60	8-12 mm	—
73	45	8-12 mm	0.64
74	45	12-16 mm	0.64
75	45	8-16 mm	0.48
75	45	8-16 mm	0.48
76	75	16-32 mm	0.32
77	75	16-32 mm	0.16
78	60	16-32 mm	0.32
79	60	16-32 mm	0.16
80	45	16-32 mm	0.32
81	45	16-32 mm	0.16
82	30	16-32 mm	0.32
83	30	16-32 mm	0.16
84	90	16-32 mm	0.32
85	90	16-32 mm	0.16
86	90	16-32 mm	0.48
87	90	16-32 mm	0.96
88	45	8-12mm	0.32
89	45	12-16 mm	0.32
90	60	8-12 mm	0.32
91	60	12-16 mm	0.32

Appendix B

Table with test results

This appendix contains the raw results of the analysis of the tests in table form.

Appendix C

PIVlab results

This appendix contains the figures with the results from the PIV analysis in PIVlab.

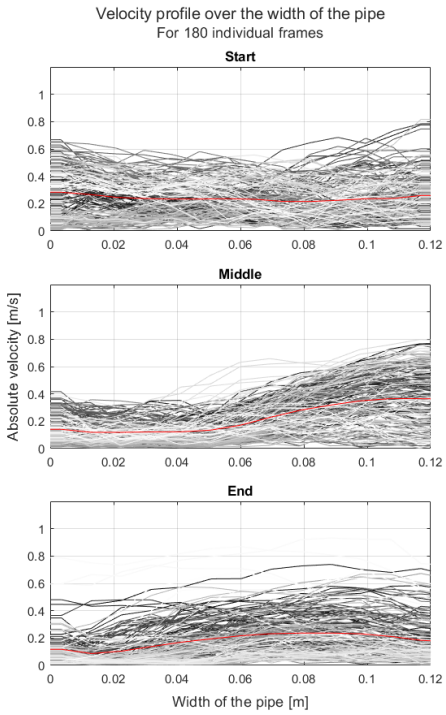

Figure C.1: Horizontal velocity profiles run 03, 75°, 0.48 kg/s, 8-12 mm.

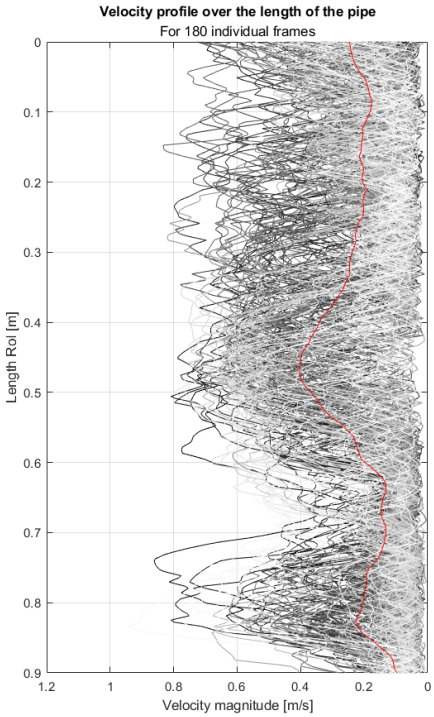

Figure C.2: Vertical velocity profiles run 03, 75°, 0.48 kg/s, 8-12 mm.

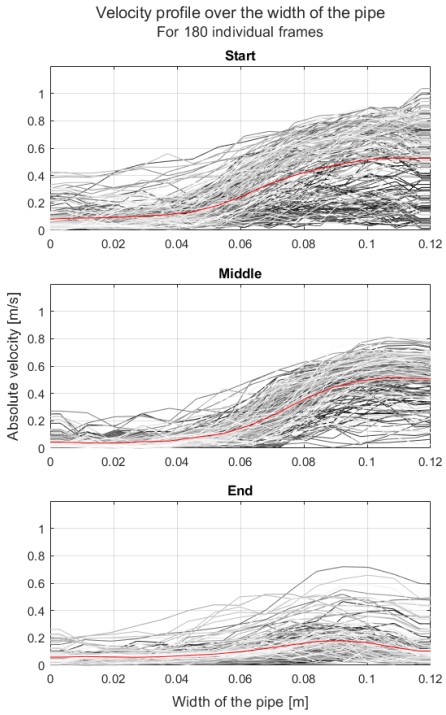

Figure C.3: Horizontal velocity profiles run 05, 75°, 0.32 kg/s, 8-12 mm.

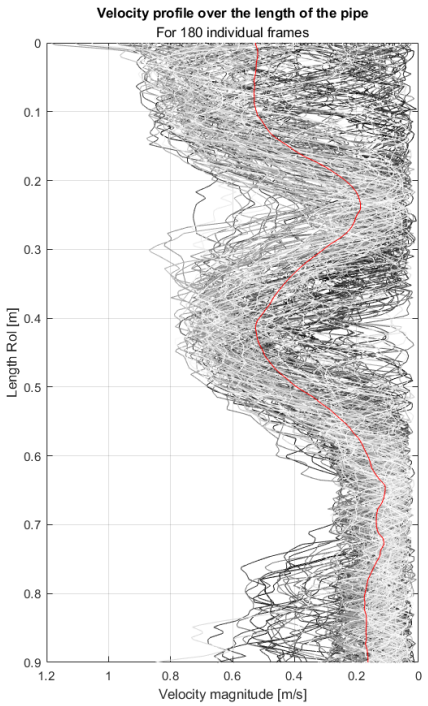

Figure C.4: Vertical velocity profiles run 05, 75°, 0.32 kg/s, 8-12 mm.

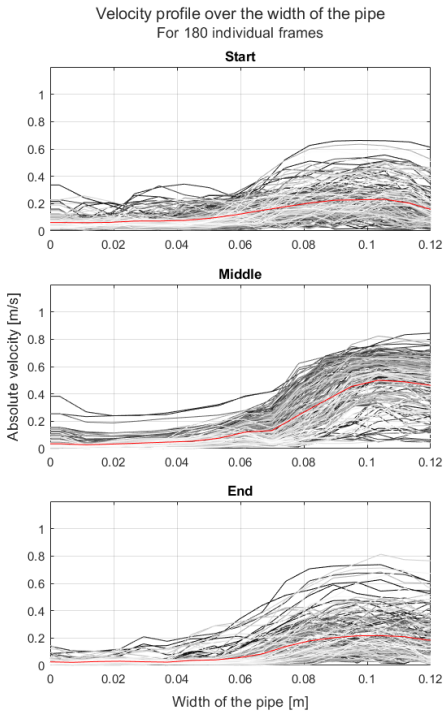

Figure C.5: Horizontal velocity profiles run 08, 75°, 0.16 kg/s, 8-12 mm.

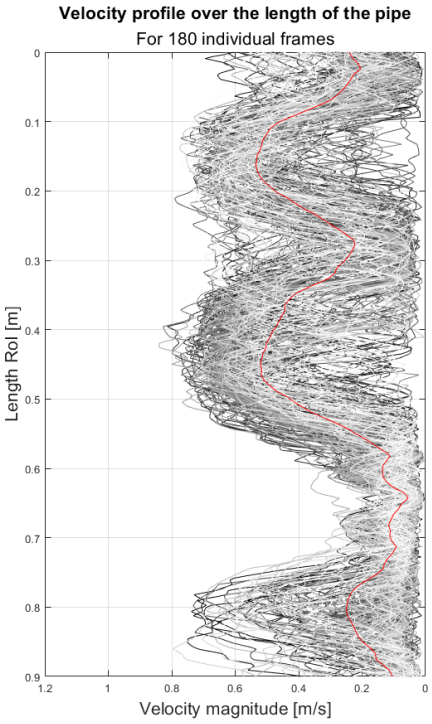

Figure C.6: Vertical velocity profiles run 08, 75°, 0.16 kg/s, 8-12 mm.

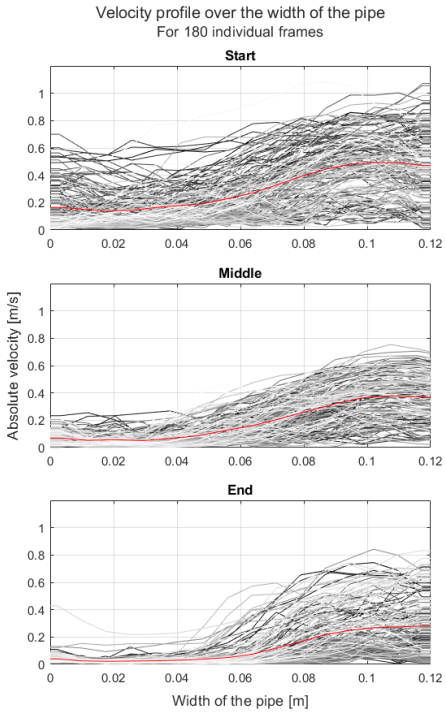

Figure C.7: Horizontal velocity profiles run 10, 75°, 0.48 kg/s, 12-16 mm.

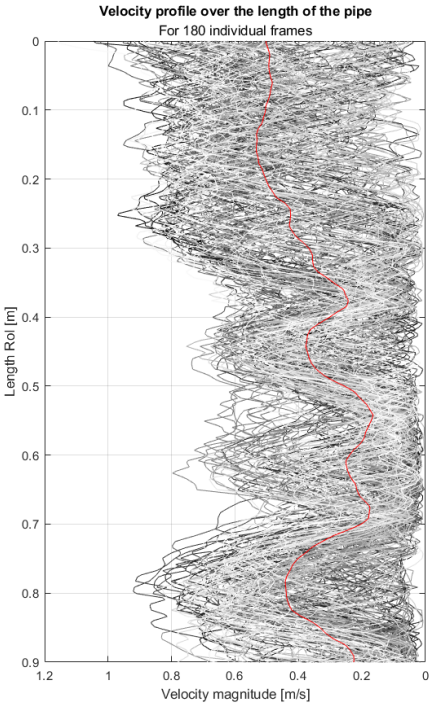

Figure C.8: Vertical velocity profiles run 10, 75°, 0.48 kg/s, 12-16 mm.

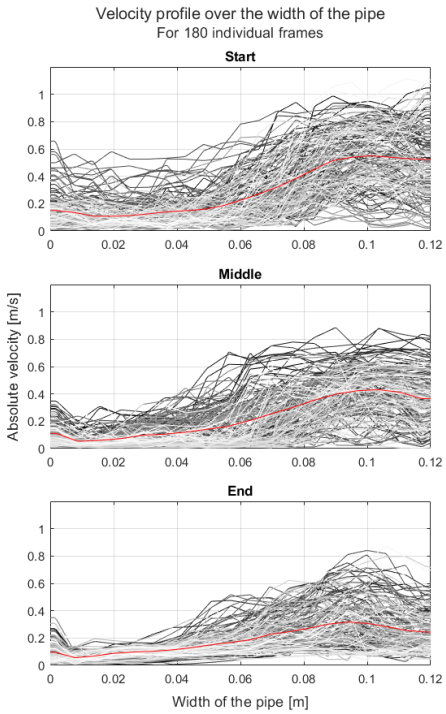

Figure C.9: Horizontal velocity profiles run 12, 75°, 0.32 kg/s, 12-16 mm.

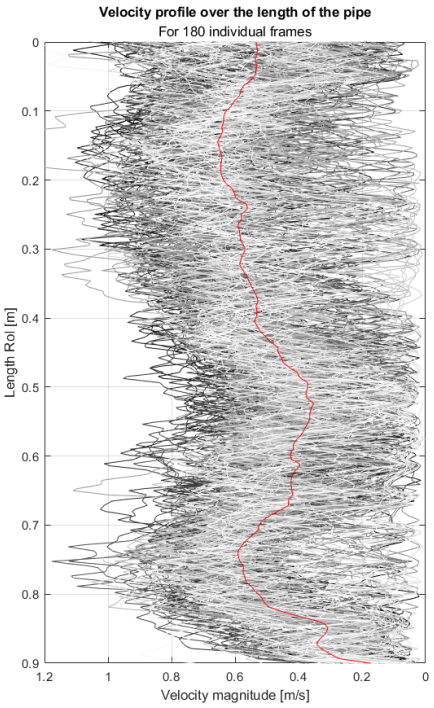

Figure C.10: Vertical velocity profiles run 12, 75°, 0.32 kg/s, 12-16 mm.

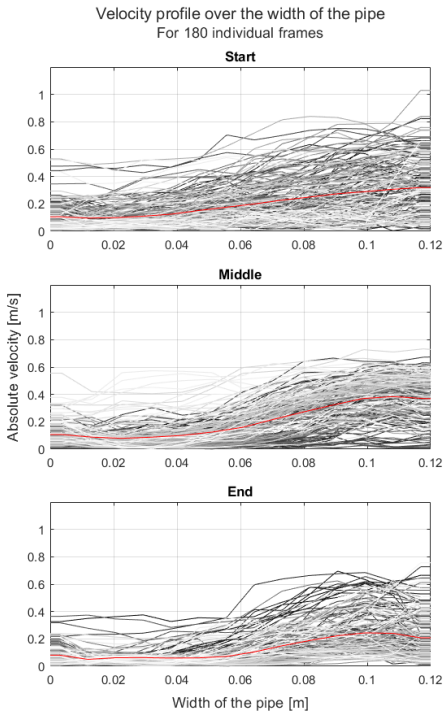

Figure C.11: Horizontal velocity profiles run 14, 75°, 0.16 kg/s, 12-16 mm.

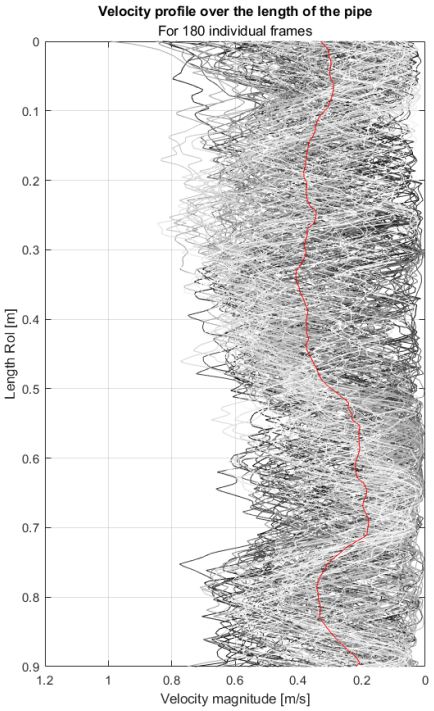

Figure C.12: Vertical velocity profiles run 14, 75°, 0.16 kg/s, 12-16 mm.

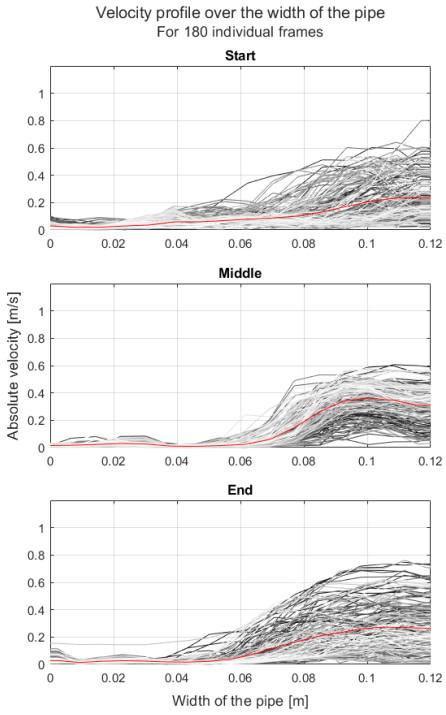

Figure C.13: Horizontal velocity profiles run 17, 60°, 0.48 kg/s, 8-12 mm.

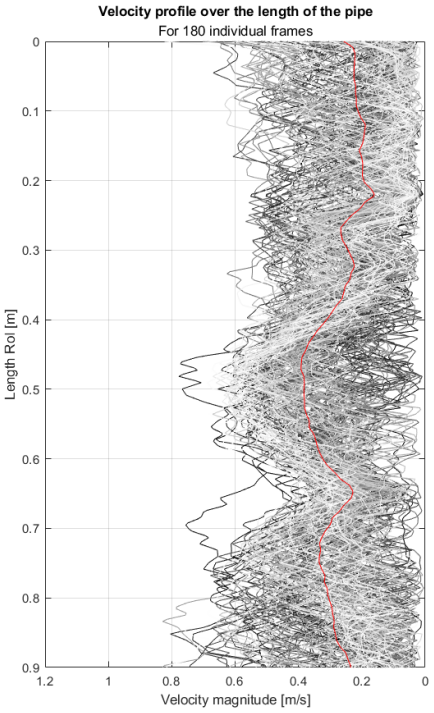

Figure C.14: Vertical velocity profiles run 17, 60°, 0.48 kg/s, 8-12 mm.

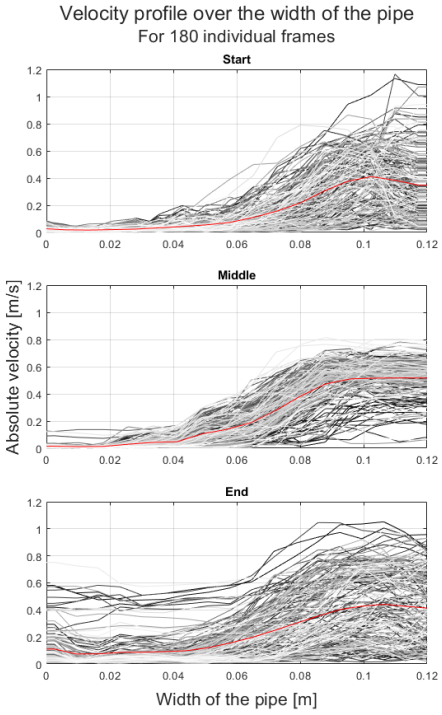

Figure C.15: Horizontal velocity profiles run 19, 60°, 0.32 kg/s, 8-12 mm.

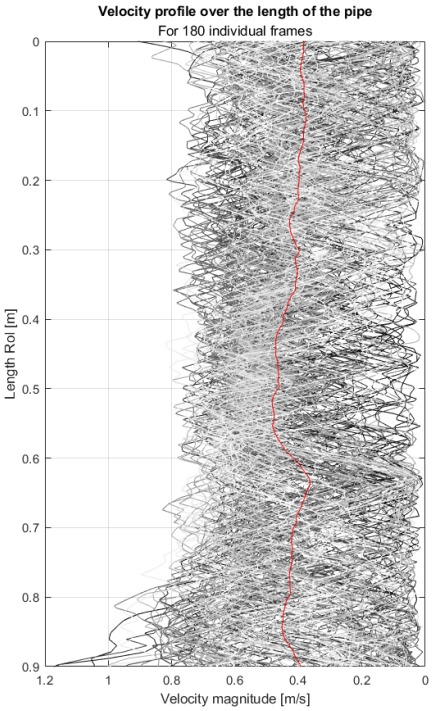

Figure C.16: Vertical velocity profiles run 19, 60°, 0.32 kg/s, 8-12 mm.

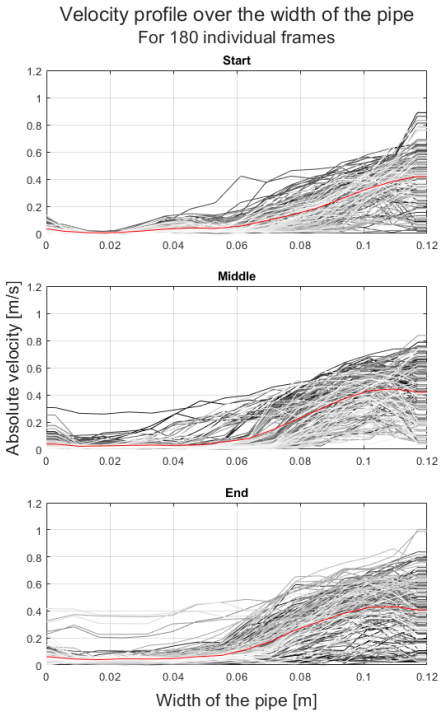

Figure C.17: Horizontal velocity profiles run 22, 60°, 0.16 kg/s, 8-12 mm.

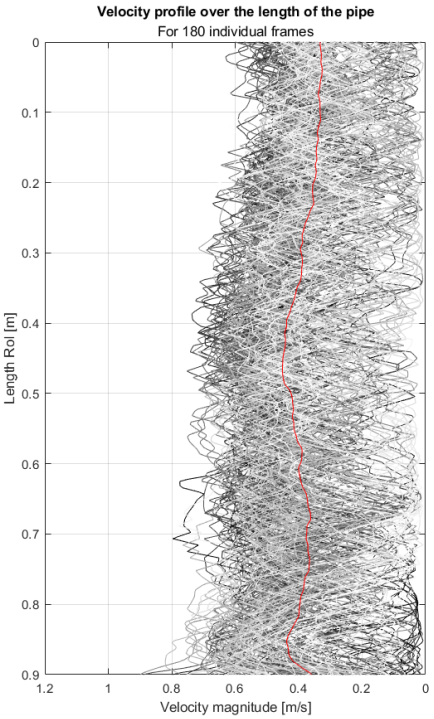

Figure C.18: Vertical velocity profiles run 22, 60°, 0.16 kg/s, 8-12 mm.

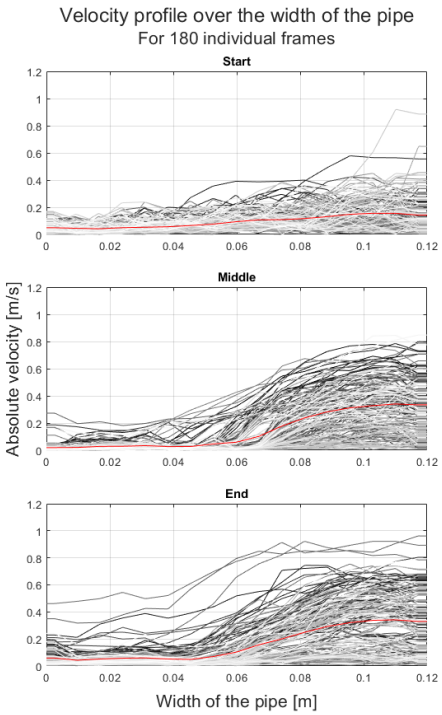

Figure C.19: Horizontal velocity profiles run 25, 60°, 0.48 kg/s, 12-16 mm.

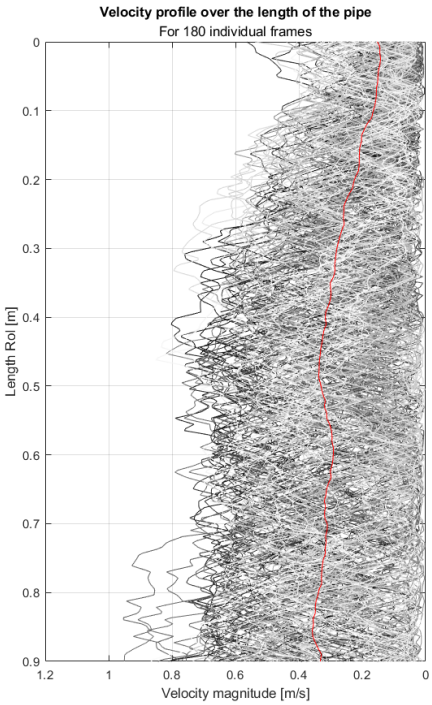

Figure C.20: Vertical velocity profiles run 25, 60°, 0.48 kg/s, 12-16 mm.

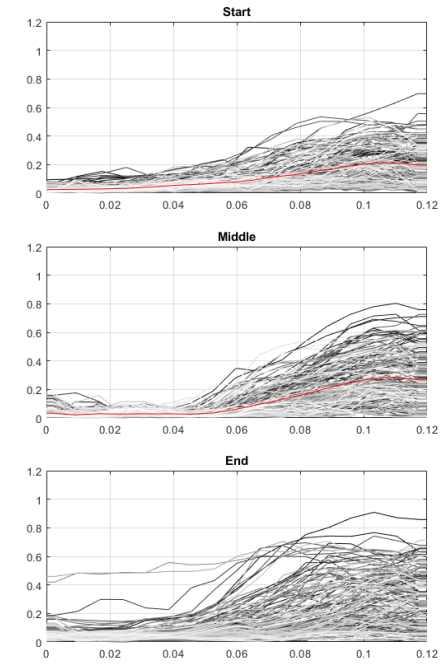

Figure C.21: Horizontal velocity profiles run 27, 60°, 0.32 kg/s, 12-16 mm.

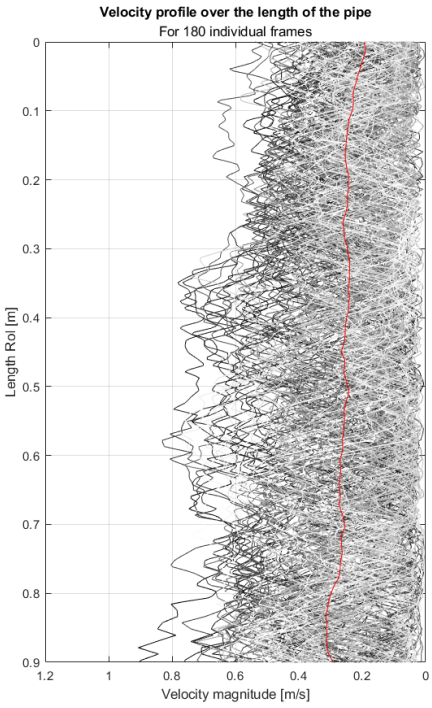

Figure C.22: Vertical velocity profiles run 27, 60°, 0.32 kg/s, 12-16 mm.

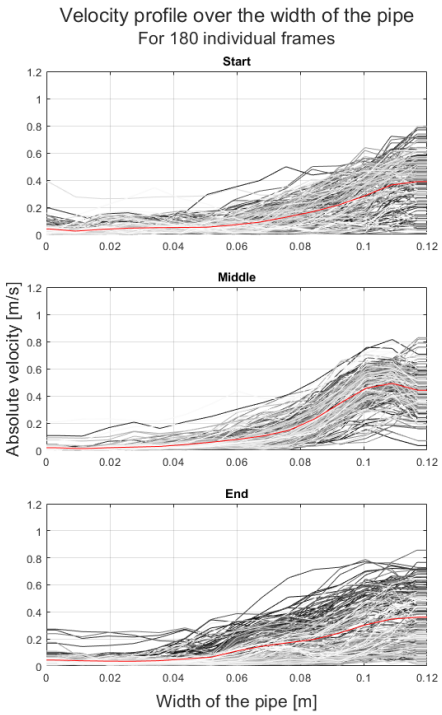

Figure C.23: Horizontal velocity profiles run 30, 45°, 0.48 kg/s, 8-12 mm.

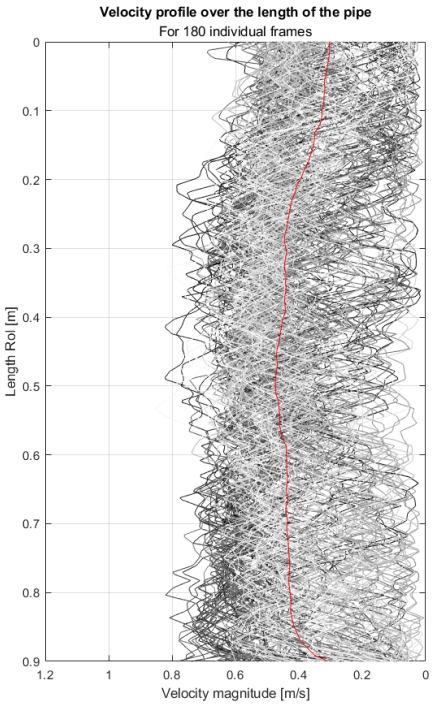

Figure C.24: Vertical velocity profiles run 30, 45°, 0.48 kg/s, 8-12 mm.

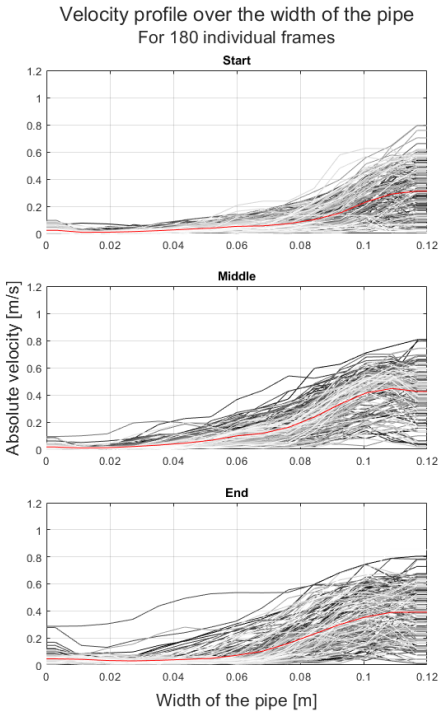

Figure C.25: Horizontal velocity profiles run 32, 45°, 0.32 kg/s, 8-12 mm.

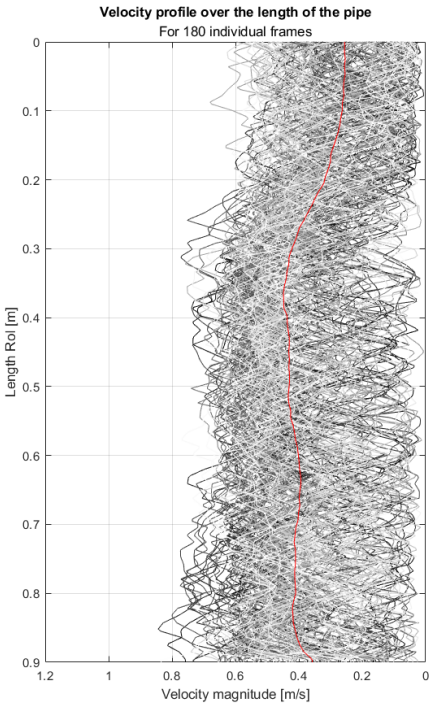

Figure C.26: Vertical velocity profiles run 32, 45°, 0.32 kg/s, 8-12 mm.

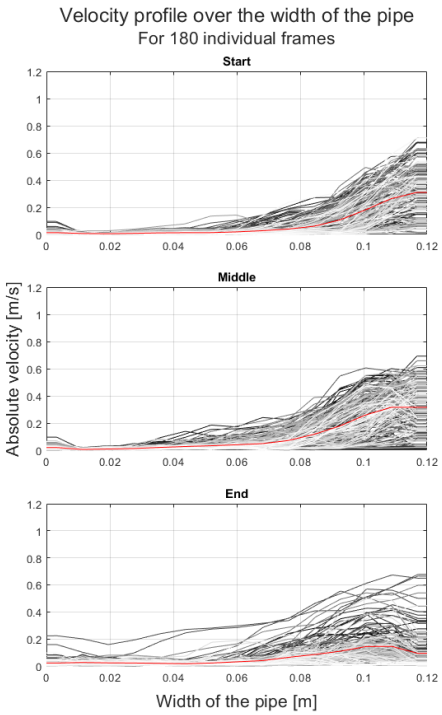

Figure C.27: Horizontal velocity profiles run 34, 45°, 0.16 kg/s, 8-12 mm.

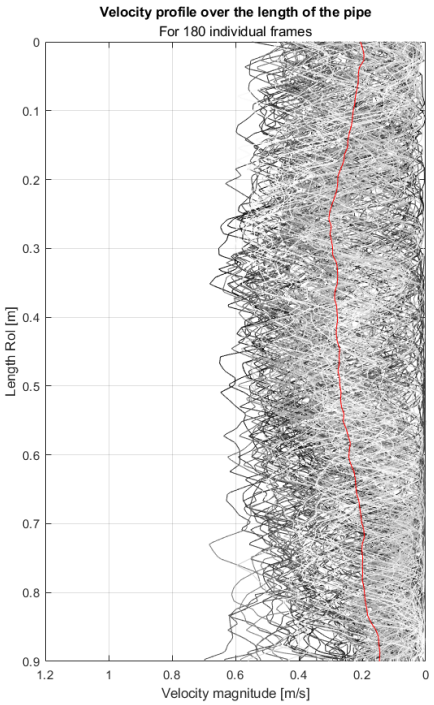

Figure C.28: Vertical velocity profiles run 34, 45°, 0.16 kg/s, 8-12 mm.

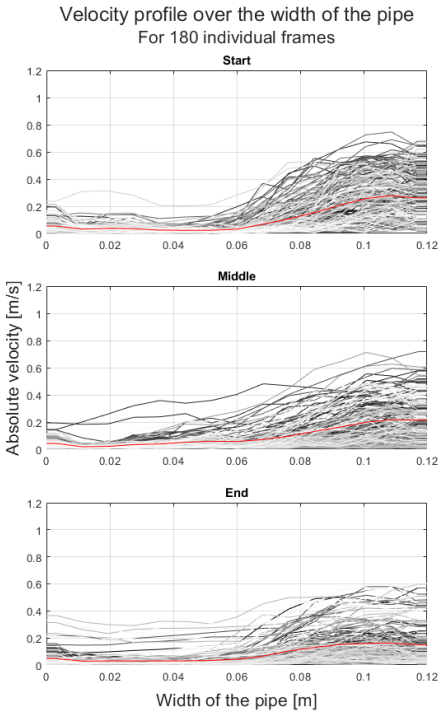

Figure C.29: Horizontal velocity profiles run 36, 45°, 0.48 kg/s, 12-16 mm.

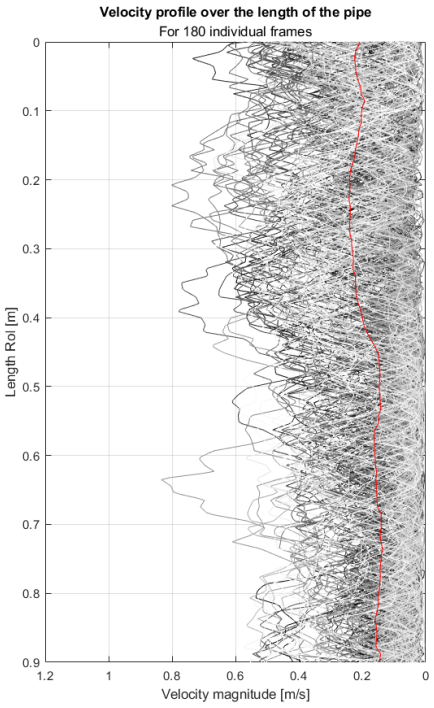

Figure C.30: Vertical velocity profiles run 36, 45°, 0.48 kg/s, 12-16 mm.

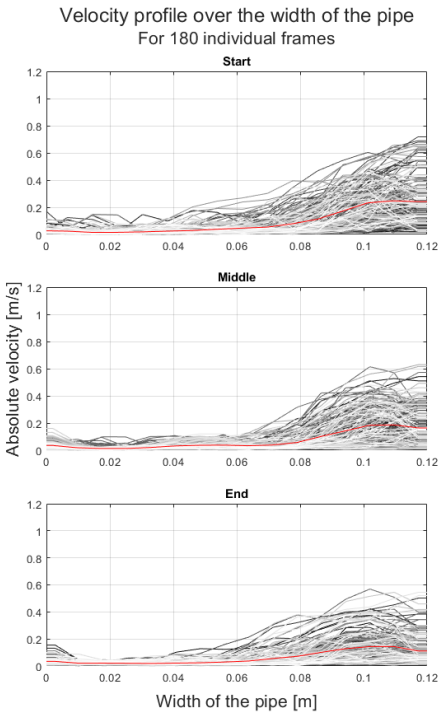

Figure C.31: Horizontal velocity profiles run 40, 45°, 0.32 kg/s, 12-16 mm.

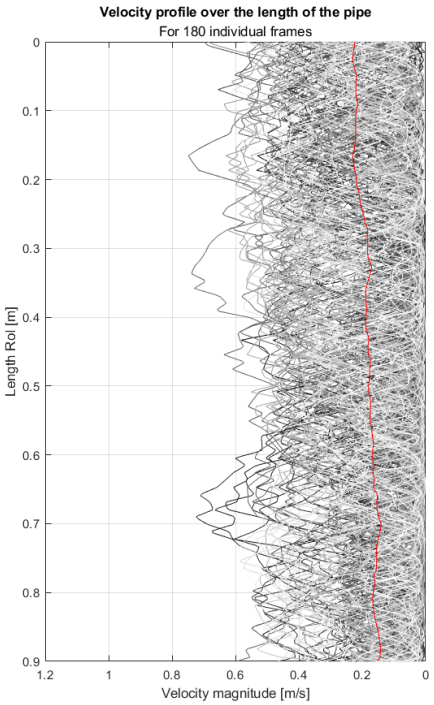

Figure C.32: Vertical velocity profiles run 40, 45°, 0.32 kg/s, 12-16 mm.

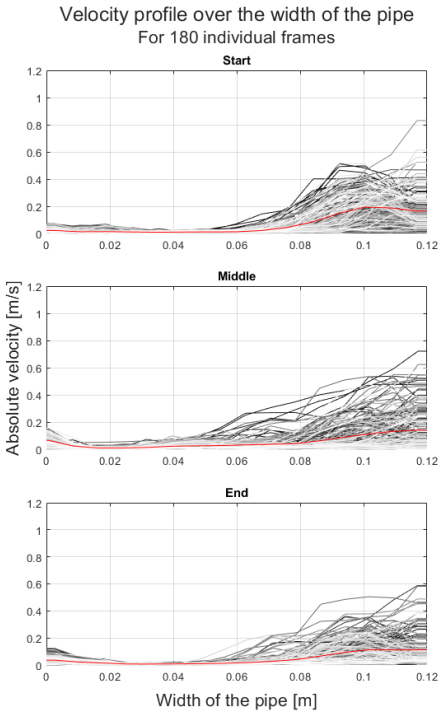

Figure C.33: Horizontal velocity profiles run 41, 45°, 0.16 kg/s, 12-16 mm.

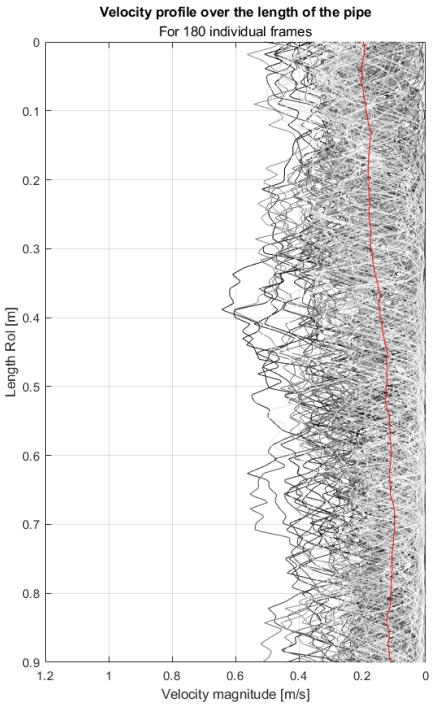

Figure C.34: Vertical velocity profiles run 41, 45°, 0.16 kg/s, 12-16 mm.

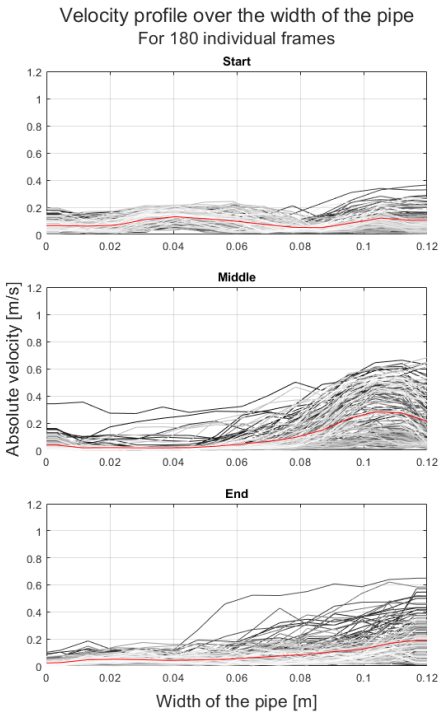

Figure C.35: Horizontal velocity profiles run 45, 30°, 0.48 kg/s, 8-12 mm.

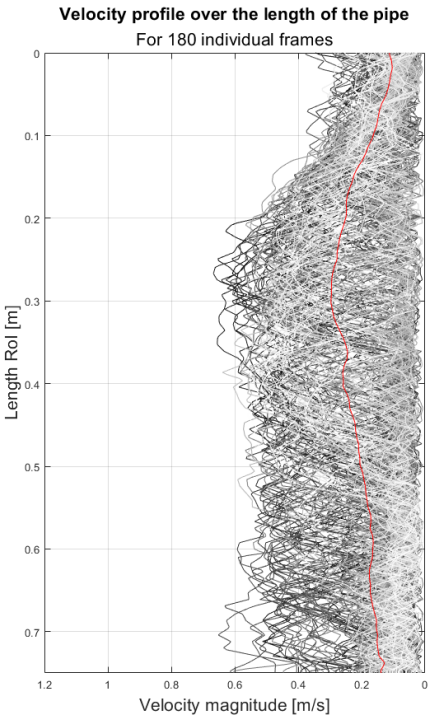

Figure C.36: Vertical velocity profiles run 45, 30°, 0.48 kg/s, 8-12 mm.

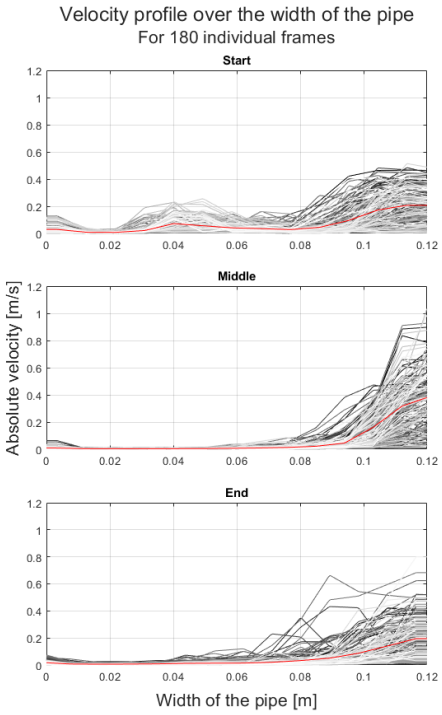

Figure C.37: Horizontal velocity profiles run 47, 30°, 0.32 kg/s, 8-12 mm.

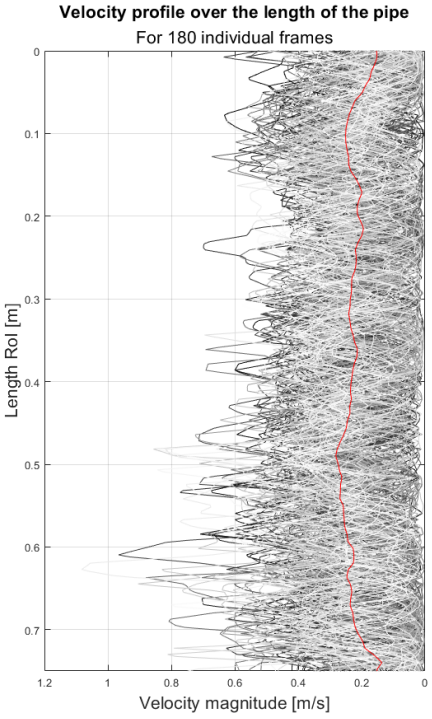

Figure C.38: Vertical velocity profiles run 47, 30°, 0.32 kg/s, 8-12 mm.

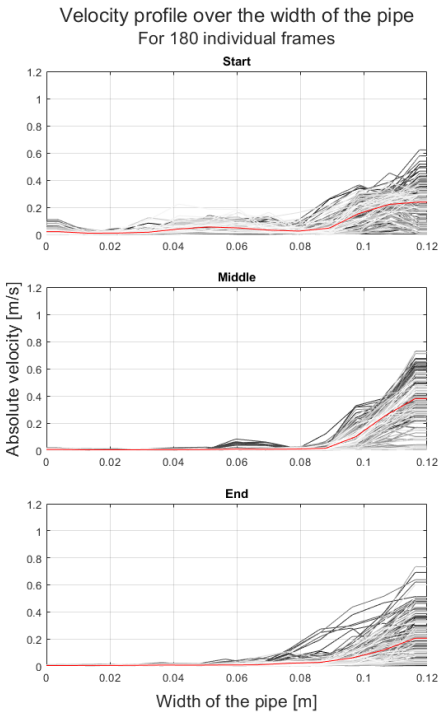

Figure C.39: Horizontal velocity profiles run 49, 30°, 0.16 kg/s, 8-12 mm.

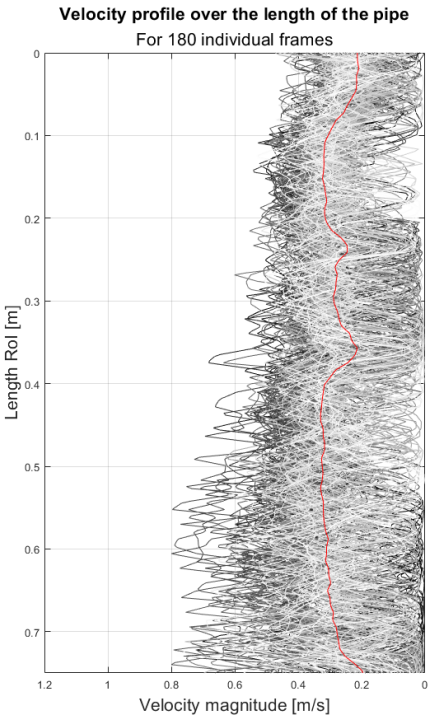

Figure C.40: Vertical velocity profiles run 49, 30°, 0.16 kg/s, 8-12 mm.

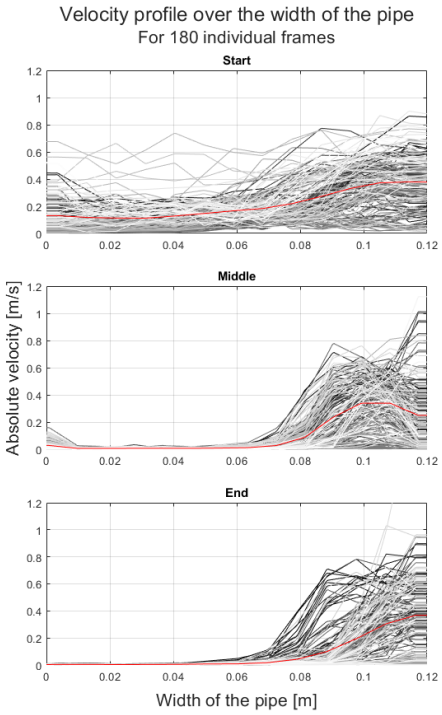

Figure C.41: Horizontal velocity profiles run 50, 30°, 0.48 kg/s, 12-16 mm.

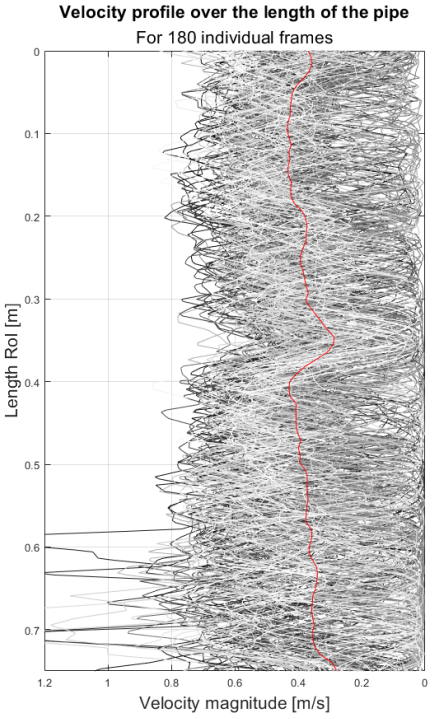

Figure C.42: Vertical velocity profiles run 50, 30°, 0.48 kg/s, 12-16 mm.

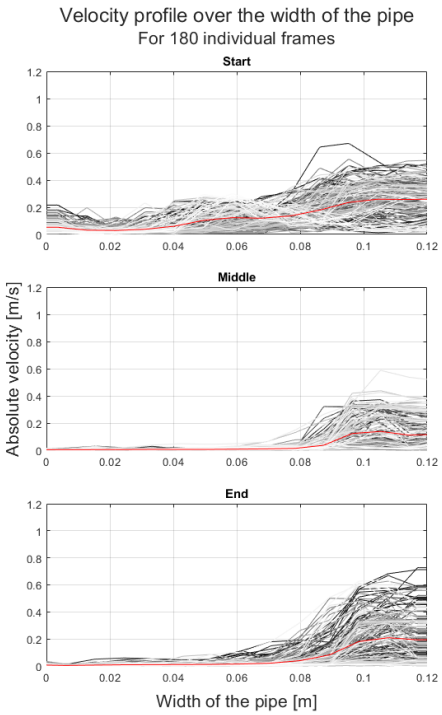

Figure C.43: Horizontal velocity profiles run 51, 30°, 0.32 kg/s, 12-16 mm.

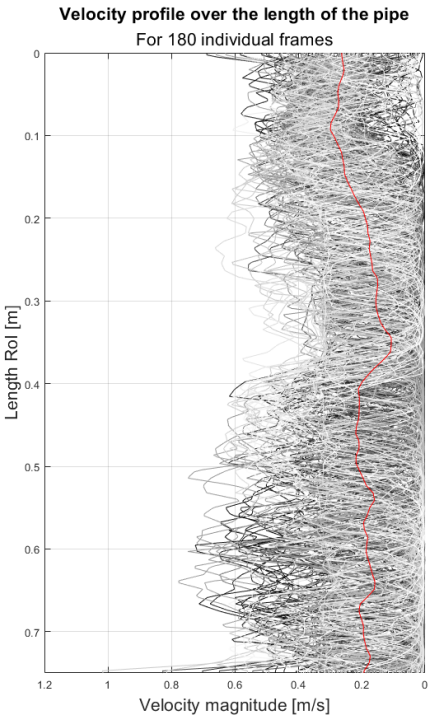

Figure C.44: Vertical velocity profiles run 51, 30°, 0.32 kg/s, 12-16 mm.

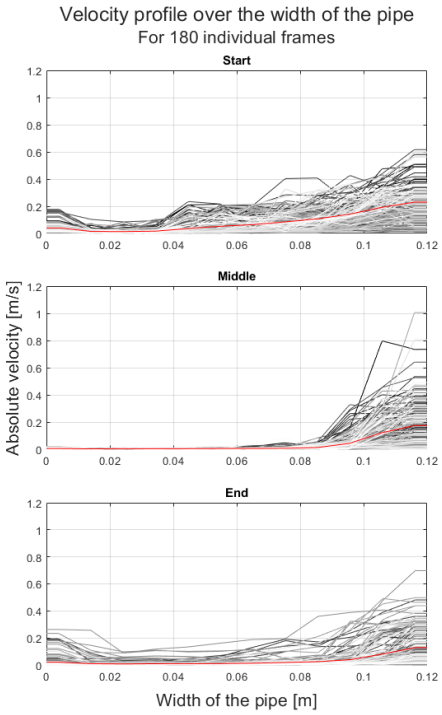

Figure C.45: Horizontal velocity profiles run 52, 30°, 0.16 kg/s, 12-16 mm.

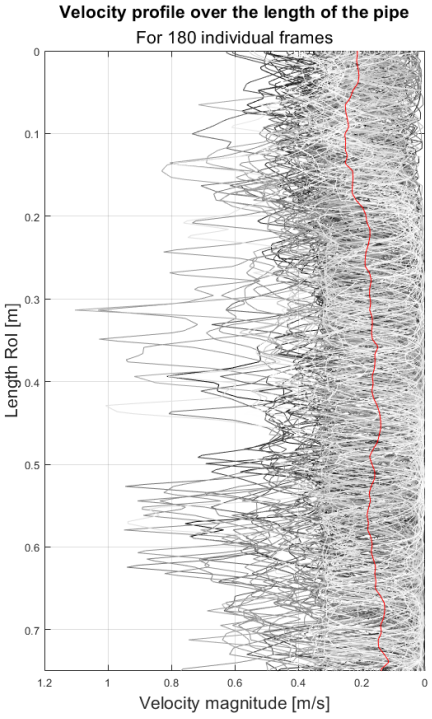

Figure C.46: Vertical velocity profiles run 52, 30°, 0.16 kg/s, 12-16 mm.

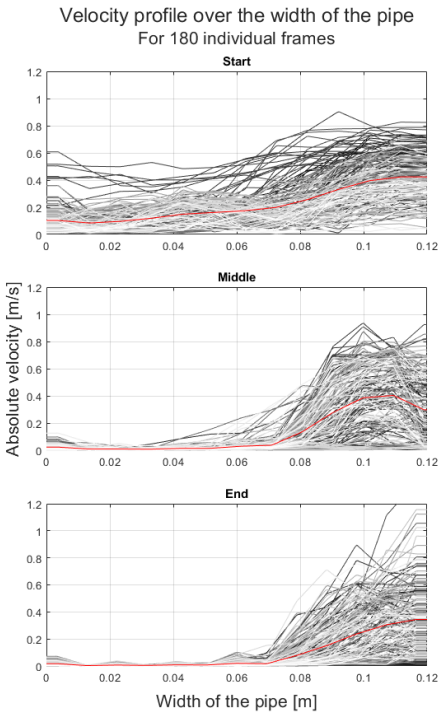

Figure C.47: Horizontal velocity profiles run 53, 30°, 0.64 kg/s, 12-16 mm.

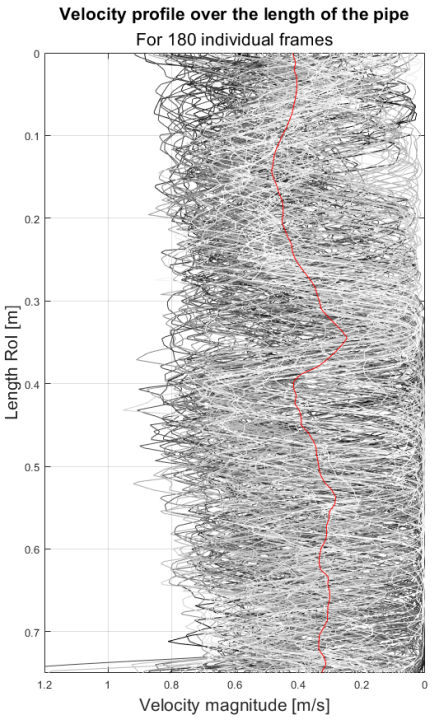

Figure C.48: Vertical velocity profiles run 53, 30°, 0.64 kg/s, 12-16 mm.

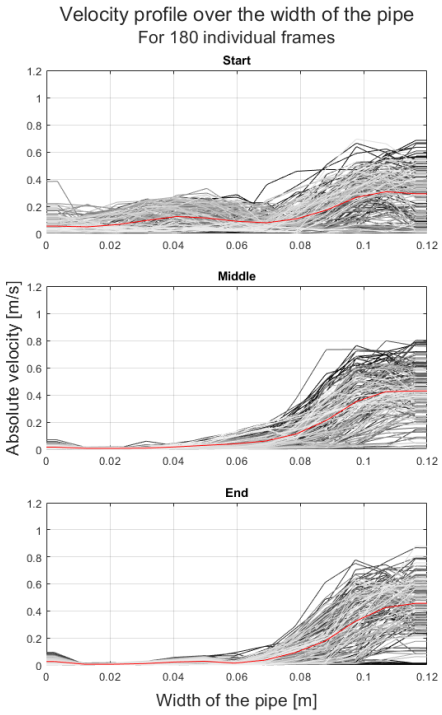

Figure C.49: Horizontal velocity profiles run 54, 30°, 0.48 kg/s, 8-16 mm.

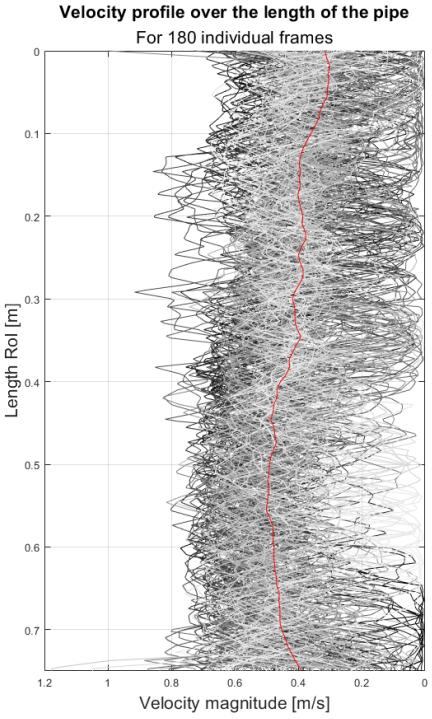

Figure C.50: Vertical velocity profiles run 54, 30°, 0.48 kg/s, 8-16 mm.

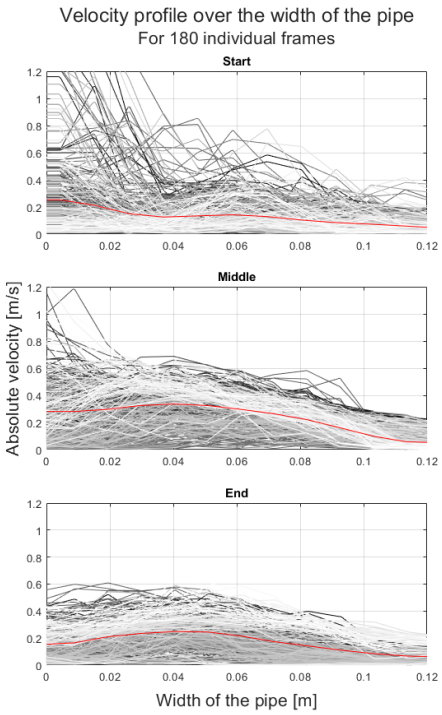

Figure C.51: Horizontal velocity profiles run 56, 90°, 0.48 kg/s, 8-12 mm.

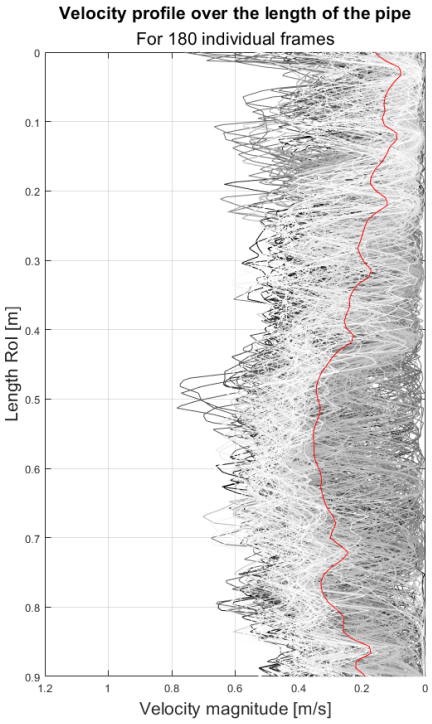

Figure C.52: Vertical velocity profiles run 56, 90°, 0.48 kg/s, 8-12 mm.

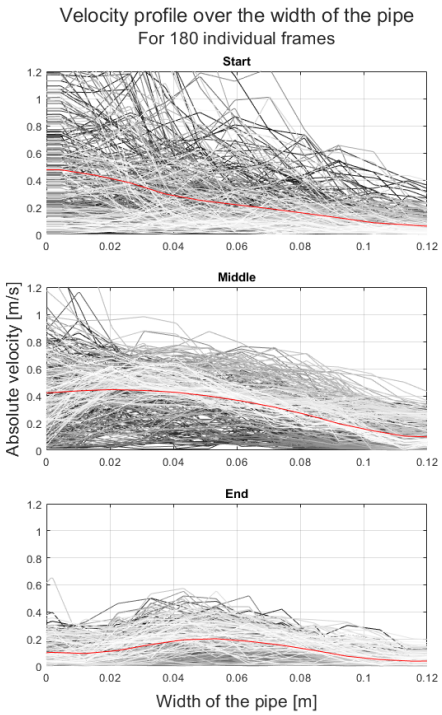

Figure C.53: Horizontal velocity profiles run 58, 90°, 0.32 kg/s, 8-12 mm.

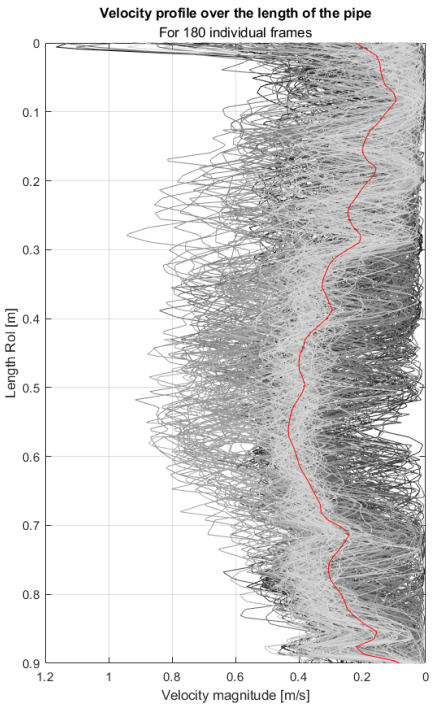

Figure C.54: Vertical velocity profiles run 58, 90°, 0.32 kg/s, 8-12 mm.

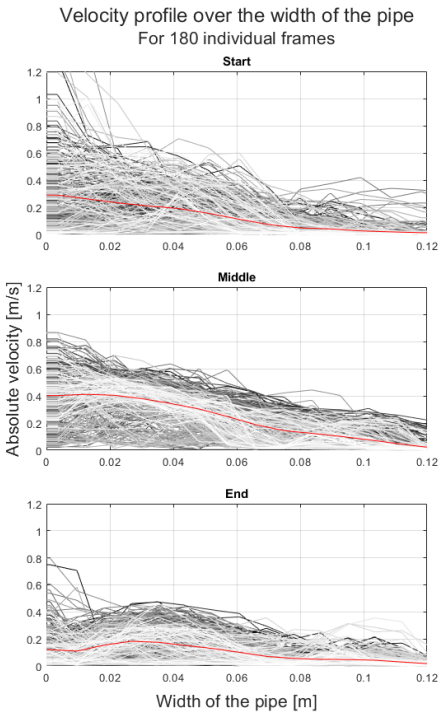

Figure C.55: Horizontal velocity profiles run 59, 90°, 0.64 kg/s, 8-12 mm.

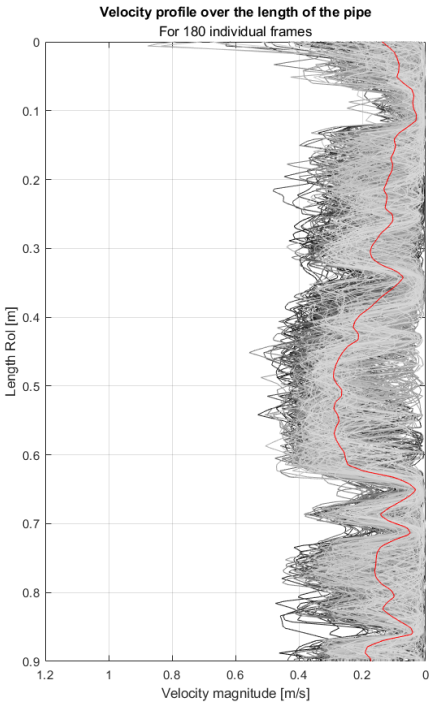

Figure C.56: Vertical velocity profiles run 59, 90°, 0.64 kg/s, 8-12 mm.

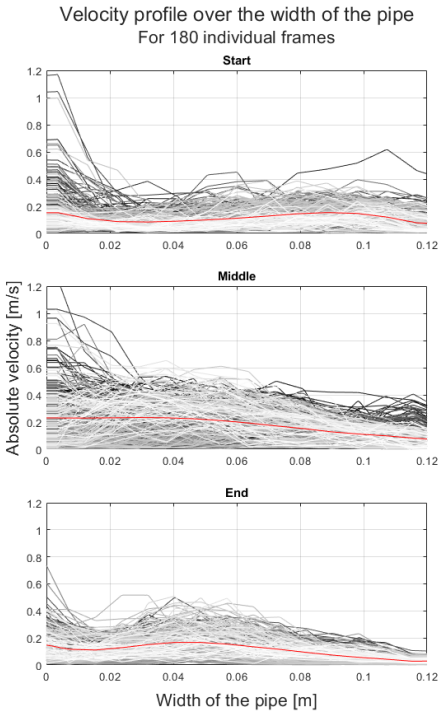

Figure C.57: Horizontal velocity profiles run 60, 90°, 0.64 kg/s, 8-12 mm.

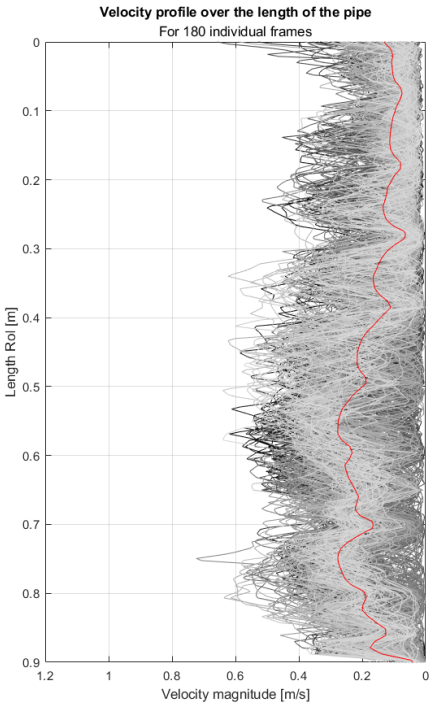

Figure C.58: Vertical velocity profiles run 60, 90°, 0.64 kg/s, 8-12 mm.

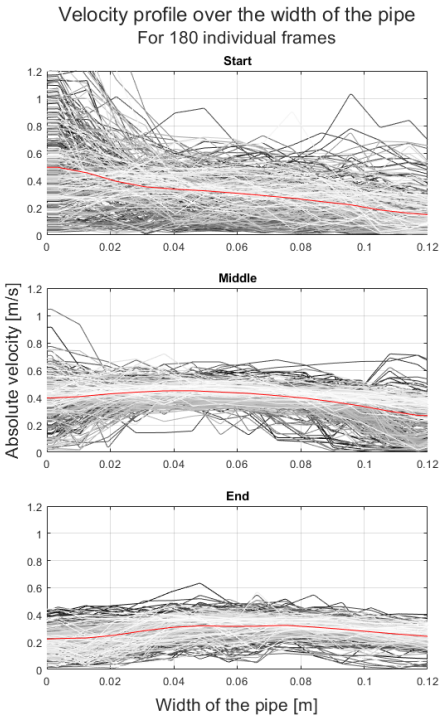

Figure C.59: Horizontal velocity profiles run 61, 90°, 0.48 kg/s, 8-16 mm.

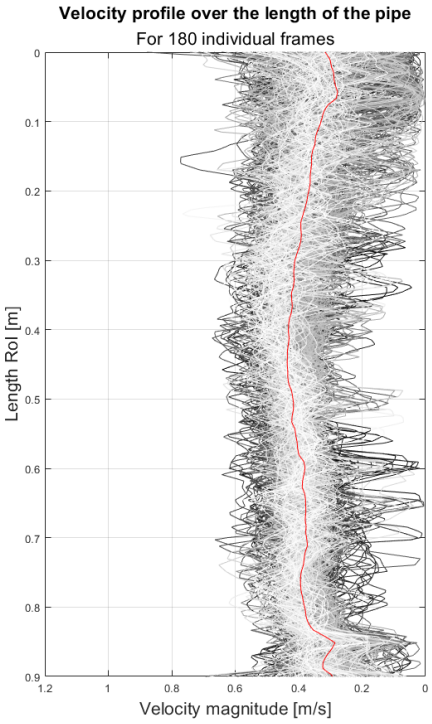

Figure C.60: Vertical velocity profiles run 61, 90°, 0.48 kg/s, 8-16 mm.

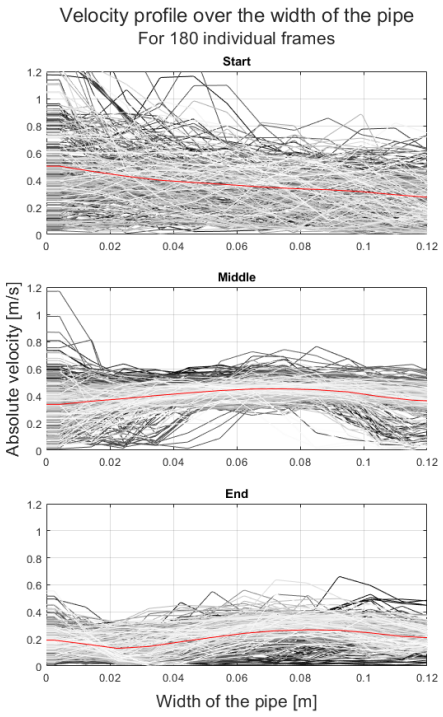

Figure C.61: Horizontal velocity profiles run 62, 90°, 0.64 kg/s, 12-16 mm.

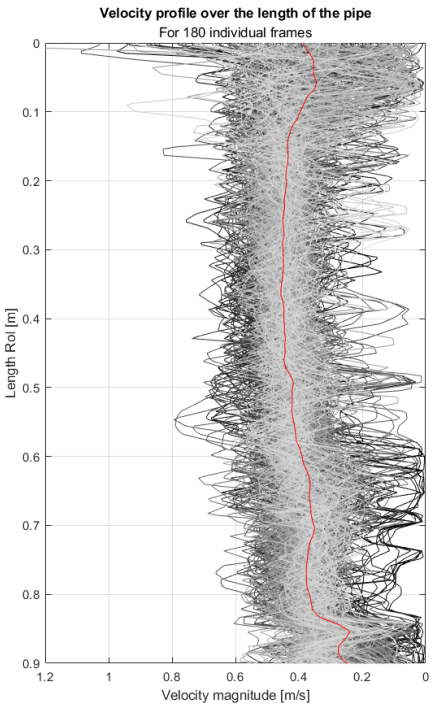

Figure C.62: Vertical velocity profiles run 62, 90°, 0.64 kg/s, 12-16 mm.

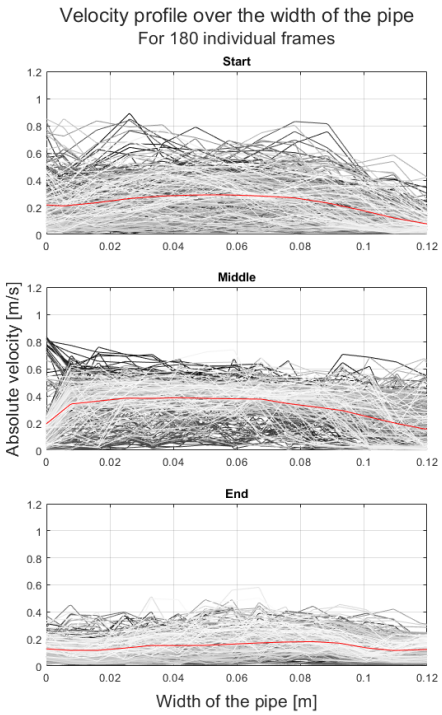

Figure C.63: Horizontal velocity profiles run 63, 90°, 0.48 kg/s, 12-16 mm.

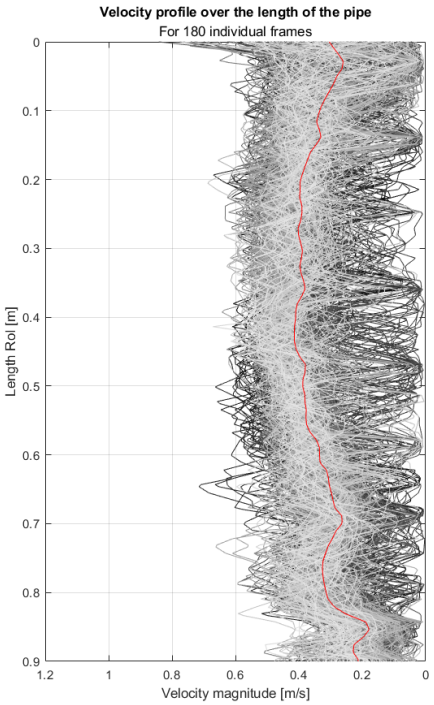

Figure C.64: Vertical velocity profiles run 63, 90°, 0.48 kg/s, 12-16 mm.

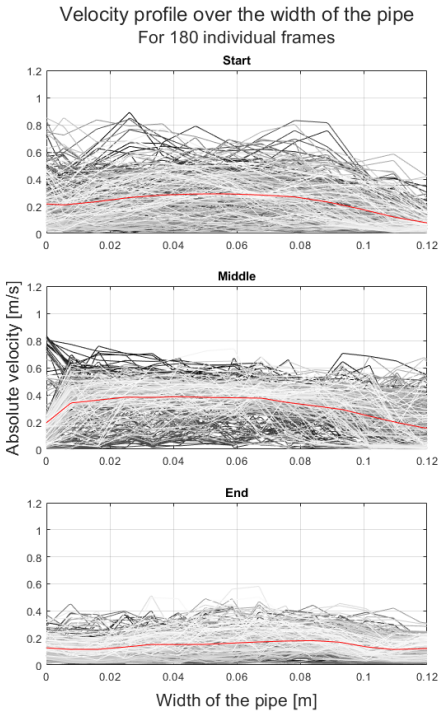

Figure C.65: Horizontal velocity profiles run 64, 90°, 0.32 kg/s, 12-16 mm.

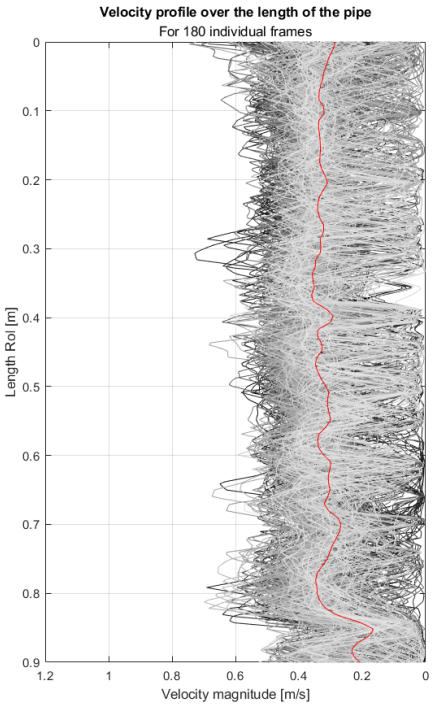

Figure C.66: Vertical velocity profiles run 64, 90°, 0.32 kg/s, 12-16 mm.

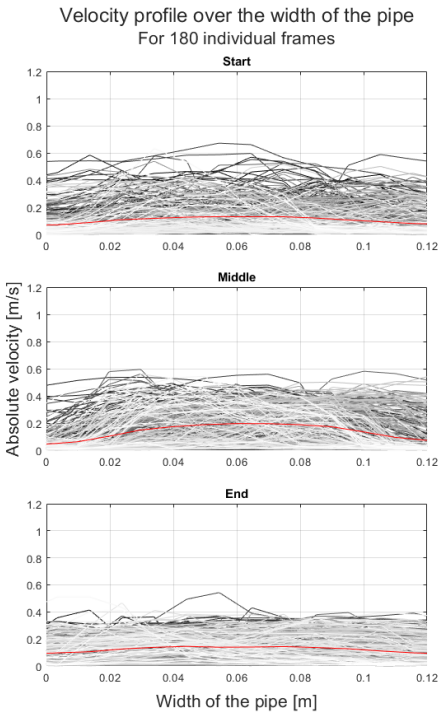

Figure C.67: Horizontal velocity profiles run 65, 90°, 0.16 kg/s, 12-16 mm.

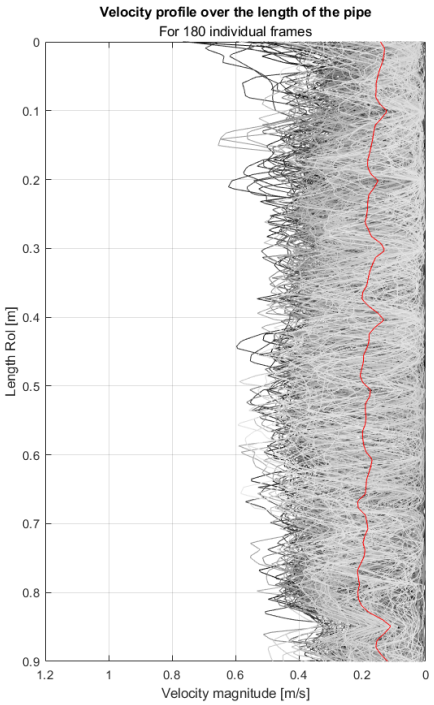

Figure C.68: Vertical velocity profiles run 65, 90°, 0.16 kg/s, 12-16 mm.

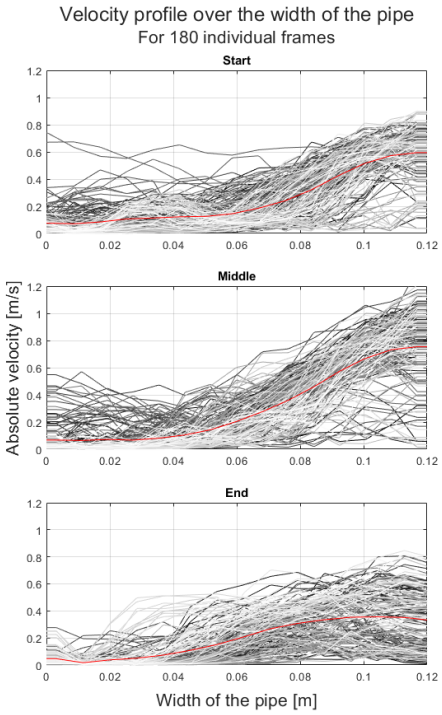

Figure C.69: Horizontal velocity profiles run 66, 75°, 0.64 kg/s, 8-12 mm.

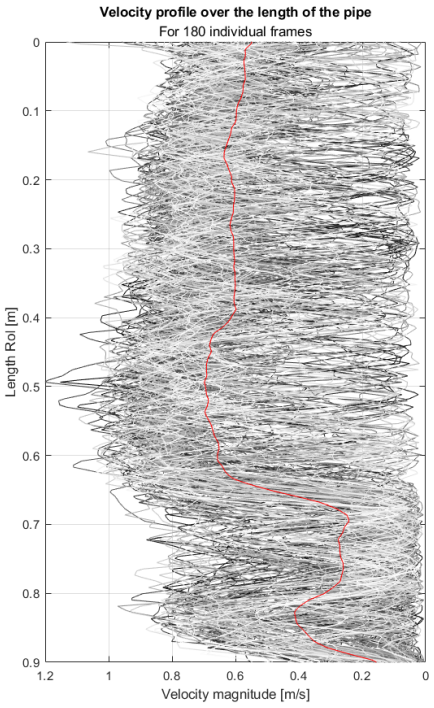

Figure C.70: Vertical velocity profiles run 66, 75°, 0.64 kg/s, 8-12 mm.

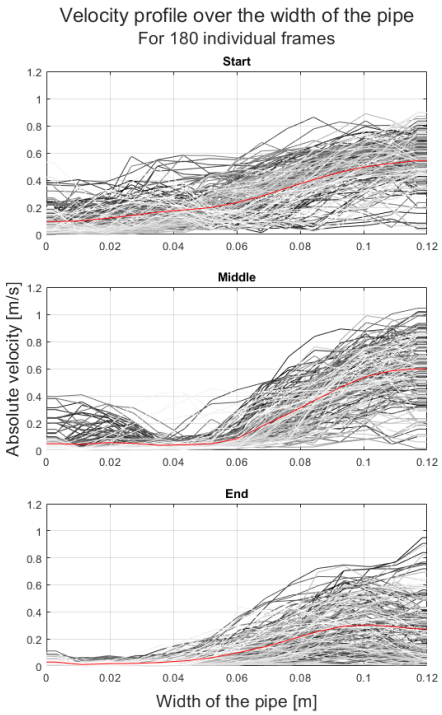

Figure C.71: Horizontal velocity profiles run 67, 75°, 0.64 kg/s, 12-16 mm.

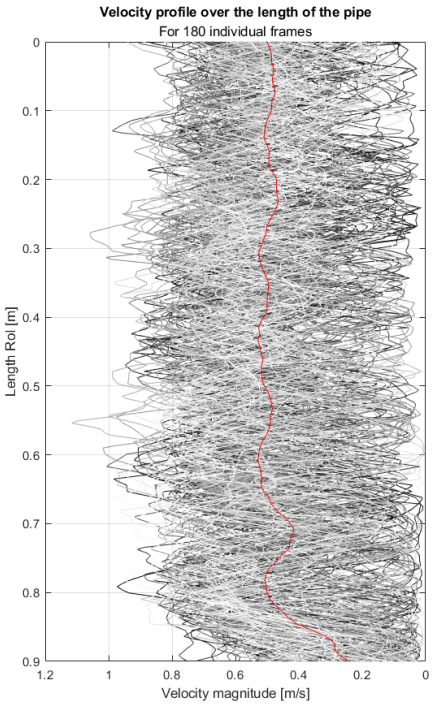

Figure C.72: Vertical velocity profiles run 67, 75°, 0.64 kg/s, 12-16 mm.

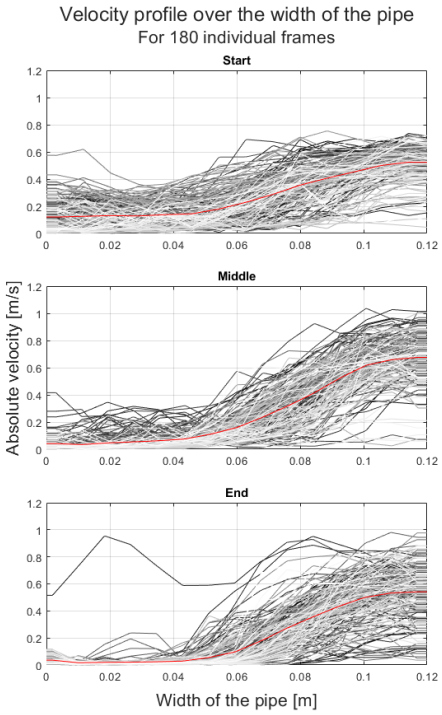

Figure C.73: Horizontal velocity profiles run 68, 75°, 0.48 kg/s, 8-16 mm.

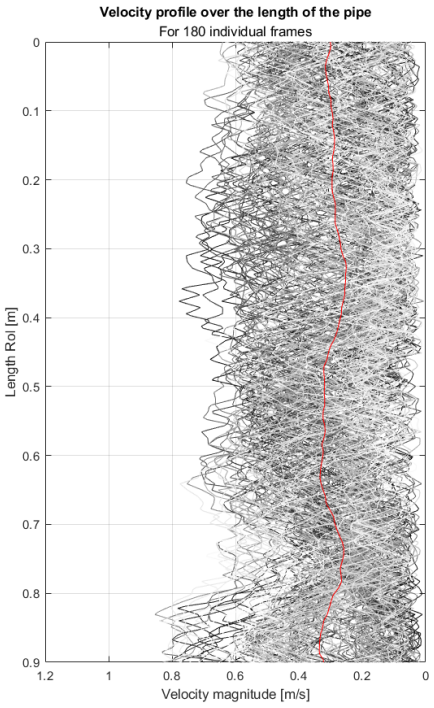

Figure C.74: Vertical velocity profiles run 68, 75°, 0.48 kg/s, 8-16 mm.

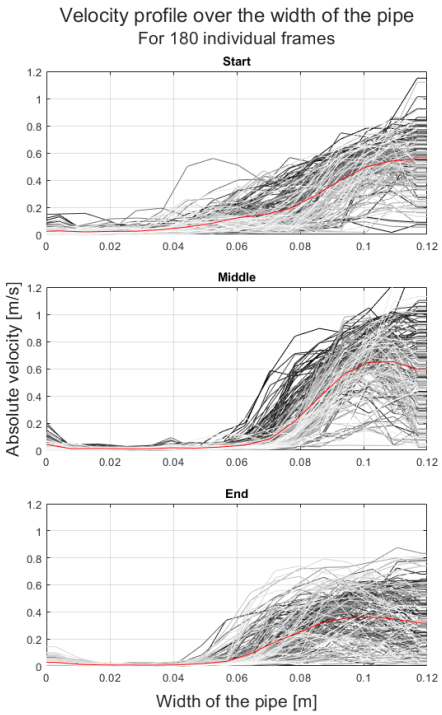

Figure C.75: Horizontal velocity profiles run 69, 60°, 0.64 kg/s, 8-12 mm.

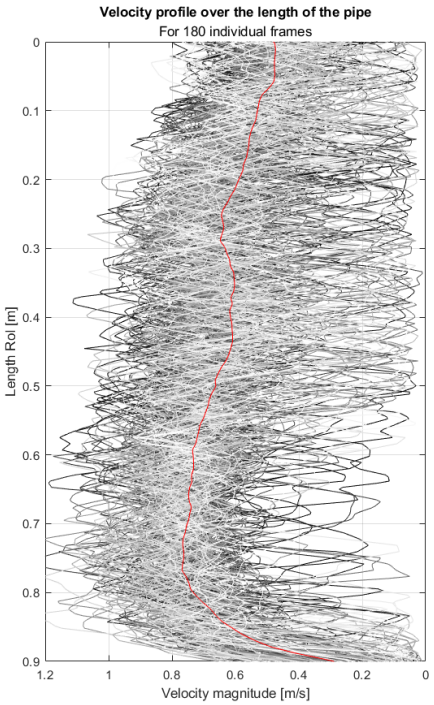

Figure C.76: Vertical velocity profiles run 69, 60°, 0.64 kg/s, 8-12 mm.

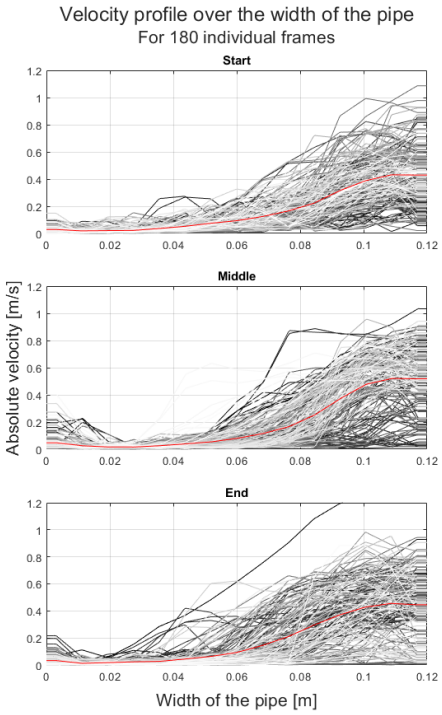

Figure C.77: Horizontal velocity profiles run 70, 60°, 0.64 kg/s, 12-16 mm.

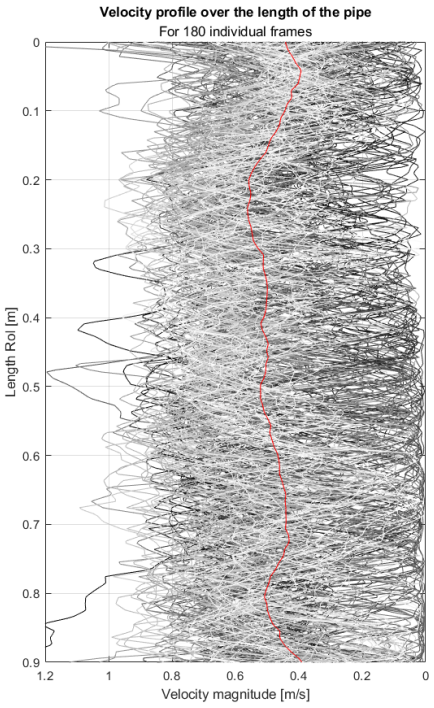

Figure C.78: Vertical velocity profiles run 70, 60°, 0.64 kg/s, 12-16 mm.

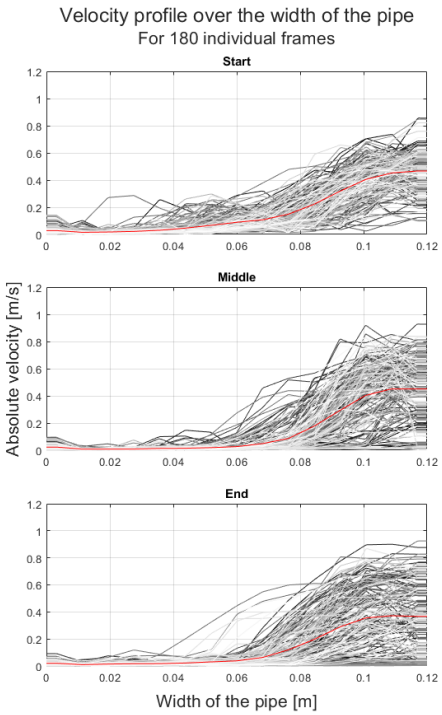

Figure C.79: Horizontal velocity profiles run 71, 60°, 0.48 kg/s, 8-16 mm.

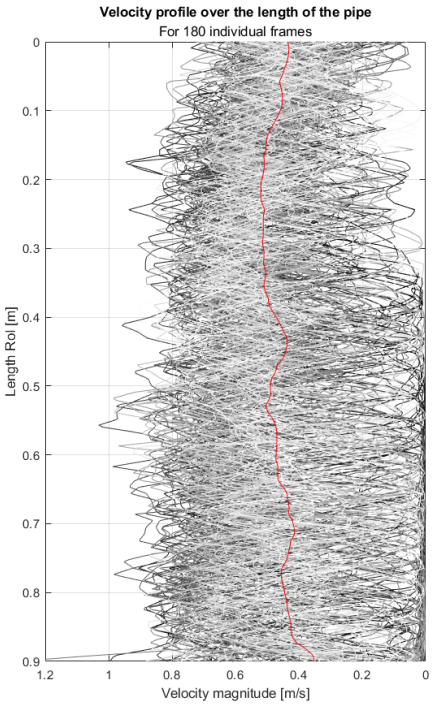

Figure C.80: Vertical velocity profiles run 71, 60°, 0.48 kg/s, 8-16 mm.

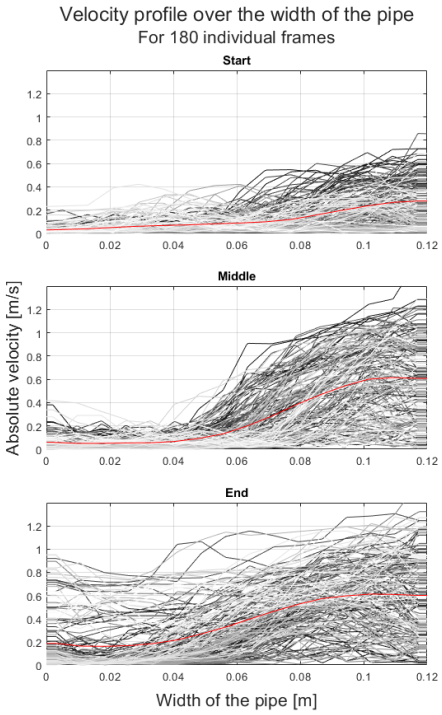

Figure C.81: Horizontal velocity profiles run 72, 60°, 0.96 kg/s, 8-12 mm.

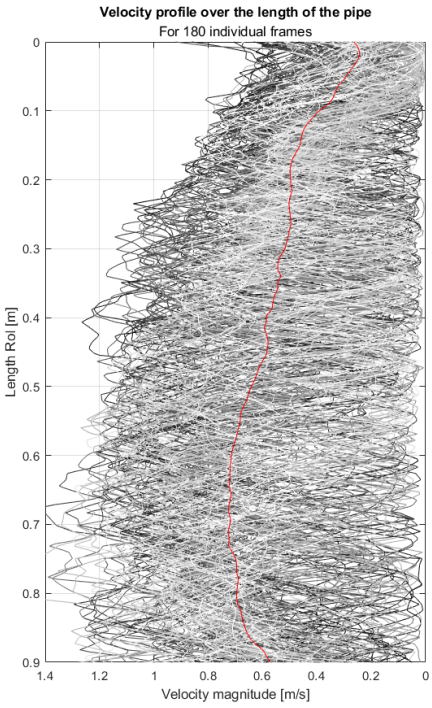

Figure C.82: Vertical velocity profiles run 72, 60°, 0.96 kg/s, 8-12 mm.

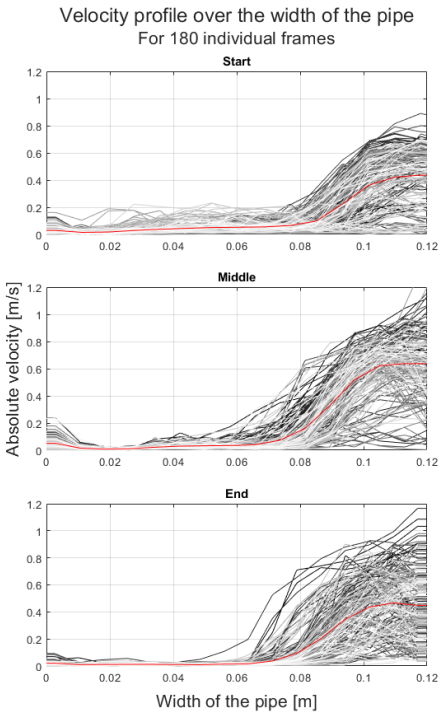

Figure C.83: Horizontal velocity profiles run 73, 45°, 0.64 kg/s, 8-12 mm.

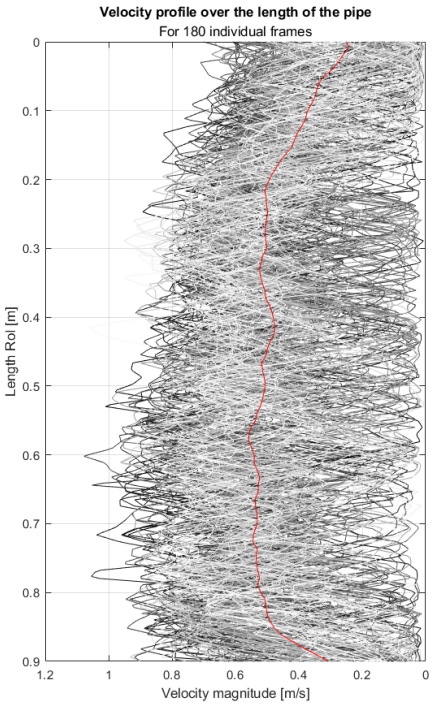

Figure C.84: Vertical velocity profiles run 73, 45°, 0.64 kg/s, 8-12 mm.

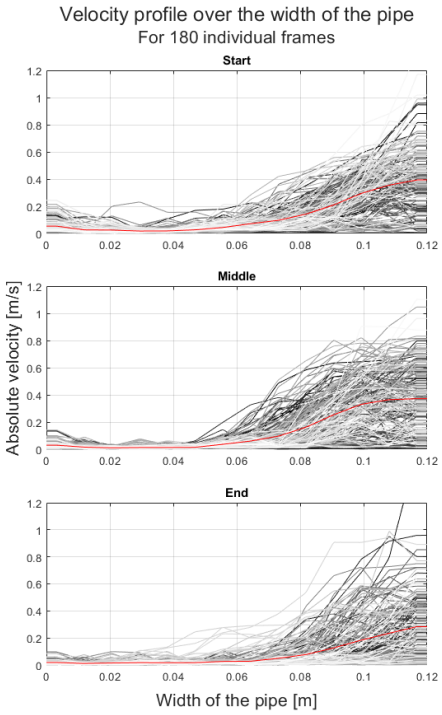

Figure C.85: Horizontal velocity profiles run 74, 45°, 0.64 kg/s, 12-16 mm.

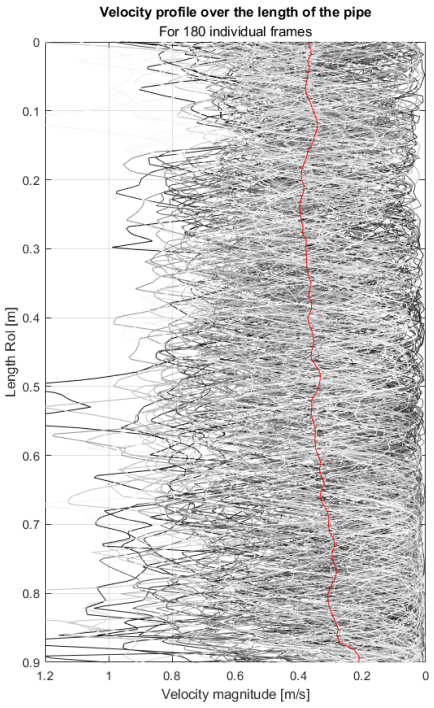

Figure C.86: Vertical velocity profiles run 74, 45°, 0.64 kg/s, 12-16 mm.

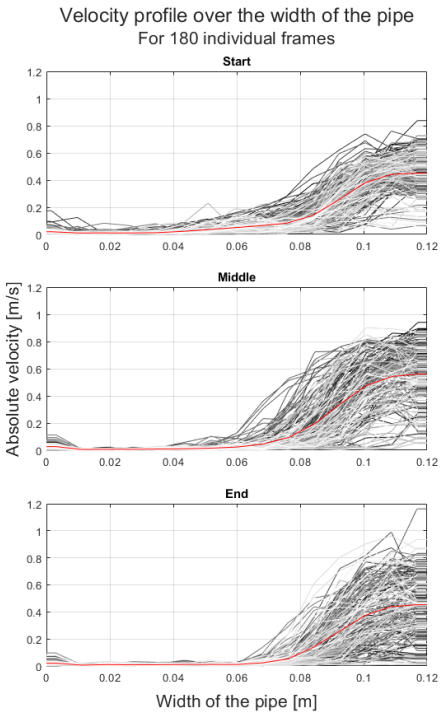

Figure C.87: Horizontal velocity profiles run 75, 45°, 0.48 kg/s, 8-16 mm.

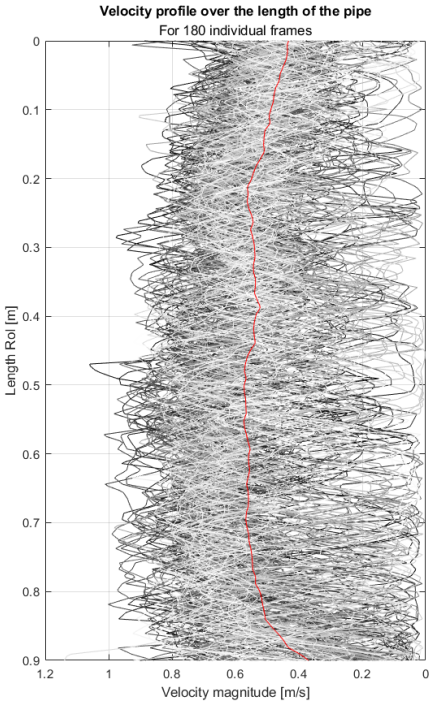

Figure C.88: Vertical velocity profiles run 75, 45°, 0.48 kg/s, 8-16 mm.